Research & Development

2022

Mechanical Engineering Letters – 2022

Technical-Scientific Journal supported by the Institute of Technology, Hungarian University of Agriculture and Life Science (MATE), Gödöllő, published by GATE Nonprofit Ltd.

HU ISSN 2060-3789

Páter K. u. 1., Gödöllő, H-2103 Hungary

Volume 23 (2022)

Contents

Impact of screw pitch length on the mixture quality of grains in a small-scale silo apparatus

Seifeddine GARNEOUI[1], István KEPPLER[1], Péter KORZENSZKY[1]
[1]Department of Mechanical Engineering, Hungarian University
of Agriculture and Life Sciences,

Abstract

Grains stocked in silos could get wet, thus the filled material might damage and causes revenue loss. For this purpose, engineers suggest blowing warm air into the silo, however this method is not efficient because that air will not reach all the parts in the silo especially in the middle where grains are dense. Stirring the material bed using a screw would be efficacious because it allows the warm air to travel through the silo and touches every particle while they are moving in the silo. As a result, the grains will keep their original characteristics and could be stored for a long duration. The better the mixture is, the better crop preservation we get. The length of the screw pitch was varied, and results showed that the best mixture is obtained when a 30mm screw pitch is used.

Keywords

mixing of grains, discrete element method, screw pitch, homogeneity

1. Introduction

Mixing is a must process in order to have an end-product of high quality in various productions, such as pharmaceutical (M. Cavinatoa, 2010), chemical (Brenda Remya, 2010) and metallurgical (Ixchel Gijón-Arreortúa, 2015). Stocking of wheat grains in silos is an ordinary task after harvesting, however the presence of moisture between grains in a silo could deteriorate the whole stock and leads to a huge loss. Typically, pumping hot air from the bottom of a silo is the used technique to remove the moisture, however when dealing with a large mass of material, moisture will slightly decrease, but an important amount remains present. For this concern, agitating the whole material with a screw would let the air to flow among the majority of particles, consequently the remained moisture will diminish. In addition, over-mixing costs money and time, therefore optimal mixing time should be pre-set to avoid these drawbacks.
Researchers studied the mixing of solid particles in various mechanisms. For example, Metcalf et al., (Metcalf, 1965) revealed using experiments that a screw feeder would be more efficient in terms of mixing quality by increasing the screw shaft diameter, increasing the screw flight diameter, decreasing the screw pitch,

and decreasing the screw rotational speed. Uchida and Okamoto (Keisuke Uchida, 2008) used the X-ray technique and they showed that a better mixture quality could be achieved by increasing the screw pitch. These contradictory results between the different experiments reveals that the appropriate selection of screw parameters depends on the particles mechanical properties. On the other hand, Peter et al., (Peter Peciar, 2018) used the Novosad theoretical mod-el to measure the resulting horizontal force acting on a blade for individual blade immersion depths during mixing, yet many terms must be calculated ahead, which make this method complicated.

With the emergence of the numerical tools based on the discrete element method, the old experimental trial and error method which is costly and time consuming is no more appropriate. Numerical simulations are conducted instead to imitate a real process and obtain many in-formation of vital importance that cannot be obtained using real experiments such as particles coordinates, particles velocities, forces acting between particles, etc. (Fenglei Qi, 2017) (Attilla Varga, 2015). Ali et al., (Ali Hassanpour, 2011) evidenced that DEM simulations showed adequate rapprochement with real experiments in a paddle mixer, which appears to be a favorable tool to forecast particles dynamics. Boon-kanokwong et al., (Veerakiet Boonkanokwong, 2016), revealed using discrete element simulations that the mixture quality is at its maximum when using two or three blades in a bladed mixer instead of one or four blades.

In our previously conducted study that used a new screw design by adding ploughs mated to the screw and evaluating the mixture uniformity using the classic index of mixing so-called Lacey index (Seifeddine Garneoui, 2020). We have seen that less volume would be available for filling grains, also changing the number of cells alters the Lacey index results. In this paper, we examined the effect of the following parameters: initial filling configuration of particles, screw rotational direction, screw pitch length, screw diameter and screw rotational speed on the mixture uniformity of wheat particles in a hopper-bottom screw mixer and examining these parameters would help to improve the mixer performance. A bi-component mixture was performed firstly using EDEM® (discrete element software), then the mixing index based on the nearest neighbor's method (W Godlieb, 2009) was employed to quantitatively evaluate the mixing rate.

2. DEM simulation

Contact model and Rayleigh time-step

The discrete element method is a powerful numerical tool that could be used to study the movement of particles during a mixing process. DEM applications could be found in various domains such as geophysics (Mathieu Renouf, 2012), masonry (Vincent Acary), blending (Meysam Alien, 2015), etc. Interactions defined between the different types of materials allows to calculate the normal and tangential forces by iteration along the process. In each iteration, several steps must be accomplished in order to move to the next iteration; it starts with the

detection of contact, then the calculation of the normal and tangential forces, respectively, which are calculated as follows:

$$F_n = \frac{4}{3}E_0\delta^{\frac{3}{2}}\sqrt{R_0} - 2\sqrt{\frac{5}{6}}\frac{ln\,C_r}{\sqrt{ln^2\,C_r+\pi^2}}\sqrt{2E_0}\sqrt[4]{R_0\delta}\sqrt{m_0}v_{nrel}, \quad (1)$$

When two particles come into contact, their equivalent Young's modulus E_0 is calculated by the subsequent formula: $1/E_0 = (1-v_1^2)/E_1 + (1-v_2^2)/E_2$. δ quantifies the overlapping between those two particles, $C_r$describes the rebounding of each particle after contact with another particle known as the coefficient of restitution (this coefficient should be defined in EDEM® pre-processor as the ratio of relative speed after collision to relative speed before collision), and v_{nrel} is the normal component of the relative velocity of particles.

$$F_t = -8G_0\sqrt{R_0\delta}\delta_t - 2\sqrt{\frac{5}{6}}\frac{ln\,C_r}{\sqrt{ln^2\,C_r+\pi^2}}\sqrt{2G_0}\sqrt[4]{R_0\delta}\sqrt{m_0}v_{trel}, \quad (2)$$

The equivalent shear modulus G_0 of two particles in contact is calculated by: $1/G_0 = (1-v_1)/G_1 + (1-v_2)/G_2$.$\delta$ and $\delta_t$describe the normal and tangential overlap between those particles, respectively, and v_{trel} is the tangential component of the relative velocity of particles. The first to last tangential contact between those particles upon slip or collision is the definition of the tangential overlap.

The dynamics of particles are computed iteratively through time to solve and update the differential equations. As it has been revealed, results would not converge without an appropriate setting of time-step, therefore it should be attentively pre-set. (Maryam Asachy, 2018). Usually, Rayleigh time is used to estimate the maximum time-step for such a DEM simulation to run stably, it is calculated as following:

$$T_{Rayleigh} = \frac{\pi R\sqrt{\frac{\rho}{G}}}{0.1631v+0.8766}, \quad (3)$$

Where;R, ρ, G and v are the average particle radius, particle density, particle shear stiffness and particle Poisson's ratio, respectively.

Based on previous conducted studies that utilized discrete element simulations, it would be better to choose a time-step below the Rayleigh time to avoid significant errors (Attilla Varga, 2015) (Z. Yan, 2015). In our simulations we fixed the time step at 40% of Rayleigh time for all the simulation scenarios.

3D model and DEM scenarios

The CAD model of the mixer showed in Figure 1 was imported into EDEM® discrete element software. The mixer has a screw positioned in the middle and was set at a 60rpm rotational speed after generating all particles under the effect of gravity in the mixer. This mixer depicts a small prototype of a silo used for storing and conserving granular materials such as wheat, cement, etc. However,

this mixing operation is a convolute task because many operational and physical factors could have an impact on the homogeneity results.

The mixer frame has the following dimensions: diameter = 100 mm, length = 250mm, and screw diameter = 10mm. While these dimensions were kept unchanged for all simulations, the screw pitch was varied (Figure 2).

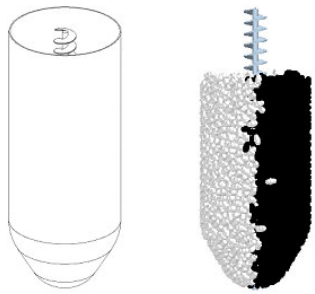

Figure 1. Mixer apparatus and initial configuration of the loaded bi-component grains

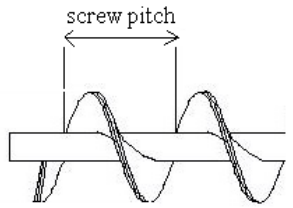

Figure 2. Screw pitch illustration

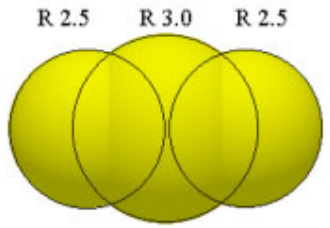

Figure 3. Shape of the grains used in DEM simulations

The shape of each particle was created as a clump of three bonded spheres to approximately mimic the real shape of a wheat grain (Figure 3), and a 70% fill fraction by volume was considered in all the numerical runs. This high filling level was intentionally identified as the flow of particles is more intense, which makes

the mixing process more challenging. The micro-mechanical properties utilized in our study were taken from the literature (Istvan Keppler, 2012).

The numerical experiments conducted are presented in the following table.

3. Results and discussion

Qualitative study

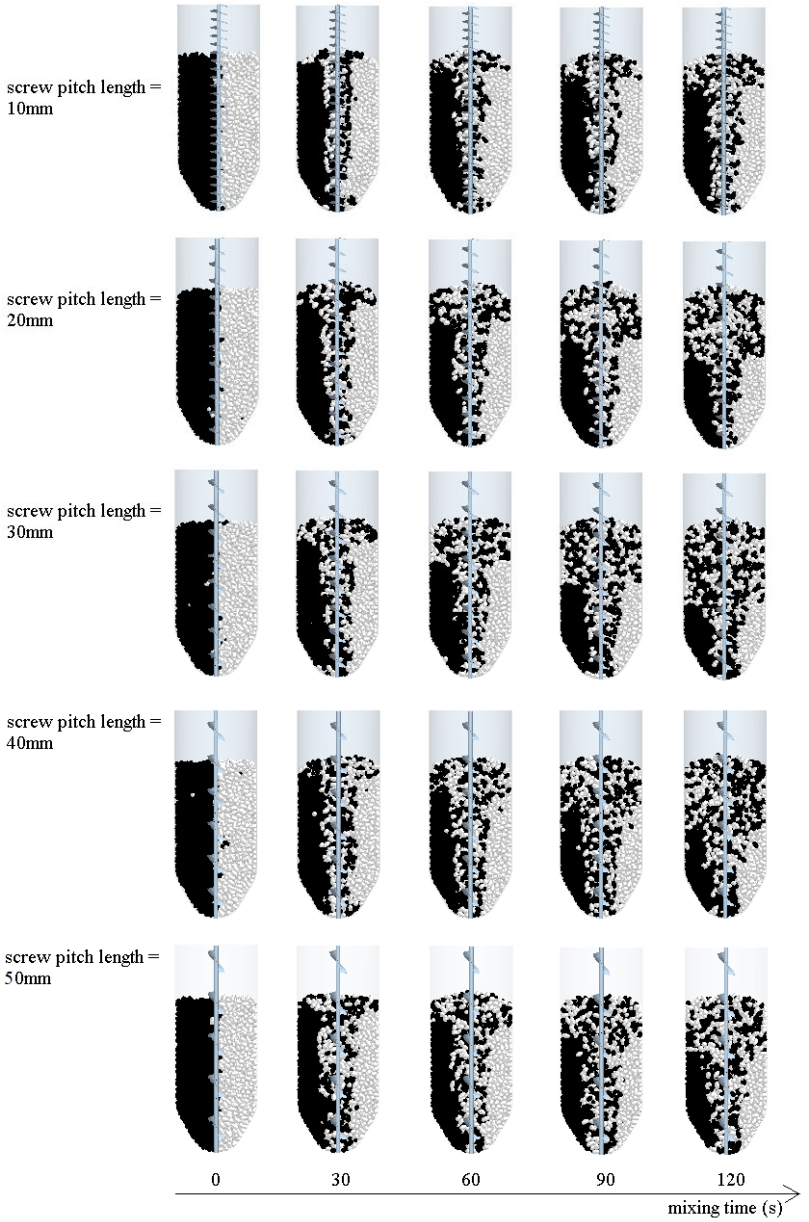

Figure 4. Mixing index based on the nearest neighbor's method

Table 1. Simulation scenarios executed

Run	Screw speed (rpm)	Screw diameter (mm)	Screw pitch (mm)
1	60	10	10
2	60	10	20
3	60	10	30
4	60	10	40
5	60	10	50

The pitch dimensions investigated are: 10mm, 20mm, 30mm, 40mm and 50mm, while the screw diameter and screw speed maintained constant. Particles state from the mixer wall doesn't give an adequate information about the mixing quality, therefore we clipped the system longitudinally along z direction to have an insight into the particles state in the middle of the mixer. Snapshots were taken each 30 seconds mixing time for all the simulations (Figure 4).

Snapshots of the internal structure of particles reveals that the homogeneity is at its maximum when using a screw pitch length of 30mm and the homogeneity is at its minimum when using a screw having a small screw pitch length. Also, increasing the length of the screw pitch above 30mm adversely impacts the mixing quality as revealed when using a 40mm and 50mm screw pitches.

Quantitative study

We have calculated the mixing indexes related to each DEM run using the nearest neighbor's method. This method is based on the position of every particle in the DEM domain. It is illustrated and described below.

Figure 5. Mixing index based on the nearest neighbor's method

Figure 5 presents a case study of the nearest neighbor's method. This method works as follows: it finds the 12 nearest particles to each particle by iteration. For instance, as shown in Figure 5, particle *i* in black has 4 white particles and 8 black particles in the vicinity, consequently the index of particle *i* is M_i= (2*4)/12 = 0.67. The mixing index of the whole material bed is the mean value of the indexes related to each particle.

Reading the graph below, it supports the qualitative examination because the best mixing rate is obtained when a screw having a 30mm pitch dimension is used.

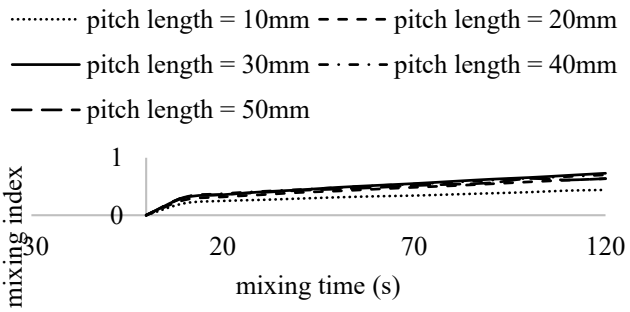

Figure 6. Evolution of the mixing rates according to the screw pitch dimensions

Conclusions

This study tackled homogeneity examination of a binary mixture of wheat particles. The loaded material was mechanically mixed in a hopper-bottom screw mixer under various dimensions of the screw pitch.

- Qualitative results clearly showed that the optimal screw pitch length is 30mm in order to get the best mixing quality of the bi-component mixture of grains.
- Calculating the mixing rate along every mixture by changing the pitch length of the screw allowed to obtain the evolution of the mixture uniformity during the process. By reading the data, we found that utilizing a screw having a 30mm pitch length improved the mixture by 58.5%, 13.9%, 1% and 6.7% compared to 10mm, 20mm, 40mm, and 50mm screw pitches, respectively.

Acknowledgements

This research was supported by the Stipendium Hungaricum Program.

References

[1] Ali Hassanpour, Hongsing Tan, Andrew Bayly, Prasad Gopalkrishnan, BoonhoNg and Mojtaba Ghadiri (2011) Analysis of particle motion in a paddle mixer using Discrete Element Method (DEM), Powder Technology, 206 (1-2), 189-194.

[2] Attilla Varga and Istvan Keppler (2015) Particle motion around open mixing screws: optimal screw angular velocity, International journal for computer aided engineering and software, 33 (3), 896-906.
[3] Brenda Remya, Thomas M.Cantya, Johannes G.Khinast and Benjamin J.Glasser (2010) Experiments and simulations of cohesionless particles with varying roughness in a bladed mixer, Chemical Engineering Science, 65 (16), 4557-4571.
[4] Fenglei Qi, Theodore J. Heindel and Mark Mba Wright (2017) Numerical study of particle mixing in a lab-scale screw mixer using the discrete element method, Powder Technology, 308, 334-345.
[5] Istvan Keppler, Laszlo Kocsis, Istvan Oldal, Istvan Farkas and Attila Csatar (2012) Grain velocity distribution in a mixed flow dryer, Advanced Powder Technology, 23 (6), 824-832.
[6] Ixchel Gijón-Arreortúa and Alberto Tecante (2015) Mixing time and power consumption during blending of cohesive food powders with a horizontal helical double-ribbon impeller, Journal of Food Engineering 109, 144-152.
[7] J. Metcalf (1965) The mechanics of the screw feeder, Proceedings of the Institution of mechanical engineers, 180 (1), 131-146.
[8] Keisuke Uchida and Koji Okamoto (2008) Measurement technique on the diffusion coefficient of powder flow in a screw feeder by X-ray visualization, Powder Technology, 187 (2), 138-145.
[9] M. Cavinatoa, M. Bresciani, M. Machin and G. Bellazzi (2010) Formulation design for optimal high-shear wet granulation using on-line torque measurements, International Journal of Pharmaceutics, 387 (1-2), 48-55.
[10] Maryam Asachy, Ehsan Nourafkan and Ali Hassanpour (2018) A review of current techniques for the evaluation of powder mixing, Advanced Powder Technology, 29, 1525-1549
[11] Mathieu Renouf, Frédéric Dubois and Pierre Alart (2012) Numerical investigations of fault propagation and forced-fold using a non smooth Discrete Element Method, European Journal of Computational Mechanics, 15 (5), 549-570, 2012.
[12] Meysam Alien, Farhad Ein-Mozaffari, Simant R.Upreti and Jiangning Wu (2015) Using discrete element method to analyse the mixing of the solid particles in a slant cone mixer, Chemical Engineering Research and Design, 93, 318-329.
[13] Peter Peciar, Olivier Macho, Roman Fekete and Marian Peciar (2018) The use of DEM simulation for confirming the process of particulate material mixing, Acta Polytechnica, 58 (6), 378-387.
[14] Seifeddine Garneoui, I. Keppler, P. Korzensky., Mixing enhancement of wheat granules in a hopper bottom screw-mixer using discrete element simulations, FME Transactions, 48 (2020) 868-873, 2020.
[15] Veerakiet Boonkanokwong, Brenda Remy, Johannes G.Khinast and Benjamin J.Glasser (2016) The effect of the number of impeller blades on granular flow in a bladed mixer, Powder Technology, 302, 333-349.

[16] Vincent Acary and Michel Jean (2000) Numerical modelling of three dimensional divided structures by the non Smooth Contact dynamics method: Application to masonry, The fifth international conference on computational structures tribology, Leuven, Belgium.
[17] W Godlieb, SA Gorter, Niels G Deen and Hans A. M. Kuipers (2009) DEM and TFM simulations of solids mixing in a gas-solid fluidized bed, Seventh International Conference on CFD in the Minerals and Process Industries, Melbourne, Australia, pp. 9-11.
[18] Z. Yan, S. K. Wilkinson, E. H. Stitt and M. Marigo (2015) Discrete element modelling (DEM) input parameters: understanding their impact on model predictions using statistical analysis, Computational Particle Mechanics, 2 (3), 283-299.

Design of a robot vacuum cleaner

Benjámin FARKAS[1], Viktor ERDÉLYI[2]
[1,2]Department of Mechatronics, Institute of Technology, MATE, Gödöllő

Abstract

This paper presents the creation of an industrial robot vacuum cleaner that was specially designed for cleaning large areas. To achieve the goal, modern, up-to-date technologies were used. The paper discusses the design, production, and programming of the robot vacuum cleaner. The robot chassis was designed using Solid Edge and manufactured using 3D printing technology. The results show that the robot vacuum cleaner successfully fulfills its intended purpose, and its operation proved to be problem-free. In the future, the technologies and tools used will allow for the further development of the robot, which will reveal alternatives for the robot vacuum cleaner that make the operation of the construction stable and more accurate.

Keywords

3D printing, Embedded systems, Autonomous, Python, Ultrasonic sensor

1. Introduction

An autonomous robotic vacuum cleaner, sometimes known as a robovac or roomba as a generic trademark, features a restricted vacuum floor cleaning system coupled with sensors, robotic drives, programmable controllers, and cleaning routines. Early models had remote-control manual operation and an autonomous cleaning mode called "self-drive." Some designs combine a number of cleaning elements with the vacuuming feature, while others employ spinning brushes to reach confined spaces. For improved mapping, object recognition, and event-based cleaning, more modern models incorporate artificial intelligence and deep learning. At an American National Exhibition held in the Soviet Union in 1959, the first concept for a robotic vacuum cleaner was conceived. Although the concept was carried out, just a prototype was made, and not much is known about it. The British business company Dyson developed the DC06 robot vacuum cleaner in 2001; however, this particular model was never made public. Furthermore, the first Roomba, which was introduced in 2002 by American startup iRobot, marked a significant advancement. They were able to sell about 50,000 units during the first year following the product's introduction. And this number is only rising as a result of new models and advancements. (Fahimi, 2009)

In order to clean regions that a regular household robot vacuum cleaner cannot,

the aim of this paper is to develop a robotic vacuum cleaner utilizing 3D printing technology and embedded systems.

2. Materials and methods

The production of the mechanical structure of the robotic vacuum cleaner
Before starting construction on the robot vacuum cleaner, existing robot vacuum cleaners were looked up on the market, both in terms of their size and technological specifications. The parts that were going to be used for constructing the robot were gathered as a first step in the design phase. Technologies that might be utilized to create the robot's structure were looked up once the necessary components had been acquired. 3D printing was the most optional method for its realization, as the writer acquired the knowledge at university that allowed him to use CAD (Computer Aided Design) programs, so he was able to design the robot vacuum cleaner and manufacture it. The robot's 3D parts were created using the Solid Edge software.

In order to work properly and fit inside the robot vacuum cleaner, housings and holders were created for the many different electrical components. First, the robotic vacuum's frame was created, which serves as both the vacuum's basic structure and the place where all of its electronic parts are housed.

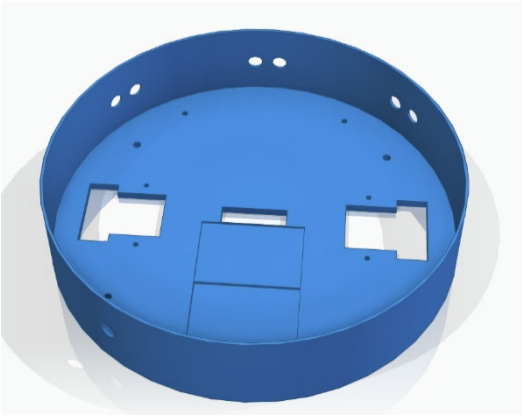

Figure 1. The frame of the robotic vacuum with the necessary cut-outs.

An application called Cura was used after setting up the printer. Cura is an easy-to-use tool that enables you to change a variety of printer parameters, like how quickly the printer prints, how hot the printing plate and nozzle temperatures should be, etc. Solid Edge files should be saved in the "OBJ" format so that Cura can accurately convert 3-dimensional solids to wireframe. Cura will produce the G-code when the file has been loaded and the appropriate adjustments have been made, which the printer may then use. We can see several kinds of 3D-printed

parts both within and outside the frame. Stepper motor holders, battery housing, a dust collection tank, and a suction motor housing are a few examples.

Due to the limitations of my printer's plate (220x220x250 mm), the larger parts had to be cut into smaller pieces. Three-dimensional bodies can be cut along the X, Y, and Z axes using a program called Netfabb, which was the used method to solve this problem. Following that, these components were either bolted or glued together. (Shahrubudin, 2019)

The parts are made from PLA, a thermoplastic polyester, usually made from sugar cane or corn starch. This material was chosen because it is relatively hard to break in the solid state, it can be printed quickly (printing speed depends on the material) and has a fairly long degradation time (about 80 years), with the only major drawback being its low thermal resistance. Printing settings are largely the same for all parts. Nozzle temperature 215 °C, plate temperature 60 °C. Filling was 20% gyroid, and the wall thickness of the parts was generally four strands. A 0.8mm nozzle was used to produce the larger parts, and a 0.4mm nozzle was used for the smaller parts requiring more precision.

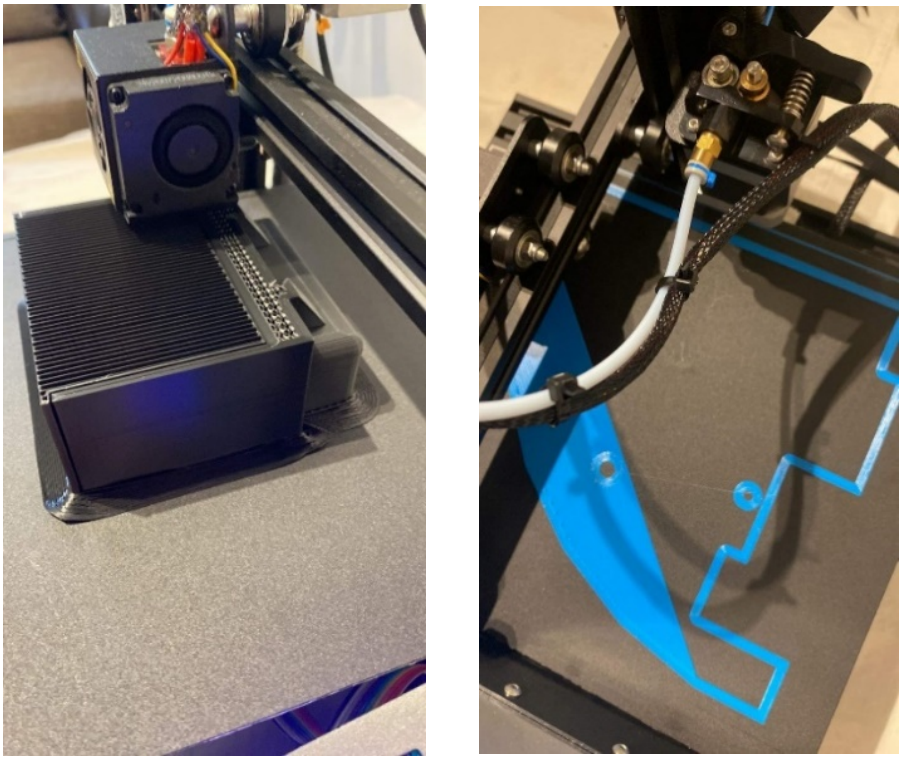

Figure 2. Parts during printing.

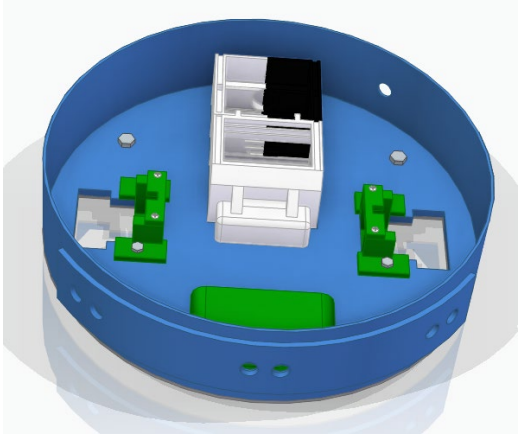

Figure 3. The 3D printed components assembled together.

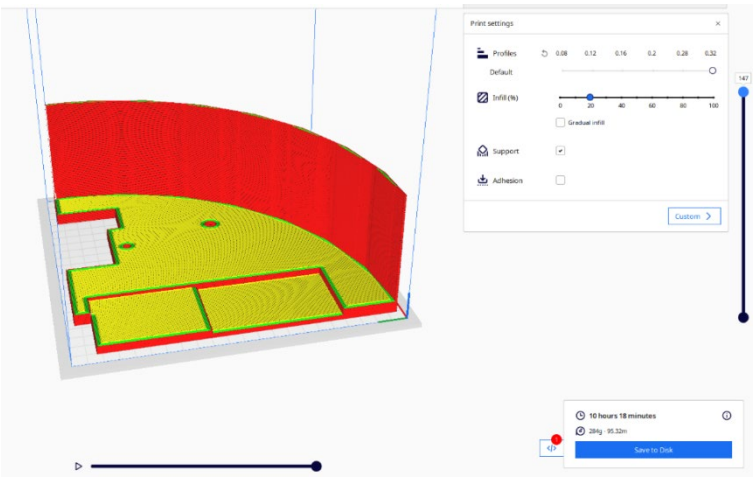

Figure 4. Part of the robot frame, imported into the Cura program.

The electrical circuit was planned after all of the components were produced and assembled.

Design and implementation of the electrical circuit

To create the electronic circuit diagram, a website called *Gliffy* was used, which allows a simple block diagram representation of the electrical circuit. The diagram is shown below.

The battery pack, which comprises of six 18650 Li-ion batteries and a 6S BMS to manage their charging, was first assembled. The batteries were connected to the charge control device by soldering wires to the battery outputs on the battery housings. The nominal maximum voltage of the battery pack is 23.7 V. Of course, there are components in the robot do not require such high voltage and most likely

would suffer harm from it. Buck converters were therefore used to lower operating voltages to suitable level. A buck converter is a device that uses the power of direct current (DC) to decrease higher voltages to lower ones and uses closed loop control to ensure precise output voltage. (Gabbar, 2021)

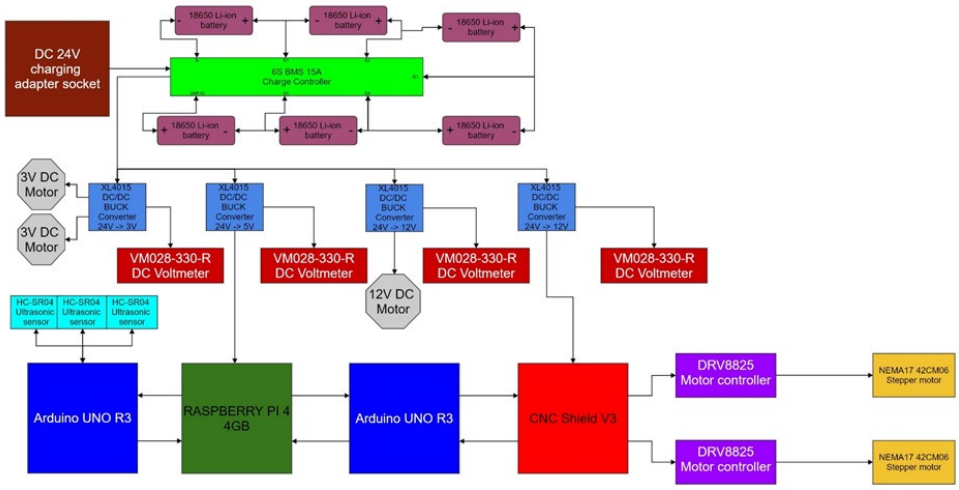

Figure 5. The circuit schematic in block diagram representation.

The robot has four such converters, to which cables were soldered. They are fed through these wires from the battery pack. Two of the converters produce 12V; to power the vacuum motor, the stepper motors, and the fans used to achieve the active cooling. The third converter generates 5V, which powers the robot's "brain," the Raspberry Pi, and the Raspberry Pi itself also powers two other important devices, the two Arduino Uno R3 development boards. The final voltage converter generates 3V, which is used by the DC motors driving the two brushes. To distribute the voltage, paralleling devices (WAGO) were used. Each converter branch has at least two of these components. (Matt Richardson, 2013)

The drive's implementation came next. In the robot vacuum's early phase, two 0.4 Nm bipolar NEMA17 stepper motors were used. These motors were selected because they are easy to regulate, extremely accurate, and capable of applying strong forces—a factor that was crucial for me because the robot weighs 6 kg. Unfortunately, the motors failed to move the robot during testing because they were underpowered. More powerful motors were purchased to address this issue. These motors were capable of producing 0.6 Nm of torque. After a few tests, it was confirmed that these motors would be able to move the robot. The motors are controlled by an Arduino Uno R3 development board, to which a CNC Shield V3 is connected. DRV8825 motor controllers were installed on the CNC Shield, which can operate from 8.2V to 45V, with a maximum current draw of 2.5A.

During the assembly, larger heat sinks were installed on the two motor controllers because the factory heat sinks weren't sufficient to dissipate thermal energy, which caused problems such as the melting of the cables connected to the motor controllers. (Crowder, 2019) (Morega, 2017)

The motor controllers can be used to adjust the current strength, which also affects the force applied to the stepper motors. For the DRV8825 motor controllers, the following formula must be used to obtain the correct current:

$$V_{REF} = \frac{I_{max}}{2}$$

Based on the formula, the motor controllers pass 2 amps of current to the motors individually, resulting in stable robot motion.

After assembling the drive, the wiring of the DC motor, which acts as the suction motor was redesigned, as it originally had a cigarette lighter charger design. The cigarette lighter cable end was cut, the end of the wires were stripped and then were coated with tin, and then the tin-coated cables were inserted into one of the paralleling connectors.

Next, the power supply of the Raspberry Pi was sorted. The voltage is taken from the Buck converter branch that supplies 5V, with a USB Type-C cable inside to supply power to the Raspberry. The plastic coating from the USB cable was removed, and then the ends of the wires were coated with tin and placed into a paralleling unit.

The next problem was how to power the two Arduino Uno development boards. Then it was discovered that the USB Type B ports on the Raspberry Pi are suitable for this purpose, as they can supply 5V, which meets the power supply criteria for the two Arduino.

Since power was provided to the Arduino boards, they were also able to supply power. This power source is used by the ultrasonic distance-sensing sensors. The distance sensors require a voltage of 5 volts, which they receive via ribbon cables, also known as jumper cables, and communication with the Arduino is also done via such cables.

Moving on, the problem of powering the 3V DC motors that drive the brooms was solved. Their voltage source is provided by a buck converter, which generates 3 V on its output branch. The cables were to the outputs of the DC motors, which are connected to a parallel connector. To ensure that the robot vacuum cleaner is actually able to perform the sweeping operation, cables were soldered with reversed polarity to one of the DC motors. To simplify, the positive and negative sides were reversed so that one of the motors rotates counter-clockwise, causing the sweepers to sweep dirt in the direction of the suction port.

The last step was to power the CNC Shield. The CNC Shield requires a voltage of 12 volts, which was provided by one of the voltage converters described above. For the CNC Shield, only two single cables were needed. One end of the cable connects to the CNC shield's solderable socket, while the other ends in a parallel connector. (Taufer, 2018)

The designed and electronic components were then placed in their designated positions in the robot frame in a 3D environment and on the robot frame within an assembly file. The final result is illustrated in the figure below:

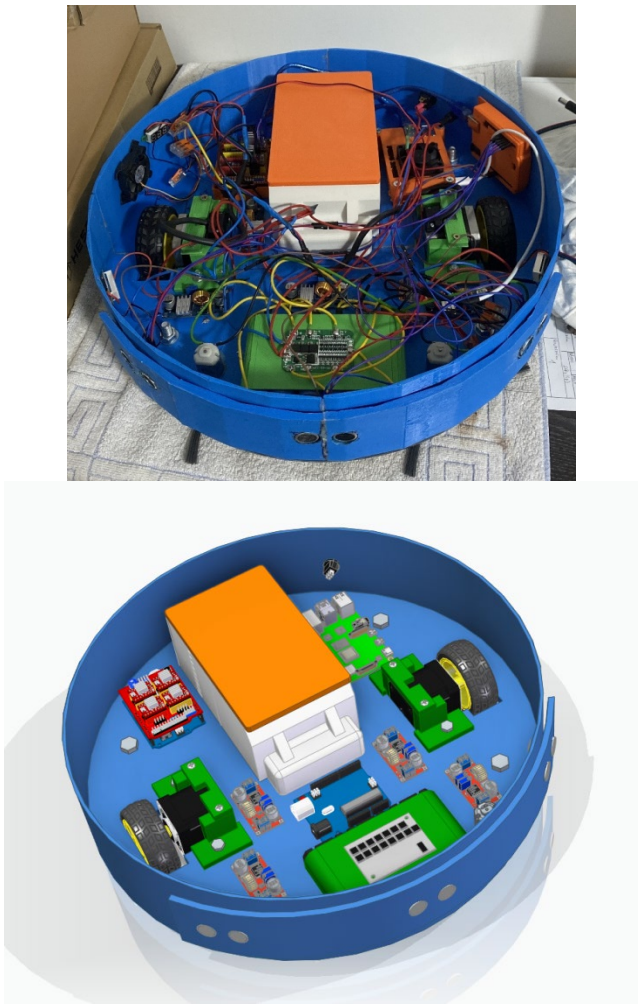

Figure 6. Assembled representation of the robot vacuum cleaner (without top element).

2.3. Software development of the robot

The development of the operating software began by implementing the Arduino program, which controls how the motors move. First, libraries were looked up that were required to program the Arduino development board. These libraries are made up of many files that give the software more functionality. During this search, a library was found that aids the effort to control the motors. The name of this library is "AccelStepper." (Kuldeep Singh Kaswan, 2020)

To aid in determining the precise speed of the motors, a number of variables have been added at the beginning of the code. The so-called "setup" function, which is only executed once at program start, is then entered by the code. In this part, the serial port is opened for communication between the Arduino and the Raspberry Pi via a type AB USB cable connection. The code then resets the motors by sending a value of 0 to the motors' speed variable. The program then enters the "loop" function, which operates repeatedly while the program is running, as suggested by its name. The "szamolas" function, which will be described in the next paragraph, is the first thing that the loop section calls.

If the serial port is accessible, the "szamolas" function receives the message received during communication and saves it in a variable. After that, the saved message is put through a number of tests, for which "if" branches have been utilized. These ask about the message's character count and if it contains a negative sign (the latter is only asked in one case). The function examines the message, stores it in two variables, and then converts it to an integer using my conversion function. This is so that the stepper motor's control package, which only supports integer variables as speed values, may be utilized. Because the converted values lose their decimal separators during the conversion, which is what allows the data to be successfully sent in the Python code, the existing integer variables are divided by 100 as a last step.

Next, an Arduino program was created to read and send the distances measured by the ultrasonic sensors. The first command lines of the program define the communication connections of the ultrasonic sensors, and then several variables are created to store and transmit the data measured by the ultrasonic sensors. In the setup function, the serial port communication with the Raspberry Pi is opened, and then the sensor connectors are set: the "Trig" pins are set as output, the "Echo" pins as input. The program then enters the loop function, which reads out the values of the distances received in the "SonarSensor" function and passes them to the Raspberry Pi, separated by dashes per sensor. The SonarSensor function sends out a pulse, then waits for the signal to return, measuring the time between the pulse being sent and returning. During this time, the signal has travelled to the obstacle and then from the obstacle back to the sensor. Since the signal travelled twice the distance between the obstacle and the sensor, the value of the received signal is divided by two, and the resulting unit of time in milliseconds is divided by 29.1 milliseconds, which is the time it takes for the sound to travel 1 centimetre. Thus, the calculated value is the distance of the obstacle from the sensor in centimetres.

After making the Arduino codes, the Python programming language codes were made, which are running on the Raspberry Pi. First, a program that calculates two given values was created. The two calculated values are first stored as a fractional number, which is then converted by the program to a rounded value, i.e., an integer, and finally converted to a variable of type "String." The Raspberry Pi then sends the values to the Arduino controller card, which sets these values as the speed of the motors. The code also includes a function called "TankMode," which is called when the ultrasonic sensors detect an obstacle ahead. Within the function, there are two branches that check whether the sensors detect an obstacle to the left

or to the right and then use the information to decide which direction to rotate the robot to avoid the obstacle. Performing this operation is very simple; the code simply prepends a minus sign to either the left or right motor speed value, depending on which side the sensors detected an obstacle, so the robot can rotate in place.

The second Python-based code handles ultrasonic sensor readings from the Arduino. To simplify this, four functions were created. Three of the four functions are responsible for coordinating the robot's movements. These are called based on the signals from the sensors; for example, if the sensors detect an obstacle on the left, a function called "wall_hit_Left" is activated, which then imports the data needed to avoid the obstacle into the aforementioned TankMode function. Otherwise, if the obstacle is detected on the right, the function "wall_hit_Right" is activated, and if there is no obstacle in front of the robot, the method "clear_way" is activated. (Snape, 2010)

Results and conclusion

This paper's aim was to develop a robotic vacuum cleaner that could effectively clean big areas. In order to develop the robot, vacuum cleaner scholarly articles, scientific studies, and instructional videos were looked up. In order to understand what parts are employed within these cleaner robots, a market research on comparable robot vacuums was also conducted.

Before beginning the robot's design, the required electronic parts were gathered. The robot’s movement were done by stepper motors. The sensing and coordination of the surrounding environment are carried out by three ultrasonic distance sensors. To control all of these gadgets, two Arduino Uno development boards and a Raspberry Pi 4 Single-Board Computer were utilized.

Then, using the Solid Edge software, the robot vacuum cleaner's 3-dimensional blueprints were created. When designing each component, the proportions of the electronic components were taken into account. The robot vacuum cleaner's frame and other smaller elements may therefore be produced more easily thanks to the use of 3D printing technology.

After finishing the robot's chassis and its smaller components, the 3D-printed components of the robot vacuum cleaner were joined by screwing and gluing them together.

After the assembly, the electronic parts were placed and wired together. The robot has four circuits that were built with buck converters. After assembling the hardware, the operating software needed to run the robot vacuum's operation was created. The programs are made up of three Python programs and two "C" program codes. Based on the goals, the robot vacuum cleaner effectively completes its duty. Additionally, there are other development choices accessible. The ROS system would be the best option if it was required that the robot vacuum cleaner move and perceive its surroundings more precisely. This allowed for the creation of the mapping function and other precision-assistance features, both of

which are currently present in the majority of robot vacuum cleaners on the market.

References

[1] Crowder, R. (2019). In *Electric Drives and Electromechanical Systems* (old.: 209-226). Elsevier Ltd.
[2] Fahimi, F. (2009). *Autonomous Robots.* New York, NY: Springer New York, NY.
[3] Gabbar, H. A. (2021). *Review of Battery Management Systems (BMS) Development.* Oshawa, Canada: University of Ontario.
[4] Galadima, A. A. (2014). *Arduino as a learning tool.* Abuja, Nigéria: Institute of Electrical and Electronics Engineers.
[5] Kuldeep Singh Kaswan, S. P. (2020). Role Of Arduino In Real World Applications. *International Journal of Scientific & Technology Research*, 1-2.
[6] Matt Richardson, S. W. (2013). *Getting Started with Raspberry Pi.* Sebastopol, CA: Maker Media Inc.
[7] Morega, A. (2017). Design and modeling of a hybrid stepper motor. *Institute of Electrical and Electronics Engineers.* Bukarest.
[8] Shahrubudin, N. (2019). An Overview on 3D Printing Technology: Technological, Materials, and Applications. *Procedia Manufacturing*, 1286-1296.
[9] Snape, J. (2010). *Smooth and Collision-Free Navigation for Multiple Robots Under Differential-Drive Constraints.* Taipei, Taiwan: Institute of Electrical and Electronics Engineers.
[10] Taufer, M. (2018). Commodity single board computer clusters and their applications. *Future Generation Computer Systems*, 201-212.

Modelling of tractor driving force during machine run-up at plowing

Jozef RÉDL[1], Juraj MAGA[2], Jozef BANGO[1], Gábor KALÁCSKA[3],
[1]Institute of Design and Engineering Technologies,
Faculty of Engineering,
Slovak University of Agriculture in Nitra
[2]Institute of Agricultural Engineering, Transport and Bioenergetics, Faculty of Engineering,
Slovak University of Agriculture in Nitra
[3]Institute for Mechanical Engineering Technology,
Faculty of Mechanical Engineering,
Szent István University, Gödöllő, Hungary

Abstract

Reducing the carbon footprint is nowadays a very popular agenda of companies that produce classic machines and vehicles including agricultural tractors. The tractor run-up process is a crucial moment when establishing the relationship between the ground and tire for transmission of the engine power for machine mass movement. If a tractor is paired with an agro-technical tool, the traction force is raised to overcome soil resistance and other driving resistive forces. The main goal of this article is to design a methodology for modeling the approximated tractive force with the utilization of spline approximation. The results of the designed model is the tractive force and driving force of the tractor with full mounted plow. The base dataset of components of tractive force on three-point hitch was taken from another research. The used plow was a product of Kverneland RS 100 for medium-deep plowing. For all mathematical procedures, we used the software Mathcad Prime 5.0. For modeled dataset, we applied the descriptive statistic functions for the determination of the standard deviation of populations or samples, Pearson's correlation coefficient for the standard error of the regression. For analyzing the time series function we used the Mathcad built-in autocorrelation function. The achieved results are compared with similar scientific results.

Keywords

plowing, modeling, spline approximation, numerical integration, tractor run-up

1. Introduction

Investigation of the driving a tractive forces of agricultural machines is mainly focused on optimalisation of the fuel consumption efficiency and the motive power effective utilization during an agro-technical operation. Measurement of

the tractive forces on three-point hitch is still attractive among the scientists. Methodology of determination of resultant tractive forces via experimental way are investigated by Bandy.et.al (1988). They research was focused on the developing an easily implemented method of accurately measuring three-point hitch (TPH) forces that did not alter the original TPH geometry. A second objective was to document the Dynamic Weight Transfer Coefficient (DWC) for several mounted implements and categorize the DWC according to the type of mounted implemented and the method used to control implement depth. Battiato et.al (2017) developed model simulates drawbar pull, traction coefficient, traction efficiency, and motion resistance as a function of slip, wheel load, tyre size and pressure. Several traction tests were performed on four Swiss agricultural soils of different type (clay, clay loam, silty loam, and loamy sand) in order to validate the model experimentally.

Experimental validation of tractive force of tractor were performed by Porteš et.al (2013). They are determined the tractor wheel load during tillage. Forces acting between tractor and implement significantly change the load of driving wheels. Mathematical description of simple model fails due to impossibility of determination these forces between the tractor and implement. The article describes the multi-body model used for calculation of resultant force and torque acting from the implement on a tractor as well as the forces acting between the wheels and the soil. Cerović et.al.(2020) developed the simulation algorithm for calculation of draft forces by two methods (followingASAE D497.4 standard and Goryachkin approach), depending on the three point linkage geometry and mouldboard technical characteristics, and calculation of forces acting on lower and upper links of three-point hitch mechanism. Calculated forces values, based on ASAE draft, exposes smaller differences compared to experimental values, while for the Goryachkin method improvement is possible by entering experimental values for soil resistance coefficient k and coefficient of dynamic resistance ε.

2. Materials and methods

Experimental dataset and model initial conditions

In this paper we are presenting the simplified 2D model to determine the traction force of tractor from the approximated draft force. The experimental dataset was taken from Slimařík (2015). the dataset was obtained from real experimental measurement. The tractor was Zetor P041 16240 with Kverneland RS 100 plow implement. The parameters of experimental ground and model objects were similar like at experiments provided by Rédl. et.al (2021). The initial conditions for the mathematical model:

- developing 2D model,
- accepting the force components only in x-axis (direction of movement),
- vertical forces at drawbar are neglected,

- three-point hitch geometry was transformed to 2D geometry,
- the real part of modelling started after the mouldboard reach the 1/3 plowing depth.

Three-point hitch model

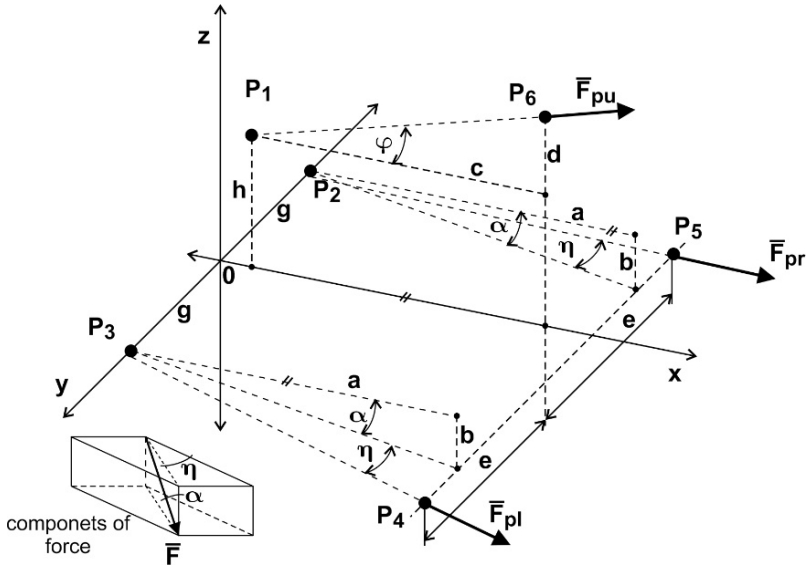

Figure 1. Three-point hitch model

The dimension of three-point hitch was taken from work of Slimařík (2015) and the model is depicted in the figure 1. The values of parameters are in the table 1. The x components of draft forces are solved for the $\overline{F}_{pu}$-upper drawbar pull , $\overline{F}_{pl}$-left drawbar pull, $\overline{F}_{pr}$ - right drawbar pull. The angles α, φ, η are solved as follows:

$$\alpha = \text{a tan}\left(\frac{b}{a}\right), \tag{1}$$

$$\varphi = \text{a tan}\left(\frac{d}{c}\right), \tag{2}$$

$$\varphi = \text{a tan}\left(\frac{e-g}{\sqrt{a^2+b^2}}\right). \tag{3}$$

For our purpose we have to find the x, and y components of drawbar pull on left and right sides of three-point hitch. The parameters of table 1 and table 2 was taken from work of Slimařík (2015).

Table 1. Parameters of three-point hitch

Parameter	Value	Unit
a	886	mm
b	74	mm
c	597	mm
d	361	mm
e	445	mm
g	255	mm
h	370	mm

Table 2. Drawbar pull

N.o.	F_{pu}, kN	F_{pr}, kN	F_{pl}, kN
1	20,61	3,63	2,66
2	22,29	5,05	4,27
3	22,05	5,04	4,35
4	23,04	5,02	4,66
5	22,53	6,14	5,92
6	24,10	5,69	5,03
F	22,436	5,095	4,482

From equations (1), (2), (3) we solved angles $\alpha = 4,7\,\text{deg}$, $\varphi = 31\,\text{deg}$ $\eta = 12,10\,\text{deg}$. The resultant tractive force was solved as follows:

$$F_{tx} = F_{pu} \cdot \cos(\varphi) + (F_{pl} + F_{pr}) \cdot \cos(\alpha) \cdot \cos(\eta) \,, \tag{4}$$

for each N.o. The time step was chosen $\Delta t = 1,0667 s$ for period $t = 6.7 s$. The resultant force is depicted in figure 2. For our model we consider, that the evaluation time not lay to the start of the tractor motion. As we mentioned in the initial condition, but we set the evaluation time approximately for the moment when the mouldboard reach the ground and penetrates the soil and breaks it open. It happens when the tractor has initial nonzero velocity on run-up.

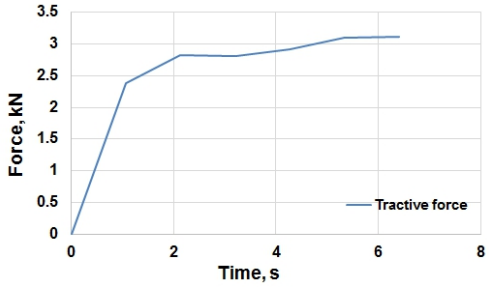

Figure 2. Resultant tractive force

Approximation and data processing

For approximation of resultant tractive force, we use the Mathcad Prime software built-in function: *Spline2*. To generate a new spline curve, it's necessary to define new vale of time step for the total time. For most devices which are recording the signal at real time is the time step is set to default value $\frac{1}{128} = 7.8125 \cdot 10^{-3} s$.

Function *Spline2* has three parameters, $x - vector$, $y - vector$, $n -$ degree, std-standard deviation. Degree defines cubic (n = 3) polynomial fits used in the B-spline. Function *stdev* returns the square root of the population variance of the elements in input matrix *M* as follows:

$$std = \left(\frac{1}{m \cdot (n-1)} \right) \cdot \sum_{i=0}^{m-1} \sum_{j=0}^{n-1} \left(M_{i,j} - mean(M) \right)^2 . \quad (5)$$

Function *Spline2* :

$$spline = Spline2(x, y, n, std) . \quad (6)$$

To determine the approximation accuracy, we used the autocorrelation function in the next form:

$$Acf(r) = \frac{1}{n-r} \sum_{i=1}^{n-r} \overline{M}_i \cdot \overline{M}_{i+r} \text{ , where } \overline{M} = M(t) - \overline{M} . \quad (7)$$

Results

Curve approximation algorithm

For new approximated dataset we set $\Delta t = 0.007813$ s and the dimension of dataset $\text{imax} = \frac{t}{\Delta t} = \frac{6.4}{0.007813} = 819$ items. Then data range we set up as follows:

$$range_i = \frac{i \cdot \left(\max\left(x\right) - \min\left(x\right)\right)}{\text{imax}+1} + \min\left(x\right) \tag{8}$$

To generate spline curve, we used the Mathcad function *Spline2*. The first element of vector *spline* is the B-spline order. The second element gives the number of intervals (*knots* - 1). The next elements are the knot values. The remaining elements contain the coefficients for the B-Spline basis functions. The $y_F\left(t\right)$ function correspond to the array $spline^{\langle 0 \rangle}$.

$$spline = Binterp\left(range, y_F\right)^T. \tag{9}$$

The first and last knots, when automatically generated, match the endpoints of the original x-data. To generate the range, we used the *Binterp* function for a range of values that matches the range of *x*. The newly generated dataset ais depicted in figure 3. The autocorrelation function for both dataset of tractive forces are depicted in figure 3.

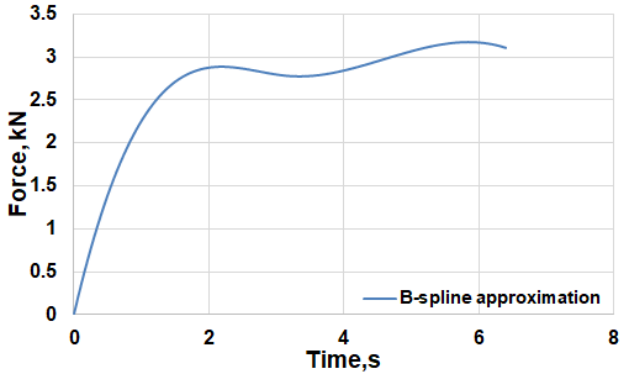

Figure 3. B-spline approximation of force

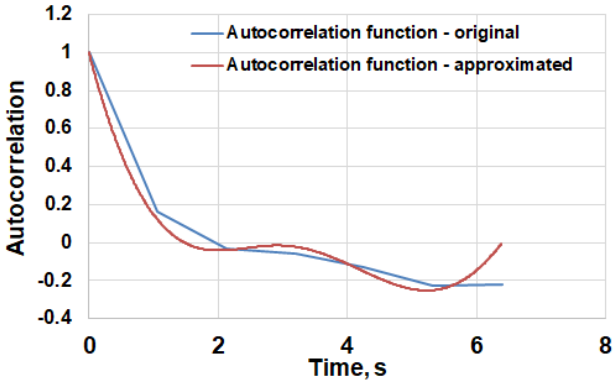

Figure 4. Autocorrelations

For solving the driving force, we used the equation published by Alcock (1986) as follows:

$$F_D = F_t \cdot \left(1 + f \cdot \tan(\alpha)\right) + f \cdot G_t \text{ , where:} \tag{10}$$

f - rolling resistance = 0,12 for stubble field, G_t - tractor mass force = 62,7kN. The calculated driving force under rear tire of tractor is depicted in the figure 5. Standard error of the driving force we calculated in Mathcad as follows:

$$\begin{gathered} slp := \text{slope}\left(range, Fd\right) = 2.726 \cdot 10^3 \\ icp := \text{intercept}\left(range, Fd\right) = 2.558 \cdot 10^4 \\ Nr := \text{rows}\left(Fd\right) = 820 \\ SE\_slopeFd := \sqrt{\frac{\sum_{i=1}^{Nr}\left(Fd_{i-1} - \left(slp \cdot range_{i-1} + icp\right)\right)^2}{\left(Nr-2\right) \cdot Nr \cdot \text{var}\left(range\right)}} = 82.249 \end{gathered} \tag{11}$$

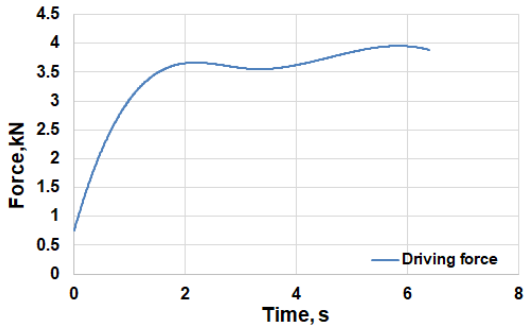

Figure 5. Driving force

where, F_d is evaluated traction force. Spearman correlation coefficient was solved by Mathcad function *corr* with *rank* of *range* array and *rank* of F_d array. We got the value Spc=0.902. Pearson correlation factor was solved with *corr* function but input parameters was *range* and *Fh* . We got the value Psc=0.757. Standard error of regression solved by eq. 11. We got the value SE_SlopeFd=82,249 N. If we assume that the maximum value of driving force is F_d=3,9547.10^4N and its equal to 100%, calculate percentage error of regression is 2,08%.

Discussion

Determining the driving force from tractive force is based on experimental measurement provide by Slimařík (2015). Some important conclusion missing from his work. For this reason, we set the methodology to determine the driving force. We took a tentative solution the tractive force by Goryatchin equations as mentioned Cerović et.al.(2020), but our results did not lay with our modelled results. Porteš et.al (2013) tried to develop the mathematical model for simulation of forces between the tractor and implement, but they fail. For the major input parameters of mathematical model is to impossible specify it, with acceptable accuracy.

Conclusions

We developed a methodology how to determine the driving force of tractor with mounted implement. For our purpose we utilized the dataset from real experimental measurement finished by Slimařík (2015). From measured drawbar pulls we extracted the x-components of forces and solved the resultant tractive forces dataset (eq.4). For curve approximation we used the Mathcad Prime functions defined upper. We also solved the error of approximation where we got the error 2,09%. For comparison of original dataset with approximated function

we solved the autocorrelation functions for both dataset (fig.4). Regression coefficient has been also calculated. We could assume that presented methodology has fair results which are confirmed with values of Pearson correlation factor (0,757) and Spearman correlation factor (0,902).

Acknowledgment

This publication was supported by the Operational Program Integrated Infrastructure within the project: Demand-driven research for the sustainable and innovative food, Drive4SIFood 313011V336, co-financed by the European Regional Development Fund.

References

[1] Alcock, R. (1986) Tractor- Implement systems. The AVI Publishing Company, Inc.001: 10.1007/978-1-4684-6879-3

[2] Bandy, S. M.- Babacz,W.A.-Searcy,S.W.- Stout, B. A. (1986) Measurement of Three-Point Hitch Forces on Agricultural Tractors. SAE Technical Papers Series 861255. International Off-Highway & Powerplant Congress & Exposition Milwaukee. Wisconsin September 8-11. 1986. ISSN 0148-7191

[3] Battiato,A. -Diserens,E.(2017) Tractor traction performance simulation on differently textured soils and validation: A basic study to make traction and energy requirements accessible to the practice, In Soil and Tillage Research, Volume 166,(2017) p. 18-32, ISSN 0167-1987, https://doi.org/10.1016/j.still.2016.09.005.(https://www.sciencedirect.com/science/article/pii/S0167198716301891)

[4] Cerović,V. - Milković, D. - Grbović, A.- Petrović D.-Simonović, V. (2020) 2D Analytical Model for Evaluation of the Forces in the Three-point Hitch. In Mechanism, In Journal of Agricultural Sciences (Tarım Bilimleri Dergisi) 26, (2020) p.271-281

[5] Porteš,P.- Bauer,F. Čupera, J. (2013) Laboratory-experimental verification of calculation of force effects in tractor's three-point hitch acting on driving wheels, In Soil and Tillage Research, Vol. 128, (2013), p. 81-90, ISSN 0167-1987, https://doi.org/10.1016/j.still.2012.10.007. (https://www.sciencedirect.com/science/article/pii/S0167198712002279)

[6] Rédl, J.- Maga, J.- Findura, P. - Kalácska, G. - Kalantari, D- - Bango, J. (2021) Assessment of ploughing stability. In Mechanical engineering letters. Gödöllő: Szent István University, 2021, p. 150-165.

[7] Slimařík, D. (2015) Analysis of force effects on the output parameters of plowing sets. Dissertation thesis (supervisor: prof. Bauer, F.) (Czech: Analýza silových účinků pluhů na výstupní parametry orebních souprav, Disetarční

práce) Mendel University in Brno, Agronomy faculty. Available on: https://theses.cz/id/jcmutt/16950130 [Accesed:01.01.2023]

On the go soil sensor development in AGIT FIEK programme

János HORVÁTH[1,2], Péter KORZENSZKY[2], László KÁTAI[2], István SZABÓ[2]
[1]Doctoral School of Mechanical Engineering, MATE, Gödöllő
[2]Institute of Technology, MATE, Gödöllő

Abstract

Nowadays agriculture faces the challenge of feeding more and more people all around the world while natural resources are running out. Digital technologies can help farmers produce safe, sustainable, high-quality food while contributing to the fight against climate change. Due to digitalization, a paradigm shift occurred in agriculture, which boosted sensor technology's rapid development, especially soil sensors. Using sensors and the digital knowledge of soil properties, farmers can better understand the needs of the fields and cultivated plants on a micro-scale, thereby saving resources and putting less strain on our environment. The relative salinity of our soils is an important topic because the need to replace salt and its quantity has an impact on production costs and yield. Currently, the standard method for determining soil selective salinity is based on an expensive and time-consuming laboratory test method. The future of site-specific crop production is moving towards a sensor-based on-the-go measurement approach because obtaining important soil characteristics quickly and cheaply is still one of the biggest challenges in precision agriculture today.

Keywords

electrical conductivity, soil salinity, digital agriculture, on-the-go measurement, proximal topsoil sensor

1. Introduction

Today, sensor technology is one of the fastest-growing areas of technology. A sensor is a device that can detect a change in the physical or chemical environment, which then converts it into electrical signals, both electric current and voltage. The precision agriculture mainly relies on real-time monitoring of soil conditions using information technology and GPS technology and then analysing and managing the spatial-temporal variability of soil and field crops. This information helps make the decision on the precision application of crop inputs including water and fertilizer. It can improve efficiency and reduce the losses of water and fertilizer (Popp et al., 2018). With the correct and sensible use of sensor technology, farmers can better understand their crops and soils while

conserving resources and at the same time saving resources and reducing their impact on the environment (Horváth&Schmitz, 2019).

Due to increases in the cost of fertilizer production inputs—predominantly nitrate (N), phosphate (P), and potassium (K) those in agriculture are looking for ways to optimize plant yield while minimizing the application and consumption of fertilizer. Since these macro-nutrients vary even on a small scale throughout a cultivated field, numerous researchers have attempted to develop an on-the-go sensing apparatus that can map the presence of these chemicals in situ so that this map, once overlaid with parameters such as pH, electrical conductivity (EC), crop yield, and mechanical properties of the soil, can give a precise spatially varying prescription for fertilizer application (Sinfield et al., 2010).

The global Agricultural Sensors market was valued at USD 1,505.4 million in 2020 and is expected to reach USD 3,200.8 million by the year 2028, at a CAGR of 11.04%. Smart Sensors allow farmers to maximize yields using minimal reserves such as fertilizer, water, and seeds. By utilizing sensors and mapping fields, farmers can commence realizing their crops at a micro-scale, conserve resources, and lessen influences on the ecosystem. Smart agriculture has roots moving back to the 1980s when the Global Positioning System (GPS) capability became accessible for civilian use. Once farmers were able to map their crop fields accurately, they could monitor and use fertilizer and weed treatments only to parts that required it. During the 1990s, early precision agriculture users implemented crop yield monitoring to create fertilizer and pH correction suggestions. As more variables could be calculated and entered into a crop model, more accurate recommendations for fertilizer application, watering, and even peak yield harvesting could be made. The device captures analyses and transmits information like temperature, humidity, pressure, water content, etc. using radio signals. It gathers the data and sends it to the base station. The base station then analyses the data and carries it for further processing. Usually, sensor networks have a base station known as a sink and several other sensors too, which sense and transmit the signals along with sending information to other nodes. Weather stations are self-contained units placed at various sites throughout growing fields. These stations have a mixture of sensors suitable for the local crops and climate. Data such as air temperature, soil temperature at various depths, dew point temperature, wind direction, relative humidity, rainfall, leaf wetness, chlorophyll, wind speed, solar radiation, and atmospheric pressure are measured and recorded at predetermined intervals (Agricultural Sensor Market, 2021).

2. Experimental

On the go soil sensors in the practice

Obviously, the dealers or service providers build their digital product portfolio for business reasons and expect business results from precision technologies. This is a very good reflection of how the market sees the use of digital products. In 2020, 92% of retailers in the USA offer some type of precision agronomy service to their

customers (Erickson et al., 2020). The Ericksons asked the responding dealers to describe what they currently offer in precision services and what they will offer three years from the survey, now the Soil EC mapping service increase is predicted in the portfolio at 16% of the dealers in 2023. The following answers were received (see Fig. 1):

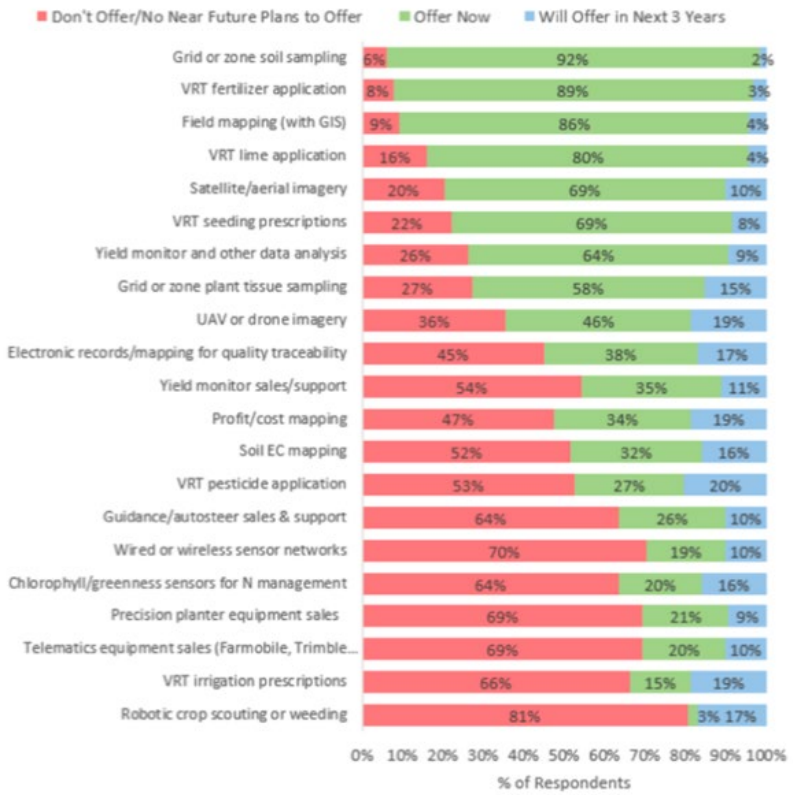

Figure 1. The precision services recommended by the interviewed dealers in 2020 and in 3 years future

Erickson also investigated the possible development paths of technologies based on digital cognition, i.e. perception, where the Soil EC mapping service will reach at 46% (see Fig. 2):

From the growth forecast of solutions using sensors, it is very easy to recognize that the future of site-specific crop cultivation points towards a sensor-based approach. But it is not yet a fully settled question whether proximal sensors that monitor the properties of the upper layer of the soil and/or sensors that remotely detect some property of the plants will be the ones that will be the runners-up (Lowenberg-DeBoer&Erickson, 2019). In our opinion, both solutions should be considered separately and in combination. But there is an important difference,

while the measurement with sensors close to the ground is a direct measurement because the properties of the soil are measured directly, while the measurement of the plant's development with remote sensing is only a conclusion about the state of the soil, i.e. an indirect measurement method. In the following, focusing specifically on sensors close to the ground, we will present how tools and solutions based on such sensors can be encountered in site-specific plant cultivation.

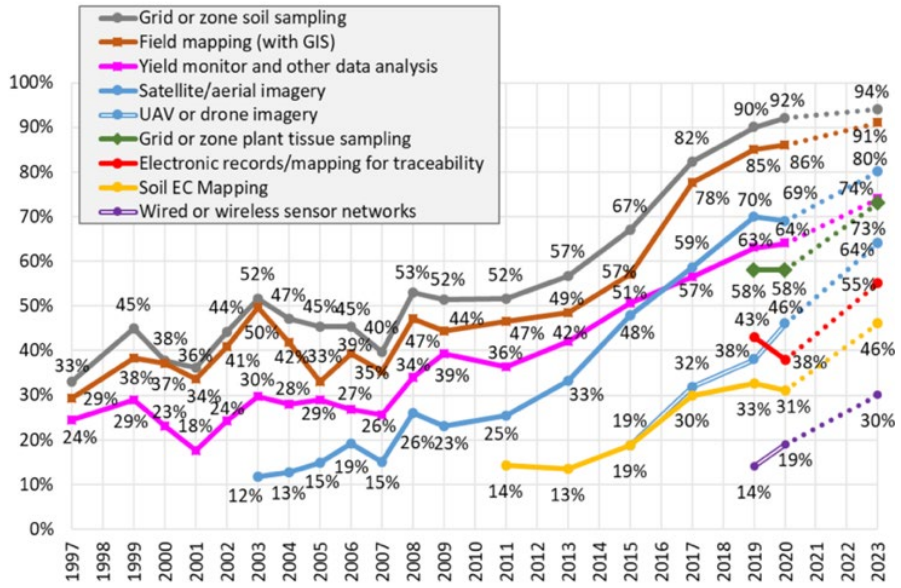

Figure 2. The range and future development of precision services related to sensing by the interviewed dealers

Proximal topsoil sensors

According to the definition of proximal (near ground) sensing, signals are obtained from the ground by using sensors used in the field, so that the measuring unit of the sensor is in contact with the ground or stays close to it (within 2 m) (Viscarra Rossel et al., 2011).

The following measurement principles and sensors are distinguished in practice (Grunwald et al., 2015):

- **Electrical conductivity measurement:** Electrical conductivity (EC) is the ability of a material to conduct electricity. Soil is a three-phase system consisting of water, air, and organic and mineral matter, and offers multiple pathways for conduction between phases with different ECs. There are two types of sensors in practice: an electrode-based and an electromagnetic induction-based.

- **Penetrating radar and reflection measuring devices (reflectometer):** Ground penetrating radar (GPR), time-domain reflectometer (TDR) and frequency-domain reflectometer (FDR) measure the dielectric constant of the soil, which describes how easily an electrical current can be generated in the soil. field when current is introduced into it. They follow the same measurement principle as the EC meter, but they work based on electrical force rather than current.
- **Diffuse reflectance sensors:** Visible (VIS) or near-infrared (NIS) or mid-infrared (MIS) diffuse spectroradiometers measure soil reflectance, that is, the proportion of incoming (incident) light that is reflected by the soil. The incident energy (light) emitted by the artificial light source interacts with the ground, and the reflected energy (light) is measured and processed to produce a continuous spectral curve, representing the reflectance by wavelength.
- **Magnetic susceptibility sensors:** Magnetic susceptibility sensors measure whether a material becomes magnetic when a magnetic field is applied. Magnetism in soil depends on the type and concentration of minerals that can be magnetized, mainly iron minerals. High-mineral iron minerals found in soil are magnetite and maghemite, but other low-mineral minerals occur in higher concentrations in soil, including hematite and goethite. These iron-containing minerals are associated with other soil constituents (mineral and organic) and their concentrations are related to the original concentrations of the parent material. The formation and dissolution of these magnetic iron minerals is controlled by soil pH and soil drainage (which includes moisture content and texture). Thus, the magnetism of soils can be used to estimate the concentration of minerals in the soil, but also by correlation of other components of the soil.
- **Gamma-ray spectrometer or gamma-radiometers** measure the energy emitted by the soil in the form of gamma radiation. Gamma radiation with a wavelength of about 0.001-0.1 nm comes from the decay of radioactive isotopes naturally present in the soil. The most common of these, which are used in practice in geophysics, are potassium (40K), bismuth (214Bi) and thallium (208Tl), where 214Bi and 208Tl are decay products of uranium (238U) and thorium (232Th)., and are used to estimate the concentration of these elements. In addition, man-made cesium (137Cs) or metastable barium (137Ba). Gamma-radiometers work by measuring kinetic energy at energy levels typically between 0 and 3 MeV. Gamma-ray spectra can be analyzed completely similarly to VIS-NIR-MIR spectra with multivariate analysis. Gamma radiometry has played a role in the creation of digital soil maps, as it can characterize soil properties (van Egmond, 2010)
- **Other promising measurement principles:** Currently, research is being done with the following soil sensors and measurement principles without claiming to be complete: X-ray beam, ion-selective electrodes,

photoacoustic spectroscopy, laser-induced fluorescence spectroscopy, inelastic neutron scattering.

- Of course, the different sensors can be combined as desired, in this case we are talking about **multi-sensor use**, in which case several properties can be mapped simultaneously.

Commercially available tools and solutions based on proximal sensors, i.e., soil scanners

The quick and cheap acquisition of important soil characteristics remains one of the biggest challenges of precision agriculture for digital agriculture, i.e., Agriculture 4.0. Many researchers and manufacturers are trying to develop on-the-go soil sensors to directly measure the mechanical, physical, and chemical properties of soil. The disadvantage of the practical use of near-ground sensors, which are becoming more widespread, is that their accuracy is not as good as that of individual sampling and tests carried out in the laboratory, but the advantage is that they are suitable for quick measurements and are relatively cheaper, so they are suitable for practice (Hajdú, 2018). With the use of devices that enable faster and more cost-effective measurements, mechanized soil testing and nutrient mapping solutions become available in a wide range of areas. In 2023, the following tools can be found in precision agricultural practice:

- Veris mobile soil scanners, which physically measure the soil's electrical conductivity, and optically measure the soil's organic matter (humus) content and determine the soil's pH value. The Veris MSP3 (see Fig. 3) soil scanner is a unique sensor platform that can be used to represent 4 important soil variables during one operation. The Veris soil scanner consists of 3 sensor systems that also measure separately. At a working speed of 8–15 km/h, the system measures soil acidity (pH), organic matter percentage and soil conductivity (EC) at the growth depth (0–30 cm) and in the root zone (0–90 cm).

Figure 3. Veris MSP3 in action (VERIS homepage)

- **Topsoil Mapper (TSM) soil scanner** (see Fig. 4), Developed by Geoprospectors GmbH in Austria, partly owned by CNHi. The TSM soil scanner emits a signal generated by electromagnetics into the tested soil and measures the conductivity of the soil up to a maximum recording depth of 1.1 m, considering the device's approximately 35 cm height from the ground. Since the sensor is not in contact with the ground, the recording speed of the measurement can reach up to 30 km/h, if the ground allows it. The equipment is ISOBUS-compatible, and since 2017 the ISOconnect version of TSM is also available as the first ISOBUS-compatible soil sensor. The big advantage of this option is much easier handling, as it is a plug-and-play solution and only one terminal is needed. The operating concept of the TSM: Electromagnetic sensors detect soil compaction in a non-contact manner during each pass. The soil compaction values are transmitted in real time to the tractor's task controller computer (TC - task controller) via the ISOBUS connection, and the tractor can then and there control the working depth of the implements of the tillage machine capable of working with variable tillage depth, i.e. the tillage implement with individual depth control in real time able to work. It should be noted that this soil sensing technology is also part of CNH Industrial's AGXTEND innovative technologies platform portfolio. CNH Industrial markets Topsoil Mapper in Europe as SoilXplorer (Topsoil Mapper website)

Figure 4. TSM in action (TSM homepage)

- **Geonics EM38 MK2 soil scanner**. The equipment developed by the Canadian Geonics Limited also works on the principle of electromagnetic induction. The standard EM38-MK2 uses two receiver coils, 1m and 0.5m from the transmitter, respectively, and provides soil conductivity (EC) data from a depth range of 1.5m and 0.75m when positioned in the vertical dipole direction, and 0.75 m, or from a depth range of 0.375 m when it is in the horizontal dipole direction. Based on the conductivity index, the physical composition, compactness, humus content, nutrient and water supply of the soil can be deduced. This equipment is also towed on the ground and performs measurements in contact with it. The optional collapsible calibration stand supports the automation of the instrument calibration procedure. The stand-mounted instrument can be calibrated in seconds without the need for repeated adjustments.
- **SoilOptix soil scanner** (see Fig. 5) uses a non-contact, pre-calibrated gamma radiometer sensor that is mounted on a vehicle approx. 60 cm from the ground to measure 137Cesium, 238Uranium, 232Thorium and 40Kalium in the upper part of the soil. The sensors can work in various weather conditions, and their accuracy is not affected by the presence of plant remains. SoilOptix provides 827 data points per hectare, allowing for high-resolution visualization of fields. The measurement results, in up to 25 map layers, are provided by the own software, with subsequent data processing.

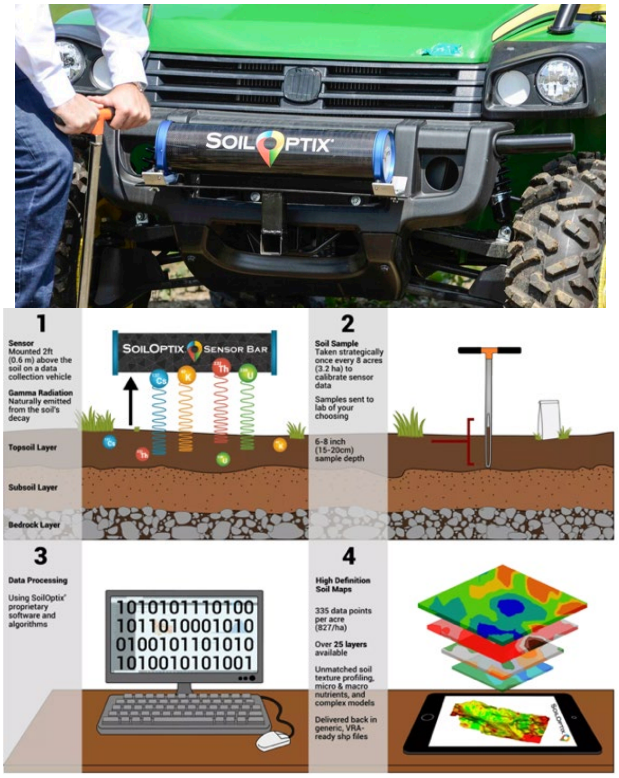

Figure 5. The device and data processing principles (Soiloptix homepage)

Medusa MS-2000 soil scanner (see Fig. 6) developed by Medusa Radiometrics BV from the Netherlands. They developed the SoilOptix soil scanner in a joint project with the University of Gröningen. In 2019, they decided to commercialize the sensor themselves.

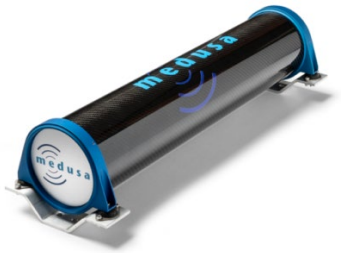

Figure 6. The Medusa MS-2000 device (Medusa homepage)

The following Table 1 will show the current soil sensors offer in the market.

Table 1. The grouping of proximal sensors, i.e., ground scanners, based on their typical properties (Horváth et al., 2021)

Type of soil sensors	VERIS MSP3	TOPSOIL Mapper	GEONICS EM38 MK2	SoilOptix	MS-2000
Producer	Veris Technologies Inc.	Geoprospectors GmbH	Geonics Ltd.	SoilOptics Inc.	Medusa Radiometrics BV
Origin	USA	Austria	Canada	Canada	The Netherlands
Measurable parameters	EC OM pH	Multi Coil Array (RX / Tx)	EC	pH, OM, P, K, Ca, Mg, %clay, %sand, % sludge, available water	pH, OM, P, K, Ca, Mg, %clay, %sand, % sludge, available water
Measurement principles	Electrical conductivity Optical sensor pH electrodes	Electromagnetic induction	Electromagnetic induction	Gamma radiometry	Gamma radiometry
Penetration depth	even 0.9m	even 1.1m	even 1,5m	topsoil	topsoil
Soil contact	Yes	contactless, from 25-40cm	Yes	contactless, from 60cm	contactless, from 60cm
Working speed	7-13kph	theoretically max. 50kph	N/A	up to 20kph	up to 20kph
Working width	15-24m	18m	N/A	12-15m	12-15m
Performance	8-26ha/h	36ha/h with 20kph	N/A	N/A	N/A
Device weight	635kg	32kg	5.4kg	N/A	12 kg
ISOBUS capability	N/A	Yes, as option	N/A	N/A	N/A
Data processing	real-time with own app	real-time with own app	real-time with own app	post processing with own app	post processing with own app
Data format	N/A	OGC (GIS consortium), SHP, GTIFF or ISOXML	N/A	SHP, CSV	SHP, CSV
External GNSS receiver	required	required	required	required	required
Mounting	tractor, quad	tractor, quad	in hand	tractor, quad	tractor, quad
Webpage	https://www.veristech.com/the-sensors/msp3	http://www.geoprospectors.com	http://www.geonics.com/html/em38.html	https://soiloptix.com	https://medusa-online.com/en/about/

3. Results and discussion

Measurement Process Development at Institute of Technology

Recognizing the trends presented previously, the sensor technology is one of the fastest developing areas of today's Precision Agriculture. We are also researching at the Hungarian University of Agriculture and Life Sciences Technical Institute how to make the current implement range smarter and extract valuable information from the soil. Currently, farmers are not yet fully prepared to generate added value for their business from the ever-increasing amount of data, so the future depends on those professionals who can transform the farmer's data into valuable information and appear on the market with new value-added services. A monetizable, value-added service requires a measuring device, a measurement principle, a large amount of data, and easy-to-use information. Useful information for the farmer must be generated from the available data so that a direct, concrete

action plan can be prepared in the form of application maps. Based on the data collected by sensors about machines and their work, the success or failure of new services in digital agriculture depends less on the willingness of the farmer to share the data than on the reliability and easy understanding of the added value for the farmer.

Soil conditions are the most important drivers of biochemical processes and biological activity in the soil, which in turn influence ecosystem properties, including plant growth and ecosystem carbon exchange. To better understand these relationships, automated sensors can continuously monitor soil properties. The measurement results assigned to the geolocation can be added to a geospatial database, which facilitates the preparation of application maps for farmers and precision agriculture providers. The aim of our work is to invent a measurement principle in site-specific plant cultivation that:

- Continuously provides information on-the-go,
- about the properties of the topsoil so that the collected information,
- is processed in real-time,
- taking advantage of the options provided by the ISO 11783 (ISOBUS) standard, assigned to RTK based geo-position,
- using the internet,
- be transmitted via the cloud-based service,
- into the user/consultant's GIS/FMIS system where the measurement data is processed and
- valuable information can be extracted to prepare subsequent application plans.

The goal of our tests is to develop a measurement principle that can be used to determine the selective salinity of the soil in the upper layer of the soil using a soil scanner that works on the electrical conductivity principle developed within the framework of AgIT FIEK. For this, we used the mobile device carrier and the soil trough located in the laboratory of the Technical Institute, so that by eliminating disturbing conditions, the soil sensor's later operating environment in the field can be well simulated. The subject of the tests was a sensor for determining soil parameters, consisting of three working elements, mounted on the front three-point suspension of a power machine. The cultivation elements made of wear-resistant steel are also sensors suitable for measuring electrical conductivity (EC). During the tests, we covered the examination of the sensor in a stationary position, which, in terms of its circumstances, did not differ much from the test of functionality during movement. The results of the test in a stationary position will also be the reference values for the signal sequence provided by the normally moving measuring unit. Both measurements were made with a high-precision Sourcetronic ST2829C LCR meter. During the measurement, the response function of the signal sequence of known frequency and amplitude issued to the cultivation element was determined. During the test, we simulated different soil

conditions in the case of soil mixed with different concentrations of KCl solution and $CaCl_2$ solution.

The new device

The object of the measurement is a sensor for determining soil parameters, consisting of three heads, which can be mounted on the front three-point suspension of a power machine (see Fig 7). Thinner soil-driven cutting discs were installed in front of the sensor elements, which prepare the soil for measurement by cutting its top layer. The same discs also cut plant remains, reducing their effect on the measurement results. The depth of penetration into the soil is ensured by the two-sided rims of the discs.

Figure 7. Device carrier, measuring instrument and implement in test position prepared for measurement

Behind the disks, there are the knife type sensor electrodes made of wear-resistant steel (see Fig. 8), which are arranged in a row. Their distance can be adjusted between 200-500mm in steps of 25mm. They are isolated from the mounting frame with a polyamide block.

Figure 8. Sensor knife

The measuring elements are clamped to the ground independently by a spring-loaded structure. The frame creates a connection between the measuring elements and the suspension of the tractor. The measuring frame is self-adjusting around the vertical axis at an angle of ± 30º, thus following the tractor's direction of travel and ensuring that both sides of the sensors are in contact with the ground even when changing direction. The following Figure 10 shows the soil cultivation device consisting of three cultivation elements that can be mounted on the front three-point suspension of the power machine.

The goal of the measurement

The purpose of the measurement is to determine whether the electrical conductivity measurement soil sensor and soil tillage device included in the study and developed within the framework of the project can provide information about the current state of the soil in a stationary position and while moving. Conductivity is one of the characteristic properties of the soil condition. Can the cation content of the soil (e.g. Ca^{2+} and K+ content) be determined by measuring conductivity. The response function of solutions of known composition applied to soil at variable concentrations to a series of high-frequency signals is investigated using an LCR meter. During the measurement, the response function of the known signal sequence issued to two soil sensors and cultivation elements was examined as shown in the following image. During the measurement, solutions with predetermined molar concentrations are injected into the soil, and then we examine their detectability in the soil through the sensor elements.

The principles of measurement

Using the high-precision SOURCETRONIC ST2819A LCR meter ensured that it always provides constant excitation at its output through a four-wire measuring system and detects the response function from the soil sensor. The LCR meter instrument is extremely sensitive to disturbing signals from the environment, therefore a special measurement method was developed to eliminate them. The

instrument generates a series of signals with a known frequency, known amplitude and known period at its output in accordance with the set parameters. The following Table 2 shows the current output test parameters set for the instrument.

Table 2. The output parameters of the instrument

Output function	**Output voltage UAC [V]**	**Frequency range used f [Hz]**
Sinus	10V	20, 50, 100, 250, 500, 1000, 2000, 5000, 10000, 50000, 100000, 250000, 500000, 750000, 1000000

The LCR meter measures the amount of phase shift (ϕ) between the output function and the response function and calculates the following values (see Fig. 9):

- **G** as Conductance [S];
- **B** as Admittance [S];

During the measurement, the LCR meter outputs the pre-programmed frequency sequence in automatic mode and measures the values of the response function obtained from it. The instrument is used in the "G–B" function, i.e. the values of "G" and "B" are stored on the external storage device connected to the USB port. The following figure shows a screenshot of the instrument during a measurement as an example.

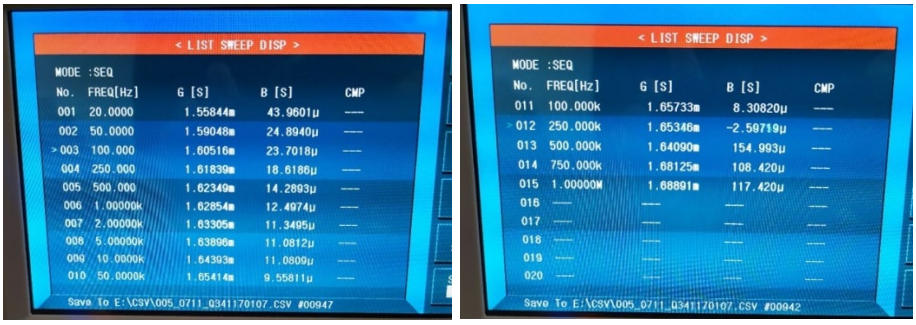

Figure 9. Screenshot of one measurement sequence

We receive the results in a CSV file, which was analysed in Microsoft Excel.

Conclusions

Today's solutions for devices using proximal soil sensors are relevant today and they will be relevant in site-specific agricultural practices in the future as well. Although the first digital agricultural solutions were already in the hands of

farmers in the 1990s, the sensor market has experienced a sudden boom in recent years as practical implementations have become available with the development of digitalization. Future sensor solutions will change the world of Precision Agriculture and are likely to affect the overall design of agricultural machinery. With the help of the proximal soil sensors, we will be able to measure the important soil properties in real-time and we will be able to intervene in the work operation promptly. By processing the data extracted in this way in real-time, a new range of services can be created, which will change the processes of precision crop production. There is no question, the development and use of sensors will increase the efficiency of site-specific crop production. This can already be treated as a fact. There are several solutions are available in the market competing for the user's wallet and this market will be expanded as the demand will certainly increase. We introduced and categorized the proximal soil sensors and presented our ongoing research of measuring process development. We are convinced that the solutions that measure the soil properties on the go directly from soil and process the collected data in real-time will be competitive.

Acknowledgements

We would like to acknowledge the Hungarian University of Agriculture and Life Sciences, Institute of Technology AgIT FIEK programme for the financial support and the for the great interest work and concession of their areas allowing this work could be carried out.

References

[1] Adamchuk V. I., Hummel J. W., Morgan M. T. and Upadhyaya S. K. (2004) On-the-go soil sensors for precision agriculture. Computers and Electronics in Agriculture 44(1), 71–91.

[2] Adamchuk V.I., Allred B., Doolittle J., Grote K. and Rossel R. (2015) Tools for proximal soil sensing. Soil Survey Staff, Ditzler, C, West, L(Eds), Soil Survey Manual Natural Resources Conservation Service US Department of Agriculture Handbook 18.

[3] Erickson B. and Lowenberg-DeBoer J. (2020) Precision Agriculture Dealership Survey, Departments of Agricultural Economics and Agronomy, Purdue University, https://ag.purdue.edu/digital-ag-resources/wp-content/uploads/2020/11/CropLife-Report-2020.pdf (Accessed: 04.01.2023)

[4] Grunwald S., Vasquesy G.M. and Riverox R. G. (2015) Fusion of Soil and Remote Sensing Data to Model Soil Properties, Advances In Agronomy 131, 1-109.

[5] Hajdú J. (2018): Quick soil analysis and soil mapping, Agronapló 2018/9, 65-67 (in Hungarian)

[6] Horváth J. and Schmitz B. (2020) Digitalisation in agriculture – From the perspective of a global agricultural machinery producer. HUNGARIAN AGRICULTURAL ENGINEERING, 36. pp. 63-68
[7] Horváth J., Kátai L. and Szabó I., (2021) On-the-go soil sensors in Precision Agriculture, Mezőgazdasági Technika, 62/10, 2-5 (in Hungarian)
[8] Lowenberg-DeBoer J. and Erickson B. (2019) Setting the Record Straight on Precision Agriculture Adoption, Agronomy Journal 111/4, 1552-1569
[9] Medusa homepage, https://medusa-online.com/en/products/sensors/ (Accessed: 04.01.2023)
[10] Popp J., Erdei E. and Oláh J. (2018) Outlook of precision farming in Hungary. International Journal of Engineering and Management Sciences (IJEMS) 3/1, 133-147 (in Hungarian)
[11] Reports and Data (2020) Agricultural Sensors Market Analysis, By Type By Application Forecasts To 2026, https://www.reportsanddata.com/report-detail/agricultural-sensors-market (Accessed: 04.01.2023)
[12] SoilOptix homepage, https://soiloptix.com (Accessed: 04.01.2023)
[13] Topsoil Mapper homepage, https://www.topsoil-mapper.com/en/exclusive-emea-partnership-with-cnh-industrial/ (Accessed: 04.01.2023)
[14] Topsoil Mapper homepage, https://www.topsoil-mapper.com/en/bodenmanagement/ (Accessed: 04.01.2023)
[15] Trosin M., Dekemati, I. and Szabó I. (2021) Measuring Soil Surface Roughness with the RealSense D435i, ACTA POLYTECHNICA HUNGARICA 18/6, 141-155.
van Egmond F.M., Loonstra E.H. and Limburg J. (2010) Gamma Ray Sensor for Topsoil Mapping: The Mole. In: Viscarra Rossel, R., McBratney, A., Minasny, B. (eds) Proximal Soil Sensing. Progress in Soil Science. Springer, Dordrecht, 323-332
[16] VERIS homepage, https://veristech.com/soil-scanning-carts/ (Accessed: 04.01.2023)
[17] Viscarra Rossel R.A., Adamchuk V.I.,.Sudduth K.A., McKenzie N.J. and Lobsey C. (2011) Chapter Five - Proximal Soil Sensing: An Effective Approach for Soil Measurements in Space and Time, Advances in Agronomy 113, 243-291

Design of an autonomous differential drive vehicle

Gergely HALÁSZ, Viktor Ferenc ERDÉLYI
Department of Mechatronics, Institute of Technology, MATE, Gödöllő

Abstract

Nowadays in the world of industry, the usage of autonomous self-navigating robots, vehicles are becoming more and more relevant. These robots often use differential drive for its easy control and reliability. The subject of this paper is to show the developmental process of such a vehicle with the usage of FDM 3D printing and basic odometry software featuring ROS2.

Keywords

autonomous vehicle, differential drive, Arduino, Raspberry Pi, ROS2, FDM 3D printing

1. Introduction

Autonomous self-navigating robots often used to move cargo in warehouses, or components between workstations in a factory environment, we can even find them in homes as robot vacuum cleaners. Today's robot vacuum cleaners can map the whole house's footprint and calculate unique cleaning paths every time, and after finishing they can navigate back to their charging station. (Majumdar, 2014) A fair amount of these robots are based on the usage of a so called differential drive platform. These platforms use the differences in velocities of its wheels on each side to move and navigate, and with that they offer an easy and effective way to control the vehicle's position. Differential drive robots can use external guide points, triangulating or GPS to navigate, but almost all of them have some form of odometry based on wheel velocities. (Gregor Klancar, 2017) The focus of this paper is the initial geometric, hardware, and software design developmental process of a custom-made self-driving capable vehicle, with basic wheel velocity based odometry data calculation.

2. Matherials and methods

Geometric design of the robot's mainframe and internal components
Usually, differential drive robots utilize two driven wheels (one on each side) and one or two caster wheels for support and balance. These types of contraptions tend to be incapable of effectively navigating through rough surfaces or more challenging terrain due to the caster wheels smaller radius. For this reason, this

projects robot utilizes four driven wheels (two on each side), and no caster wheels. However, this means that the control of the robot becomes more complicated as the four contact point provided by the four wheels makes it impossible to turn the robot without the skidding of the contact points, hence the more appropriate classification as a skid drive robot.

The robot's mainframe got modelled first in Autodesk Inventor 3D modelling software, with the intention of making the rest of the components installation in it as easy and free as possible, with future upgrades and modifications in mind. The geometric dimensions were determined by the already acquired motors and their gearboxes. Consequently, the enclosure dimensions were 220mm (width) x 418mm (length) x 110mm (height). With these dimensions, the wheels points of contact with the ground fall exactly on the four corners of a regular square.

After the mainframe was finished, the following phase involved modeling the four motor fixtures, whose purpose it is to keep the motor housing from shifting under heavier loads. After then, a variety of sensor consoles and internal consoles for the electrical components were designed; these are simple to modify and install for a variety of sensors and instruments because the mainframe offers a variety of installation points and methods. Finally, the encoder discs and wheel assembly got modelled, then all the different components and parts have been printed by a modified Ender 3 FDM 3D printer, using PETG and TPU filaments. (CENTERS, 2017)

Electrical design

The circuitry had to be designed to achieve two different voltage levels, as the motors require a higher voltage level than the control electronics to operate. Two Arduino development board, an Arduino Mega 2560 and an Arduino Nano, were utilized in the control electronics. Four motor controllers and eight optical sensors are connected to the outputs of the Arduino Mega, while the Arduino Nano handles several ultrasonic sensors. A Raspberry Pi has also been installed, which is responsible for running the code of the ROS2 framework, communicating with the two Arduinos via a serial port. To connect the motor controllers and the optical sensors to the Arduino, had to be made separate connectors using pin headers and pin header sockets. In designing these, had to be ensured that they could only be connected in the correct orientation to avoid problems later.

To power the device, batteries, a battery charge controller, and DC-DC buck converters were used. The nominal voltage of the battery module is 12V, which is supplied directly to the motors via the motor controllers. Two switching buck converters were also connected to the batteries to supply the necessary power for the control electronics.

The power supply of the whole assembly can be interrupted by means of an external switch connected directly to the negative side of the output of the battery module. In this way, the whole device, except the battery charge controller, can be de-energized while maintaining the possibility of charging the batteries. The output of the battery charging controller is distributed via Wago terminals to the

motor controllers and buck converters. Battery charging is possible via a DC socket using a 12V voltage output adapter.

The batteries used were 18650 lithium-ion cells with soldering tips. These cells reach 4.2V when charged, but this was not sufficient to power the motors, so a 12V supply voltage similar to their original use was needed to achieve stable and trouble-free operation. To achieve this, three battery cells were connected in series. To increase the capacity, two more battery cells were connected in parallel with the three series-connected batteries, after bringing them to the same voltage level. As a result, the charge controller charges 3x3 cells.

A charge controller capable of balance charging, with a variable cell count from one to five, is used to control the charging of the batteries. This charge controller has a BM3451 IC, which contains the logic circuitry of the controller. The number of cells charged can be adjusted by connecting its outputs to a resistor. It stops charging the batteries between 4.21 and 4.29V voltage level and prevents them from discharging when the voltage range 2.72-2.88V is reached. During discharge, the maximum current service capability is 100A and the maximum charging current is 60A. The magnitude of the balancing current is 60mA.

The 10-12V voltage from the batteries is unsuitable for the control electronics, and without lowering the value, it would immediately lead to failure. For this purpose, DC-DC buck converter switching mode power supplies have been used, which are capable of generating a stable 5V voltage to meet the needs of the control electronics. Despite their small size, these power supplies are capable of delivering 3A current, with input voltages ranging from 4.5V to 24V. Their output voltage can be regulated by bypassing the outputs of the built-in resistive voltage dividers, between 1.8V, 2.5V, 3.3V, 5V, 9V, and 12V, but these are inaccurate in practice. To set an accurate value, it is possible to use a potentiometer on the back plate to set voltage levels with acceptable accuracy. Of the two power supplies used, one is used to power the Raspberry Pi and the other to power the Arduinos and the several sensors.

The wheels are driven by brushed DC motors from Parkside PBSA T2 D2 cordless handheld screwdrivers. Due to the design of the manual screwdrivers, the motors are fitted with heavy-duty two-speed planetary gearboxes, which are also been utilized. Thanks to the planetary gears, the motors are capable of 28Nm of torque and 350 or 1300 rpm.

To control the DC motors, one iBT-2 motor controller had been used for each motor. These motor controllers are capable of adequate power output for the motors due to their 40A current capability. They are powered by a BTS 7960 microchip. During their operation, the motor controllers receive PWM (pulse width modulation) signals from the Arduino. The motor controllers vary the magnitude of the output voltage applied to the motors as a function of the PWM signals. This means that, since the conditions limiting the rotation of the motors do not change, and hence the amount of torque to be applied, the speed of the motors can be varied by changing the voltage. The motor controllers thus allow the Arduino to change the speed of the wheels simply by outputting a given PWM signal.

The direction of rotation of a brushed DC motor can be changed by reversing the direction of the winding current in it. Depending on which input the motor controller receives the PWM signal, the internal H-bridges change the polarity of the motor controller output and thus the direction of the motor current. This allows the Arduino to change the direction of rotation of the wheels in addition to their rotation speed, using the PWM signal on its two outputs.

For the wheel's rotation speed control, four dual-channel incremental optical rotary encoders (one per wheel) had been made. The encoder disc got modelled in 3D design software.

The sensors that detect the teeth of the disc are ES011 type optical limit switch panels with mounted slot-opto. Since it is a dual-channel rotary encoder design, two sensors were assigned to each disc. During their operation, the sensors transmit the voltage they receive to the signal line in case their light beam is blocked, which is indicated by a green LED. Four of the signal wires (one per wheel) are connected to four of the six interrupt pins of the Arduino MEGA, while the other four are connected to standard digital inputs on it.

For the project HC-SR04 type ultrasonic sensors had been used. These sensors are equipped with four pins: one for the 5V supply voltage, one for ground, one "trig" input and one "echo" output. The "trig" input receives a signal from the Arduino, which causes the sensor to emit an ultrasonic pulse. When the return of the tone is detected, the sensor sends a signal from the 'echo' output, which is picked up by the Arduino.

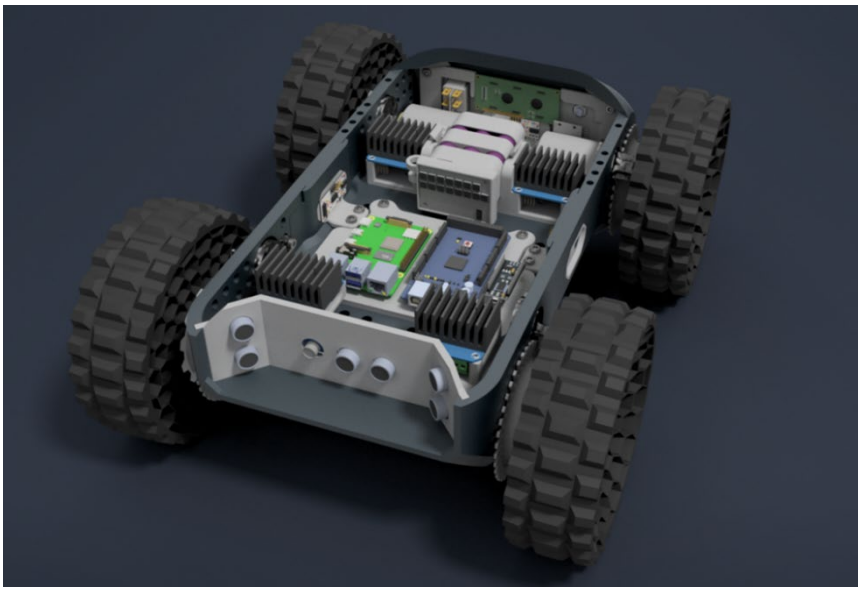

Figure 1. The robots 3D model with its internal components.

The Arduino calculates the time elapsed between the transmitted and the received signals and determines the distance measured by the sensor.
A Raspberry Pi 4 SBC is used to run the ROS2 framework. Despite its compact size and low power consumption, the Raspberry Pi has the right hardware background to run the computationally intensive tasks of ROS2.
To control the speed of the wheels and to process the optical sensors signals an Arduino mega 2560 development board is used, as it is equipped with a sufficient number of interrupt pins (6pcs) to allow program interruption, and the additional optical sensors and motor controllers could be connected to it too. However, there were not enough inputs for the ultrasonic sensors, and the stability of the code would have been questionable, so they were connected to an Arduino Nano development board. The final 3D model of the robot with the various internal component can be seen below in figure 1.:

Software design
Two codes are responsible for controlling the robot. One runs on the Raspberry Pi, which does the more complex computing, and one on the Arduino MEGA 2560 development board, which controls the motors and their associated hardware.

The code running on the Arduino controls the wheels motors based on the messages sent by the Raspberry Pi, and sends feedback to the Raspberry Pi about the position of the wheels.

The Arduino's code first reads the messages sent by the Raspberry pi on the serial port. The function only starts to spend time reading the serial port if there is data waiting in its buffer and the message processing code has already finished processing the contents of the previous message. The function considers the message complete after reading the '\n' terminator character at the end of the message, and only then signals to the message processing part of the code that the message array is updated and a new message is available. The message contains the robots desired linear and angular velocities.
Based on the message, the speed of the right and left wheels can be determined according to the equations below:

$$\omega l = \frac{(2 \cdot vel + rot \cdot L)}{2R} \tag{1}$$

$$\omega r = \frac{(2 \cdot vel - rot \cdot L)}{2R} \tag{2}$$

where:
ωl – angular speed of the left wheel [rad/s]
ωr – angular speed of the right wheel [rad/s]
vel – speed of the robot's centre point in the x-axis direction in its own coordinate system
rot – angular velocity of the robot about its z-axis
L – the distance between the wheels on the two sides
R – radius of the wheels

Knowing the angular velocity values of the right and left wheels, the value of the number of step changes per second that each wheel must perform can be determined. These values are then sent to PID controllers which are operating on the four wheels simultaneously independently from each other. The controller tries to implement the value of the determined position change, and compares the value obtained with the actual position change, the value of which is provided by the interrupt handling code part of the program. Consequently, it does not control for velocity but for position value, so that it is possible to achieve accurate distances.

The program's interrupt handler function is responsible for incrementing the value of the variables that store the position of the wheels using signals sent by the rotary encoders. In order to ensure that all signals received are processed, this function takes precedence over all other parts of the code. When a signal is received, the currently running program is aborted and the program interrupt handler function is started. After the function has completed its task, the interrupted code resumes execution at the point of interruption. To operate, it is necessary that the signals from the sensors on the Arduino are received at the dedicated interrupt input pins. At the end of a code cycle, the current position value of each hind wheel is sent towards the Raspberry Pi via serial port.

The code running on Raspberry Pi was written in python using the ROS2 framework. In the ROS2 framework, the parts of the program that performs a specific task and form a communication network with each other are called "nodes". One of the information channel types that allow nodes to communicate with each other is called "topic". Nodes can send messages to a topic (publish) and read messages from a topic (subscribe). A message sent by a node to a topic can be seen and processed by all nodes subscribed to that topic. A node can subscribe to and publish on multiple topics. The operation of a network built in this way is flexible and stable, the failure, stalling or restarting of one node does not affect the stable running of the other nodes. (Endre Erős, 2019)

The written code consists of a single node (drive node), this node is responsible for the communication with the Arduino and thus its control. The node subscribes to the "cmd_vel" topic from which it receives messages containing the speed commands to be executed and then instructs the Arduino to execute them. In addition, it processes the data returned by the Arduino and calculates the coordinates and velocities (odometry) of the robot in its environment. The calculated values are then published to the "odom" topic, allowing compatibility with additional ROS2 nodes.

The odometry function determines the position of the center of the structure's own coordinate system, its rotation about the z-axis in the environmental coordinate system, from the wheel step numbers supplied by the Arduino. The center and the angle of rotation of the environmental coordinate system are the same as the initial state of the coordinate system of the robot, so the function determines the relative displacement of the two coordinate systems. The resulting values are published to the "odom" topic every 0.1 seconds.

The code first determines the number of steps taken since the previous run, by determining the difference between the stored steps count and the freshly received steps in the message from the Arduino. Given the number of new steps (dl), the number of signals per revolution of the wheels (fl), and the radius of the wheels (r), it determines the new distance travelled by the wheels (s) in meters, according to the following equation:

$$s = 2\pi \cdot r \cdot \frac{dl}{fl} \tag{3}$$

where:
s – the distance travelled by the wheels
r – radius of the wheels
dl – change in the number of steps of the wheels
fl – number of steps of the wheels per revolution
By knowing the distance travelled by the wheels, it is possible to determine the length of the distance travelled by the robot and the magnitude of its rotation around its z-axis:

$$dc = \frac{(dl+dr)}{2} \tag{4}$$

$$dth = \frac{(dr-dl)}{l} \tag{5}$$

where:
dl – change in distance travelled by the left wheel
dr – change in distance travelled by the right wheel
dc – change in distance travelled by the robot's center point
dth – change in rotation of the structure about the z-axis

In the next step, the code determines the change in the coordinates of the structure in its surroundings, if the distance travelled by the two wheels are the same, using the following equations:

$$dx = dr \cdot \cos(th) \tag{6}$$

$$dy = dr \cdot \sin(th) \tag{7}$$

where:
dx – change along the x-axis
dy – change along the y-axis
th – the value of the stored past rotation about the z-axis

To the extent that the value of the change in the distance travelled by the two wheels differs, the robot moves along a circular arc of radius "R", the value of which is first determined according to the following equation:

$$R = \frac{dc}{dth} \tag{8}$$

where:
dth – change in rotation about the z-axis
R – radius of the instantaneous turning arc
The position of the arc's center point in the environmental coordinate system can then be determined:

$$iccX = x - R \cdot \sin(th) \tag{9}$$

$$iccY = y + R \cdot \cos(th) \tag{10}$$

where:
iccX – the x-coordinate of the centre of the instantaneous curvature curve (ICC)
iccy – the y-coordinate of the centre of the instantaneous curve of curvature (ICC)
x – the x coordinate of the position of the structure in the stored environmental coordinate system
y – the y coordinate of the position of the structure in the stored environmental coordinate system

By knowing the center of the arc, the changes in the coordinates of the robot's center point can be determined:

$$dx = \cos(dth) \cdot (x - iccX) - \sin(dth) \cdot (y - iccY) + iccX - \text{x} \tag{11}$$

$$dy = \sin(dth) \cdot (x - iccX) - \cos(dth) \cdot (y - iccY) + iccY - y \tag{12}$$

The stored x, y and th values can be updated to reflect the change in coordinates. The values dx and dy are added to x and y, but this cannot be done for th. In order to change the value back to zero after a complete rotation, the code first adds the values of th and dth and then divides the remainder by 2π, the remainder being the new stored value of th, the rotation about the z-axis. To determine the velocity of displacement (vx,vy) along the x and y coordinate axes of the environment and the angular velocity of rotation (vth) about the z axis, the derivatives of the values defined above with respect to dt are determined:

$$vx = \frac{dx}{dt} \tag{13}$$

$$vy = \frac{dy}{dt} \tag{14}$$

$$vth = \frac{dth}{dt} \tag{15}$$

where:
vx – x-axis velocity of the structure in the environmental coordinate system
vy – y-axis velocity of the structure in the environmental coordinate system
vth – angular velocity of rotation of the structure about the z-axis
dt – the time interval

In the next step, the value of th must be converted to quaternions to make the value match the format of the message to be published. (Quaternions are an extension of complex numbers to 4 dimensions, allowing the code to process rotations around multiple axes at once.) In the next step, the variable "odom", which will contain the "pose" and "twist" messages associated with the odometry, will be declared and timestamped.

The "pose" message part will be set to the x and y coordinates and th, the "twist" message part will be set to vx,vy,vth. The content of the variable is then published to the 'odom' topic.

Finally, the stored right and left wheel step values are updated. (Gregor Klancar, 2017)

3. Results and discussion

As the current results of the project, with the finished code the vehicle is capable of functioning as a compatible element of the ROS2 framework, which is often used in the industry as well. Thanks to the different design processes, the vehicle is capable of executing tasks from software, physically with acceptable precision. Beside this as an autonomous navigational function, the vehicle can also describe its location with the help of the odometry code.

The current form of the robot can be seen below on figure 2.:

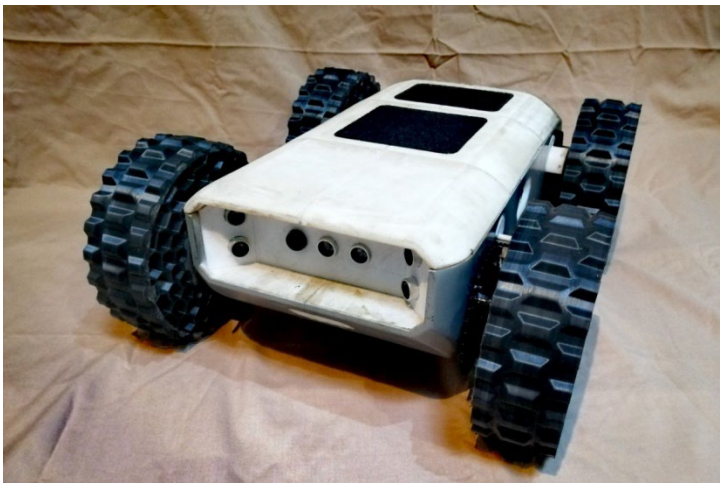

Figure 2. The robot's current form.

Conclusions

The project's goal was to create a developmental platform, that could be capable of doing basic autonomous navigational tasks.

For this to succeed, first a virtual 3D model of the needed components had to be designed, in a way that's later become close representation of reality. FDM 3D printing technology was utilized to manufacture the modelled parts, this made it possible to quickly test, redesign and reprint the components for them to be more precise with every iteration. In order to make it possible for some parts to print successfully, the printer had to be modified and calibrated several times. As the electrical design proceeded to make it possible for the vehicle to function properly, attention was also paid to make room for future upgrades. One of the more, if not the most challenging aspect of the project was the programming process, which goal was to make it so on a reasonable level.

For future development maybe the actual usage of the equipped ultrasonic sensors is the most relevant. To use them only the programming needs to be done, and by that point the vehicle could be capable of doing some fully fledged self-driving. Furthermore, it could be equipped with a lidar which would further increase its capabilities. It would be also reasonable to improve on the precision of the rotary encoders, which could be done by a low-pass filter, or to increase the capabilities of the position determination system by the integration of a GPS, gyroscope, or compass module. Beside these, the modular design of the vehicle gives an open opportunity for additional sensors or manipulators to be equipped, for example instead of the ultrasonic sensors there could be cameras as their usage is supported by the compatibility with the ROS2 framework.

References

[1] CENTERS, E. 3. (2017). 3D PRINTING TECHNICAL GUIDE.

[2] DUDEK, P. (2013). FDM 3D PRINTING TECHNOLOGY IN MANUFACTURING COMPOSITE ELEMENTS. *A R C H I V E S O F M E T A L L U R G Y A N D M A T E R I A L S, 58*(4).

[3] Dulika Nayanasiri, a. Y. (2022. Maj 26). Step-Down DC–DC Converters: An Overview and Outlook. *MDPI: electronics*.

[4] Endre Erős, M. D. (2019. June 24-28). A ROS2 based communication architecture for control in. *ScienceDirect*.

[5] Gregor Klancar, A. Z. (2017). *Wheeled Mobile Robotics: From Fundamentals Towards Autonomous Systems.* Elsevier Science.

[6] Jenkin, G. D. (2010). *Computational Principles of Mobile Robotics.* Cambbridge, USA: CAMBRIDGE UNIVERSITY PRESS.

[7] Majumdar, S. K. (2014). Kinematics, Localization and Control of Differential Drive. *Global Journal of Researches in Engineering: H Robotics & Nano-Tech*, 9.

[8] Nourbakhsh, R. S. (2004). *Introduction to Autonomous Mobile Robots.* Cambridge, Massachusetts és London, UK: Massachusetts Institute of Technology.

Effect of air collector structure on the efficiency of a solar dryer

QuanKun ZHU[1], János BUZÁS[2], István FARKAS[2]
[1]Doctoral School of Mechanical Engineering,
[2]Institute of Technology,
Hungarian University of Agriculture and Life Sciences

Abstract

In this paper, an indirect solar dryer discussed, which was constructed in the Solar energy laboratory of the Hungarian University of Agriculture and Life Sciences. The main core components are the collector and drying chamber. The purpose of this paper is to study the effect of horizontal fin collector and inclined fin collector on a solar drying system. The experimental results show that the horizontal fin collector has better ability to absorb and convert solar radiation energy, better dehumidification capacity, and the average efficiency is higher than that of the inclined fin collector. The solar drying systems with horizontal fin collectors have better thermal performance.

Keywords

efficiency, finned absorber, solar collector, solar drying system

1. Introduction

Solar drying system is a device that uses solar energy. Because of its economical, energy-saving, and environmental protection features, it is often used for drying crops and fruits. The principle is to absorb solar energy and convert it into heat to remove excess moisture from the product. The process involves heat and mass transfer operations. The efficiency of solar drying is affected by factors such as temperature, humidity, solar radiation and wind speed.

Farkas and Géczy-Víg (2003) analysed the thermal network model and the Hottel-Vhillier (H-V) model of flat-plate solar collectors by using artificial intelligence methods. The research results showed that the ANN structure of the three collectors for air, water and latent heat storage can be successfully trained using the data of the H-V model, and the outlet temperature distribution can be accurately described using ANN, with an average deviation of 0.9 °C.

Sopian *et al*. (2009) established a theoretical model and verified it experimentally to analyse the thermal efficiency of porous and non-porous dual-pass solar collectors. The research results show that the introduction of porous media in the second channel of the double-return collector can increase the heat

transfer area and increase the outlet temperature. Thereby improving the thermal performance of the whole system, the thermal efficiency is about 60-70%.
Montero *et al.* (2010) designed and built a solar drying system to study the thermodynamic behaviour of Spanish high-moisture crops under different operating modes. The results of the study showed that dryers in passive mixed mode performed better under no-load conditions. Under load, for the collector, the temperature increases by 15 °C for the passive mode system and 4 °C for the active mode. For the drying chamber, the maximum temperature difference between the inlet and outlet is 17 °C and the maximum humidity difference is 27% in the forced hybrid mode. In drying experiments with dried olive pomace, the hybrid and mixed modes of operation performed best, cutting the drying time in half.

Şevik (2013) designed and built a new type of solar dryer using double-pass solar air collector (DPSAC), and tested its performance by drying carrots. According to test results, drying carrot slices to a constant weight (weight variation less than 0.1 g water/g dry matter) required 220 minutes. The air velocity has an impact on the collector's efficiency, and the DPSAC's thermal efficiency ranges from 60% to 78%. DPSACs are effective in a variety of thermal applications.

Bhowmik and Amin (2017) built a flat plate collector with or without reflector and designed a comparative test in Bangladesh in January 2015. For improve collector reflectivity a combination of solar reflector and collector were used. The research results have been shown that solar radiation greatly affects the efficiency of collector, and the combined use of reflector and collector is about 10% more efficient than the collector in itself, and reflector can improve the efficiency of flat-plate solar collector.

Verma *et al.* (2020) developed a collector with spiral shaped fluid passage tube for thermal behaviour comparison with traditional flat plate collectors. The research results show that under the forced mode, under the same mass flow and solar radiation conditions, the thermal efficiency of the spiral tubed collector increases by 21.45%, and the exergy efficiency increases by 6.73%. The collector tubed with helical-shaped tube uses less material and costs less to produce and maintain.

The solar collector is the core part of the entire drying system and has a significant impact on the efficiency of the system. The purpose of this paper is to study the effect of different solar collector components on the whole drying system.

2. Experimental

The experimental set up
The horizontal finned and 45° inclined finned double pass solar air collector experiment was carried out at Solar energy laboratory of the Hungarian University of Agriculture and Life Sciences, Gödöllő, Hungary (47.59º N, 19.36º E). The experiment was conducted from 10:00 am to 3:00 pm in October 2017, the

weather was clear, ambient temperature and solar radiation was constant. The experimental data was collected every 10 minutes during the experiment period. Air speed was 2.3 m/s in the solar system by using the inline air blower.

The two solar collectors have the same absorber surface area, the difference is the fin direction, see Fig. 1. The absorber function is to collect solar energy from the sun, the fin function is to increase the absorber surface. The sides and back side of collectors made from wood, with the dimension 120 cm × 50 cm × 12 cm. The ambient temperature, the inlet, outlet, and absorber temperature of the collectors and drying chamber temperature furthermore relative air humidity of drying chamber have been measured (Al-Neama and Farkas, 2017; 2019).

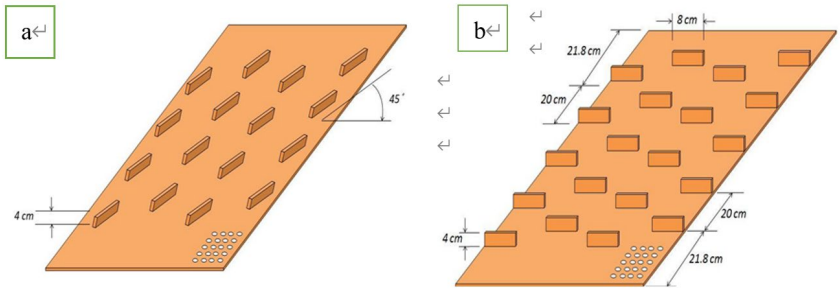

Figure 1. Collector structures: a) Incline 45° finned absorbing surfaces; b) and horizontal finned absorbing surfaces

Main components of solar drying system

Figure 2. The layout of the solar dryer system (Al-Neama, 2017; 2019)

In this experiment, the major components of the solar drying system are a solar thermal collector, a drying chamber, and a chimney, see Fig. 2. The function of the collector is to absorb the energy of solar radiation, the function of the drying chamber is to place the items to be dried, and the function of the chimney is to accelerate the flow of air. An in-line blower, a power controller, and an air duct are utilized as accessories. Thermocouples and thermometers, relative humidity meters, pyranometer, anemometers use to measure relevant parameters.

3. Results and discussion

Temperature distribution of solar collectors

In the experiment, related instruments were used to measure the inlet and outlet temperatures of the horizontal fins and 45° inclined fins of the double air pass solar collector. Fig. 3 shows that the temperature of horizontal fin collector is consistently higher than the incline 45° fin collector. The variation trend of the input temperature of the two collectors is similar. The upper channel temperature is consistently higher than the lower channel, the maximum temperature difference is around 15°. The output temperature trend of the two collectors is the same, rises slowly to a maximum value and then drops.

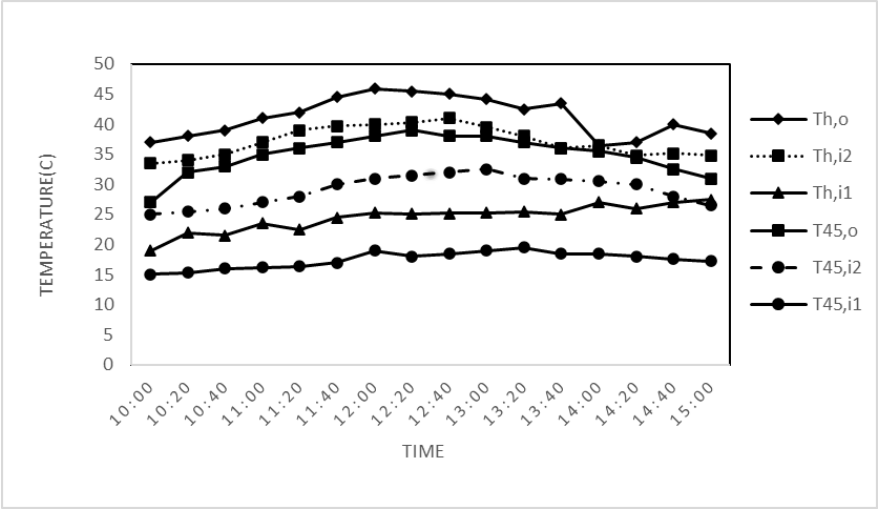

Figure 3. The temperature distribution of two solar collectors

The average absorber plate and ambient temperature

Fig. 4 shows the ambient and absorber surface temperatures of two collectors. For horizontal fin collector, the average absorber surface temperature rises gradually over time, reaches a peak and then starts to fall. At 12:20, the temperature reaches the maximum value of 50 °C. The ambient temperature rises slowly over time.

For incline 45° fin collector, the temperature trend of average absorber surface is similar to horizontal fin collector. At 12:40, the temperature reaching the maximum value of 58 °C. After 12:00, the ambient temperature barely changes at all. In the experiment, the average absorber surface temperature of incline 45° fin collector is always higher than that of horizontal fin collector, it is indicating that the amount of solar radiation absorbed is large.

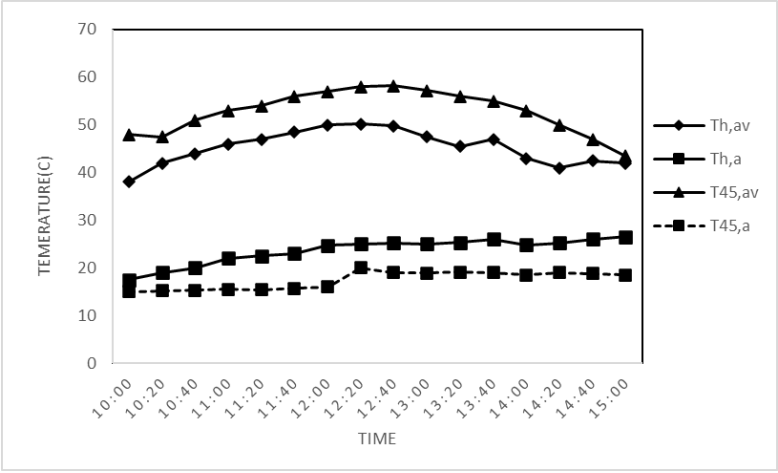

Figure 4. The average absorber surface and ambient temperature

Useful heat analysis of solar collectors

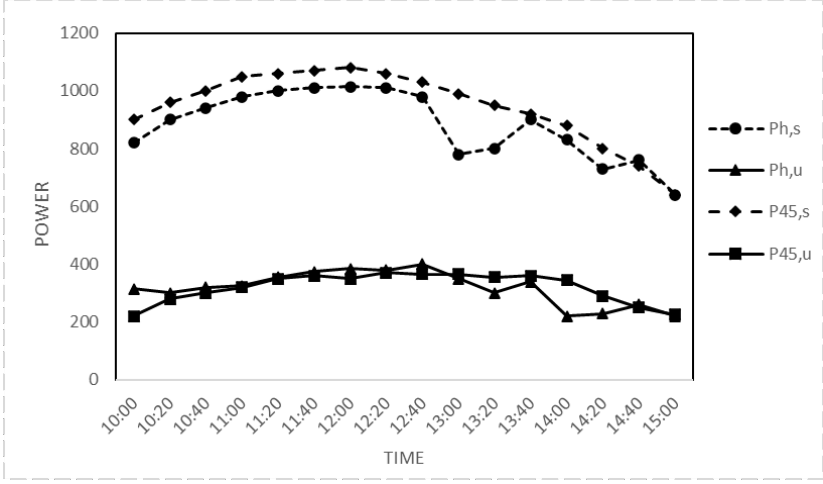

Figure 5. Global solar radiation in the collector plane and the useful heat gain of horizontal finned and 45° inclined finned air collectors

Fig. 5 shows the solar radiation and the energy absorbed by the two collectors. For horizontal fin collector, solar radiation increases over time, reaches a maximum value of 1015 W/m^2 at 12:00. Between 12:40 and 13:40, the solar radiation changes abruptly due to clouds. For inclined fin collector, solar radiation increases with time, after reaches a peak value of 1080 W/m^2 at 12:00, gradually starts to decline. In the experimental, the solar radiation of incline fin collector is higher than horizontal fin collector. The useful heat values of the two collectors are quite close to each other. It shows that the horizontal finned collector has a strong ability to absorb and convert solar radiation.

The efficiency of collectors

Fig. 6 shows the efficiency of the collectors. For horizontal fin collector, the efficiency curve fluctuates greatly. Between10:20 and 13:00, the efficiency increases over time and reaching a maximum efficiency of 70% at 13:00. At 14:00 the efficiency is the lowest, 40%. For inclined fin collector, the overall efficiency curve shows an upward trend. At the begin, the efficiency value is the lowest 40%. At 13:40, the efficiency reaches the maximum value around 60%. After 13:00, the efficiency curve does not fluctuate much. The graph shows average efficiency of horizontal fin collector is higher than that of inclined fin collector.

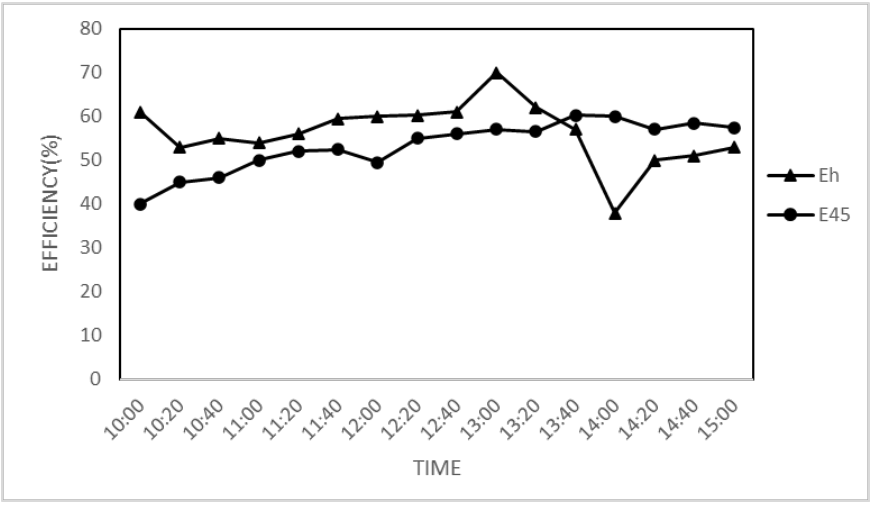

Figure 6. The efficiency of two collectors

Drying chamber temperature analysis

Fig. 7 shows the ambient and average temperature of drying chamber over time. For horizontal fin collector, the average temperature of drying chamber does not change much, the temperature difference is 5 degrees, maximum value is around 28 °C. The maximum ambient temperature is around 20 °C. For incline fin collector, the overall trend of ambient temperature is rising, reaching the

maximum value around 27 °C at the end of experiment. The curve of the average temperature changes greatly, and the maximum temperature difference is about 10 degrees. At 12:20, the temperature reaches the maximum value of 37 °C. The graph shows a positive correlation between the ambient temperature and the average temperature in drying chamber.

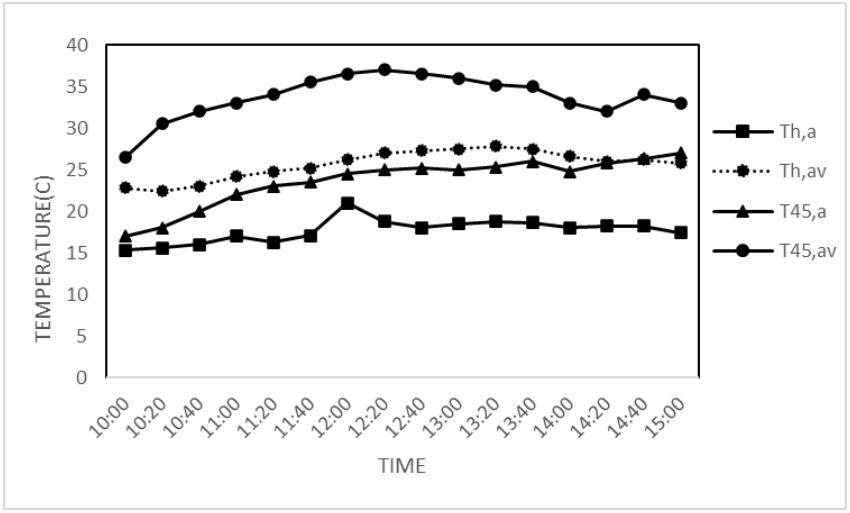

Figure 7. The drying chamber temperature

Drying chamber humidity analysis

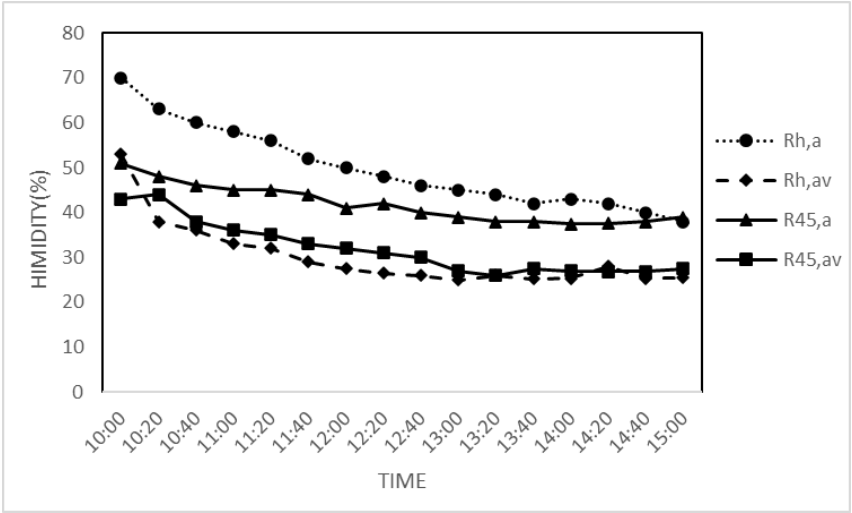

Figure 8. The humidity of drying chamber

Fig. 8 shows the ambient humidity and average humidity of drying chamber over time. For horizontal fin collector, the ambient humidity is 70% at the beginning, it is gradually dropped during the experiment. The final humidity is 38%, a total drop of 32%. The average humidity of drying chamber dropped rapidly between 10:00 and 12:40, and the humidity changed little thereafter. In the experiment, the average humidity has dropped by about 28%. For incline fin collector, the ambient humidity drops slowly over time, with a total decrease of 12% during the experiment period. At the end, the humidity is 39%. The general trend of the average humidity curve is similar to the ambient humidity. During the experiment, the humidity dropped by about 15%. At the end, the average humidity is 28%. The graph shows the changes of the ambient humidity and the average humidity curve of the drying chamber of the two collectors are consistent. The ambient humidity and average humidity of the drying chamber of the horizontal finned collector dropped rapidly, indicating that the horizontal fin collector has a strong drying ability.

Conclusions

- Construct a solar drying system, equipped with horizontal fin collector and inclined 45° fin collector, and conduct drying experiments to study its drying performance.
- The temperature of the upper channel of the double pass air collector is higher than that of the lower channel in the experiment. The horizontal fin collector has a better ability to absorb and convert solar radiation energy. The average efficiency of horizontal fin collector is higher than inclined fin collector.
- For drying chamber, the average temperature is related to the ambient temperature. The horizontal fin collector has better ability to remove humidity.
- The experiment shows that the changes in collector absorber plates can have an impact on the performance of solar drying systems.

Acknowledgements

This work was supported by the Stipendium Hungaricum Programme and by the Doctoral School of Mechanical Engineering, Hungarian University of Agriculture and Life Sciences, Gödöllő, Hungary.

References

[1] Al-Neama M.A. and I. Farkas (2017), Investigation of finned solar air collector performance for drying purposes, R&D in Mechanical Engineering Letters, Gödöllő, Hungary, 16, 64-72. https://www.gek.szie.hu/system/files/oldal/mel_2017_16synergy.pdf

[2] Al-Neama M.A. and I. Farkas (2019), Thermal efficiency of vertical and horizontal-finned solar collector integrated with forced air circulation dryer for apple as a sample, Drying Technology, 37(5), pp. 546-558. doi: https://doi.org/10.1080/07373937.2018.1488260

[3] Bhowmik H. and R. Amin (2017), Efficiency improvement of flat plate solar collector using reflector, Energy Reports, 3, 119-123. doi: https://doi.org/10.1016/j.egyr.2017.08.002

[4] Farkas I. and P. Géczy-Víg (2003), Neural network modelling of flat-plate solar collectors, Computers and Electronics in Agriculture, 40(1-3), 87-102. doi: https://doi.org/10.1016/S0168-1699(03)00013-9

[5] Montero I., J. Blanco, T. Miranda, S. Rojas and A.R. Celma (2010), Design, construction and performance testing of a solar dryer for agroindustrial by-products, Energy Conversion and Management, 51(7), 1510-1521. doi: https://doi.org/10.1016/j.enconman.2010.02.009

[6] Şevik S. (2013), Design, experimental investigation and analysis of a solar drying system, Energy Conversion and Management, 68, 227-234. doi: https://doi.org/10.1016/j.enconman.2013.01.013, 2019

[7] Sopian K., M.A. Alghoul, E.M. Alfegi, M.Y. Sulaiman and E.A. Musa (2009), Evaluation of thermal efficiency of double-pass solar collector with porous–nonporous media, Renewable Energy, 34(3), 640-645. doi: https://doi.org/10.1016/j.renene.2008.05.027

[8] Verma S.K., K. Sharma, N.K. Gupta, P. Soni, and N. Upadhyay (2020), Performance comparison of innovative spiral shaped solar collector design with conventional flat plate solar collector, Energy, 194, 116853. doi: https://doi.org/10.1016/j.energy.2019.116853

Mechanical seal experiments in different tribometers

Marcell Péter KISS[1,2,3], Gábor KALÁCSKA[2,3]
[1]Flowserve Hungary Services Kft., Budapest
[2]Department of Materials Science and Engineering Processes,
Institute of Technology,
MATE Gödöllő
[3]Doctoral School of Mechanical Engineering,
MATE, Gödöllő

Abstract

Mechanical seals are under continuous development, with better solutions, material combinations and lubricants being investigated for a wide range of extreme operating conditions. To simulate real-life industrial operating environments tribometers are used to test the tribological properties of slip rings. Experiments have measured frictional torque, coefficient of friction, and the surface area and extent of wear on slip rings. Conclusions were drawn after the experiments. This article describes the measurement systems used, the tests carried out on them, and the results obtained.

Keywords

mechanical seal, wear, friction of coefficient, lubricants, tribometer, coating

1. Introduction

Measuring systems are used to test and determine the tribological properties of mechanical seals. On these test benches, the main goal is to create conditions that simulate the stresses and strains of mechanical seals in real operation. To achieve this, the different parameters need to be set on our measuring system. Examples of such settings are the load on the slip rings, the speed of the drive, the quantity and quality of the lubricants and the duration of the measurements. Several measurements can be carried out with different material combinations such as carbon, ceramic, silicon carbide and tungsten carbide, lubricants, slip rings with different surface qualities, materials manufactured and machined with newer production technologies and different composites. Different forces and torques are measured, such as friction torque. At the end of the measurement, the composition of the wear surfaces is examined under an electron microscope and the amount of worn material determined. These series of measurements help to identify and find new solutions, applications, manufacturing processes, coatings and substitute lubricants in the sealing technology. (KISS P. M., et al. 2022)

2. Silicon carbide under different lubrication conditions

In agriculture, water and other fluids in irrigation systems are transported by pumps, where it is essential to have a proper mechanical seal and to reduce wear and tear to a minimum to ensure long and efficient operation. Silicon carbide is one of the most popular materials used in these seals because of its high wear resistance and resistance to corrosive materials. Also, there are many coating solutions for silicon carbide seal faces, to increase heat resistance. (ZHANG, Sainan, et al., 2022)

In this study, Xingyu ZHAO and Ying LIU investigated the frictional performance of silicon Carbide and graphite-containing silicon carbide in dry and water lubricated cases. The tribometer was a Falex-1506, on which could vary the load applied to the slip rings at constant speed. During the measurement, a torque sensor was used to measure the actual friction torque.

Sintered silicon carbide mechanical seal rings were used for the measurement. Figure 1 shows the sequence of clay pairings made during the measurements.

Pair conditions	No.	Friction pairs
Self-mated pair	1	WNV2/WNV2
	2	CHV1/CHV1
	3	R/R
	4	R2/R2
Nonself-mated pair	5	WNV2/CHV1
	6	WNV2/R2
	7	CHV1/R2
	8	R/R2

Figure 1. Material combinations used in measurement.

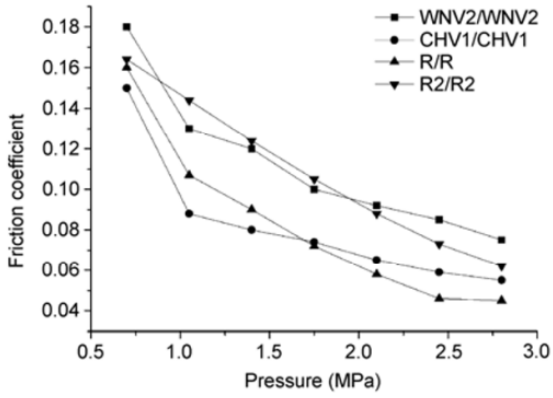

Figure 2. Variation of friction coefficient for identical material combinations under water lubrication.

The measurement was made on a Falex-1506 type tribometer with the ring fixed on top was rotating and the lower ring remained stationary. For distilled water lubrication, the load range was from 0.7 MPa to 2.8 MPa at a circumferential speed of 5.074 m/s. For dry lubrication, the load was varied from 0.31 MPa to 0.69 MPa at a lower circumferential speed of 0.665 m/s. All measurements were performed for 10 minutes.

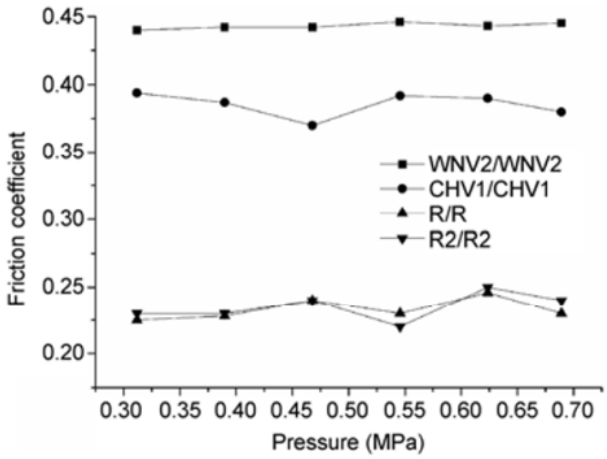

Figure 3. Variation of friction coefficient for identical material combinations under dry lubrication.

Figure 2 clearly shows that the coefficient of friction between the slip rings is reduced from 0.18 to 0.05. At the beginning of the measurement, dry lubrication was present, and then as time passed and the load increased, the dry lubrication changed to wet lubrication. This is due to the fact that the holes in the friction surface of the material pairs became larger due to wear, allowing more fluid to be absorbed by the higher pressure.

As pressure increases, the percentage of water lubrication increases, which means a reduction in the friction coefficient. This behavior is also true and noticeable for different material combinations. Figure 3 clearly shows that for dry lubrication, the coefficient of friction increases minimally with increasing load. The same is observed for different material pairings. In agricultural and industrial pumping technology, equipment is often used to transport drinking water, irrigation water, water and a mixture of other chemicals. In these pumps, it is very important to use slip ring seals that provide adequate sealing during operation. The study by Xingyu ZHAO and Ying LIU makes a major contribution to the long-lasting and reliable operation of these material combinations in sliding ring seals for liquid transfer equipment in agriculture and industry. (ZHAO, Xingyu, et al. 2014)

3. Frictional characteristics of laser-texture seal face

One possible solution to increase the lifetime of mechanical seals is to minimize wear during operation. With laser surface machining, porous wear surfaces can have a lower coefficient of friction than surfaces machined by other manufacturing techniques. (WANG, Tao, et al. 2014) In this study, X.Q. Yu and S. He investigated two laser-textured sliding rings and their wear properties by varying the speed and load.

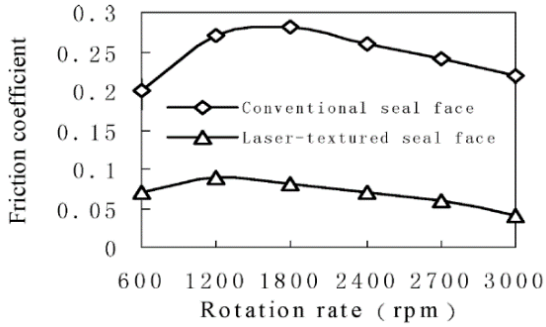

Figure 4. Change of friction coefficient at 68 N load.

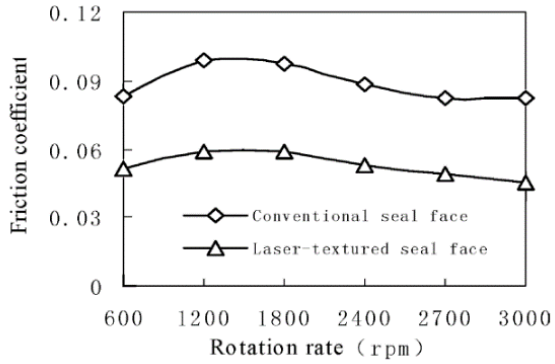

Figure 5. Change of friction coefficient at 136 N load.

X.Q. Yu and S. He used silicon carbide and carbon slip rings in their investigations. These two materials are very widely used in today's pumping technology because of their wear resistance, high hardness, and corrosion resistance. The silicon carbide was the stationary ring, while the carbon slip ring was on the bench. The contact surfaces were polished and only the wear surface of the silicon carbide sliding ring was machined by laser. When laser machining, the frequency with which spherical pores form in the surface can be adjusted.

After polishing, the average diameter of a pore was 90 μm and their frequency on the surface was 20%. Before each measurement, the silicon carbide slip ring was cleaned with acetone. The measuring bench consisted of the following units: frequency converter, electric motor, rotating slip ring, stationary slip ring, torque measuring device, lubrication system and load. During the measurement, mineral oil was used as a lubricant, which was supplied by the lubrication system from a reservoir. At the beginning of each measurement, an initial measurement of 900 s at 1200 rpm was carried out. The speed was then increased by 600 rpm from 600 rpm to 3000 rpm. Each step was measured for 300 s, where the temperature and friction torque between the slip rings were monitored every 30 s. For each measurement, the slip rings were subjected to a different load. For the first measurement, the load was 34 N, and then the load was increased by 34 N up to 170 N. The same pair of slip rings was used for all measurements. In Figures 4 and 5, it can be clearly seen that as the load increases, the coefficient of friction also increases. The two coefficients of friction are very different from each other, which is mainly since the contact surface of one slip ring has been laser-textured while the other ring has not. During laser machining, the micro-pores formed on the surface are better able to retain the lubricant, thus acting as a micro-sized lubricant bearing. This property results in better lubrication, which in turn leads to less friction.

This preliminary result can be a good starting point for seals used in industry and agriculture. (YU, X. et al. 2002)

4. Dry, compressed air, liquid lubricating conditions

Of course, many other media can be considered as lubricants in the process, not just mineral and vegetable oils. S. Kavinprasad and S. Shankar have carried out measurements on both dry and compressed air lubrication. Their primary objective was to measure the temperature generated during friction, as this has a major influence on the lifetime of sliding ring seals. The slip rings were made of carbon and SS 316. These materials are widely used in sealing technology because of their properties such as high wear resistance, heat shock resistance and high hardness. In addition to dry and compressed air, Neem oil and water have also been used as lubricating and cooling fluids.

The measuring bench for the measurements consisted of the following units: pump, DAQ, LAB view, RPS, inverter, load, electric motor, sealing chamber, thermocouple, and wind gauge. The slip rings tested were made of SS 316 high speed steel and carbon. The speeds used in the measurements were set and checked by means of the friction converter. The flow control valve and pressure adjustment valve of the cooling system were monitored and controlled by LAB view. The DAQ system allowed the measurement of inlet and outlet temperatures using the thermocouple. The air velocity was monitored by the anemometer. The pressure in the dust seal, the size of the wear surfaces and the sliding speed have a great influence on the friction between the sliding rings.

In addition to the measurements, a computer finite element model was also created using ANSYS ICEM CFD14.0. A thin layer is placed between the two slip rings to simulate the location of heat evolution in the system. Various boundary conditions such as velocity, pressure and slip rings are defined to reproduce the real model when using the program.

Each measurement took five minutes. The speed of the electric motor was varied from 200 rpm to 1200 rpm during the measurements, while the load was varied to 58 N, 67 N and 76 N. In these measurements, compressed air, water, and Neem oil were used as lubricants. The CFD simulation simulated perfect lubrication and minimal heat generation in case of Neem oil lubrication. For compressed air and water at a flow rate of 3.2 m/s, the simulation showed similar results as the real measurements. On the test bench, for compressed air and water, the result is that the heat generated during the five-minute measurement was 66 °C. As soon as the velocity of the compressed air inlet was increased to 3.2 m/s, the temperature generated dropped to 51 °C. For liquids the temperature is lower than in the previous case. At maximum speed and load, the highest temperature measured with Neem oil lubrication was 38°C while in the water lubricated system it was 41 °C. From the results of the measurements, it is clear that maximum heat developed when PV (pressure and velocity) values are high. For this reason, these applications prefer to operate at lower pressures and lower speeds with adequate lubrication. The heat development is considered as a loss, which can be deducted from the electrical motor performance.

The measurement clearly demonstrates that Neem oil can be a suitable coolant between SS 316 and carbon slip rings at higher speeds and loads. The right lubricant should be selected for different material pairings as this will greatly increase the life of the seals. If it is not possible to use Neem oil, compressed air and water may also be a suitable solution. (KAVINPRASAD, S. et al. 2013)

5. Steam environment

At higher temperatures and pressures, vapor pressure may be present in the pumps in addition to the medium being pumped. For steam environment the most common used material is carbon. (ZANINI Peter, 2017). The following study sliding ring seals were investigated in a steam environment. S.S. Goilkar and Harish Hirani investigated the wear and tribological changes on sliding ring seals under steam pressure in a real operating environment. The measurement system was designed and set up to simulate a real industrial application.

In this study, the system was sealed using a slip ring seal with steam flowing through it. The seal is subjected to enormous pressure from the working fluid, as there is steam inside the system and only atmospheric pressure outside. During operation, the steam tries to escape from the system between the two pairs of sliding ring seals and thus tries to separate the ring pairs. To prevent this, a kicker is used to keep the seals under constant axial load.

The bench assembled for the measurement consisted of the following units: electric motor, frequency converter, pressure sensor, temperature and speed indicator, steam output, thermocouple, rotary joint, target plate, rotary joint and drainage outlet. During the measurement, the temperature was 110-160 °C, the maximum pressure was 5 kgf/cm2(9.81*N/ cm2), the maximum speed was 240 rpm, and the working fluid was dry saturated steam. The measurement lasted 24 hours, which simulated the real operating conditions of the dryer drum. In order to achieve a simulation of the real steam environment, a separate steam inlet module consisting of a moisture separator and a pressure control valve is designed. This system continuously monitored and controlled the parameters during the measurements. To check the condition of the shaft, a measuring clock was used and to monitor the torque variation during the measurement, a disc was concentrically mounted on the shaft, where an optical displacement sensor detected and measured the displacement between the sensor and the disc shroud. The slip ring seal used for this measurement consists of four parts. Of the four parts, only the third is made of carbon graphite, while the other three are made of antimony-impregnated carbon graphite.

The total load from the operating pressure is ultimately applied equally to the seal and the shaft. The high pressure causes the steam to try to escape through smaller gaps into the lower pressure space. Such small gaps are found, for example, at the interface between the shaft and the seal, where the vapor tries to separate the shaft and the seal housing. This pressure controls the lubrication conditions at the mating surfaces.

The results show that the friction torque varies in direct proportion to the steam pressure. As the vapor pressure increases, the frictional torque increases, with the change in frictional torque being smaller for low balance ratios than for higher balance ratios. In previous studies it was claimed that at higher balance ratios the slip ring seal operates under more stable conditions, but here the failure of the third element was due to high vapor pressure. At higher balance ratios, the friction torque was measured to be between 5 and 30 Nm, as the thin layer of lubricating fluid between the friction surfaces could not be permanently formed, which would have greatly reduced the friction coefficient. At lower balance ratios, this fluid layer can form more easily. At any balance ratio, the vapor pressure increases the friction torque, which reduces the life of the mechanical seal. (GOILKAR, S. et al 2010)

6. Cryogenic environment

The following study will investigate the tribological properties of mechanical seal in cryogenic environments. For very cold liquids and gases, the most common material choices for slip ring seals are stainless steel and graphite. However, during operation these materials are subject to very high wear. In the following study, Jianlei Wang, Qian Jia et al. investigate how a slip ring gasket with a-C coating behaves in cryogenic environments.

Before starting the measurements, the sliding ring made of 9Cr18 stainless steel was cleaned with acetone and dried with dry air. Using a pulsed direct current device, an amorphous carbon coating was applied to the cleaned stainless slip ring. A titanium layer was then applied between the substrates to increase the adhesion strength.

The properties of the a-C coating were investigated on a stork-disc tribometer. Three different media were used, air, water and liquid nitrogen. The disc rotated at a speed of 10 1/second, with a 3 mm diameter ball of 9Cr18 material in contact from above. The load forces were 1, 4 and 8 N, and in each case the measurement lasted 30 minutes. A single X-ray photoelectron microscope (XPS, Axis Ultra) was used to evaluate the chemical composition of the wear marks. Figure 6 shows that the highest specific wear was measured when dry lubrication was used, while the lowest specific wear was measured when water lubrication was used. As the load increased, the wear rate also increased, but not in a straight proportion, as the increased degree of graphitization improves the lubrication conditions. When using liquid nitrogen, there are also wear marks on the disc, so in this case the conditions are similar to those for dry lubrication. The only difference is that oxidation during measurement has no effect on the coefficient of friction due to the low temperature provided by liquid nitrogen.

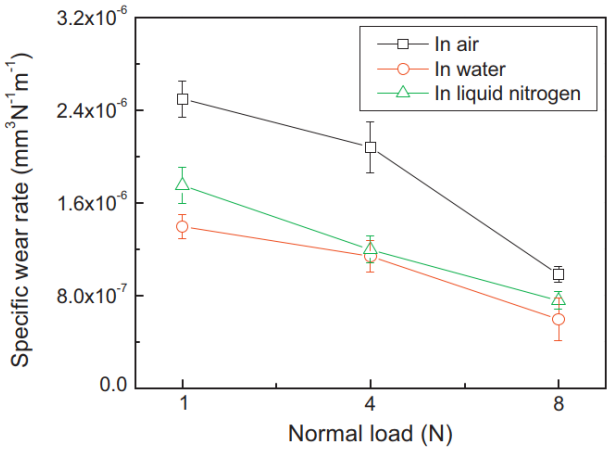

Figure 6. Specific wear of A-C coating with different lubricants.

Overall, the amorphous carbon coating greatly reduces the coefficient of friction in mechanical seals and can be a suitable solution even at extremely low operating temperatures. As mentioned earlier, the surface quality and hardness of the slip rings determine how wear resistant a given seal will be. In the following study, a new manufacturing process for carbon-based slip ring seals is investigated. (WANG, Jianlei, et al. 2012)

7. Tribological properties in case of new production process

In sealing technology, carbon-based materials are preferentially used because of their hardness, fatigue strength and heat shock resistance. However, at higher pressures and speeds, carbon-based slip ring seals require improvements in mechanical properties. The study by Zhanjun Liu et al. presents possible optimizations for carbon-based slip ring seals. In their investigations, the following raw materials were used: calcined coke, black carbon powder, coal tar pitch and organic solvent. Two different mixing methods were used in the research, one is the traditional solid mixing, and the other is the new liquid method. The new method was to melt the pitch in the solvent and add the coke and black carbon powder. The mixture was then dried at 100 °C for two hours to ensure that the solvent evaporated and calcined at 550 °C under 3 MPa pressure. After cooling, the material was again reduced to 105 µm granules and remixed with the dissolved pitch. Finally, the material was ground to 75 µm grains and the solvent was completely evaporated from the mixture. The materials prepared by both methods were cast into cylindrical bodies and pressurized at 150 MPa. Calcination was carried out at 1300 °C for 2 hours. The topography of the specimens was examined by electron microscopy and the porosity by a mercury porosimeter.

Mechanical properties of our materials

Materials	Density (g/cm^3)	Compressive strength (MPa)[a]	Scleroscopic hardness	Porosity (vol.%)	Median pore diameter (nm)
CM	1.45	118	69	22.5	5143.4
NM	1.50	210	84	19.3	712.8
CMC	3.14	445	92	0.20	–
NMC	2.87	552	102	0.24	–

[a] Parallel to the graphite layers.

Figure 7. Mechanical properties of new materials.

Figure 7 shows the mechanical properties of the new materials. The density and compressive strength of the two new materials (CMC and NMC) have doubled. The most important property in terms of abrasion resistance is hardness, which has also increased. In addition, the porosity has decreased by a percentage, indicating that there are fewer voids than before, which means that the material is denser and more wear resistant. Porosity can be both positive and negative for slip ring seals. It is positive if the porous material has gaps on its surface that can trap the lubricant, thus forming a tiny, tiny lubricant bearing hole in the gap and reducing the coefficient of friction. Overall, it can be concluded from the study that the mixing, compaction, and calcination of raw materials can greatly affect

the hardness, microstructure, and other mechanical properties of the materials. These materials could even play an important role in sliding ring seals. (LIU, Zhanjun, et al. 2007)

8. Multilayered diamond coatings

The different coatings on sliding ring seals can have a major influence on the degree of wear. (ADJEMOUT, Mohand et al. 2021) In this study, M. Shabani et al. applied multiple coatings to slip ring seals and investigated their tribological properties under biodiesel and pressurized water lubrication. Silicon nitride ceramic slip ring seals were coated with ten layers of diamond coating. The diamond coatings were deposited on the ceramic rings using a hot filament chemical vapor deposition technique, also known as Hot Filament Chemical Vapor Deposition. During the pumping of biodiesel, the seals are exposed to high temperatures. The assembled measuring system was tested with water for the first time. Two different layers were prepared on two ceramic rings. One ring was coated with ten layers of diamond, the other with a single layer of diamond. For both rings, the total coating thickness was 10 μm. A TE-92 Plint type tribometer with ring-to-ring coupling was used for the measurement.

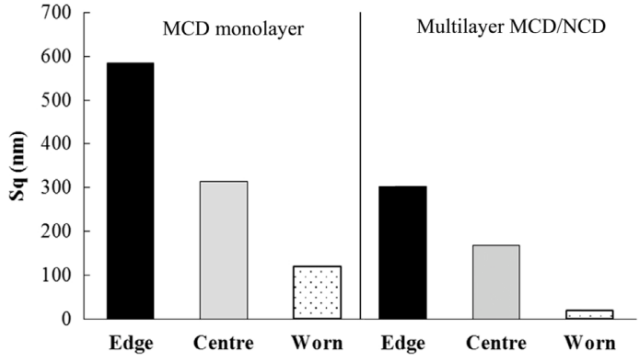

Figure 8. Surface roughness and wear rate.

The measurement was performed according to ASTM D3702. The smaller diameter ring performed the rotary motion, and the larger diameter ring was captured on the tribometer. The measurement was carried out with biodiesel and then in a system filled with water at 2 bar overpressures. The biodiesel contained 77% soybean oil, 22% palm oil and 1% rapeseed oil. The test runs started with an initial run lasting 2.5 hours to achieve proper lubrication under stable conditions. This was followed by 16 hours of measurements. The coefficient of friction was determined from the instantaneous torque using a load cell. The sealing was measured with pressurized water. The pressure was 2 bar. During the test the seals

provided a complete seal against the pressurized water. The stressed sealing surfaces were examined using a Hitachi SU-70 electron microscope. The microscope was used to characterize the surface morphology of the diamond coatings. Surface roughness, topographic analysis and wear volume were measured using a 3D optical profiler.

The single-layer coated specimen has coarse-grained pyramid-shaped diamond crystals in contrast to the multilayer nanocrystalline surface of the diamond-coated ceramic ring. After the electron microscope measurements, the surface roughness of the two different types of rings and the amount of wear during the biodiesel measurement are shown in Figure 8. The diagram clearly shows that the surface roughness of a ceramic gasket with a single coating is almost twice that of a ring with multiple coatings. Consequently, there is also a large difference in the amount of wear volume. In the case of gaskets, minimizing wear is of primary importance, along with adequate sealing. (SHABANI, M., et al. 2017)

9. Planned tools and methods

My research topic concerns the wear and testing of mechanical seals. I plan to carry out the experiments on a similar measuring system to the above test bench designs.

I will carry out the measurements and tests needed for my research on a new measuring bench. The measuring bench will consist of the following parts: a shaft, bearings, heating fiber, a thermocouple, pressure gauge, electric motor, a flexible coupling, an inverter (optional), a box with two spaces divided in the middle so that one side contains the medium (liquid or gas) and the other side contains only air.

In the center of the container is located the mechanical seal, where the material of the wear rings has been specified by the industrial partner. The material pairing will be the following: carbon filled PTFE vs carbon filled PTFE, I name this material pairing CP, and the other pairing is PTFE vs Aluminum-oxide which got the name PA. During my tests, I plan to measure the sealing performance, the wear rate of the friction surfaces and the chemical composition of the wear rings for different material pairs and media. The chosen media are Nitrogen in gaseous state vs air, and corrosive substance versus air. I plan to do the experiments with CP and PA material pairing for both type of medium. During the measurement, I will be able to vary the following parameters:

- the spring force compressing the sliding ring seals,
- gear ratio,
- electric motor speed using a frequency converter,
- temperature,
- pressure of the media.

Since mechanical seals have a lifetime of 2 years, the measurements must be taken over a longer period to show visible changes and wear on the contact

surfaces. It is of course possible to change the influencing conditions during the measurements to speed up the processes, for example by increasing the spring force or applying higher engine speed. Regardless of these conditions, I plan to carry out the measurements for the following durations: 1 week, 2 weeks, 4 weeks, and 8 weeks. During the measurements, I monitor the composition of the working fluid and air in the two isolated spaces by changing the pressure of the working fluid, thus testing the tightness of the seals. After each measurement, I examine the wear surface of the mechanical seals and their chemical composition by electron microscope and determine the extent of wear

Conclusion

- Silicon Carbide and graphite-containing silicon carbide are long-lasting and have reliable operation in sliding ring seals for liquid transfer equipment in agriculture and industry.
- Laser surface machining creates micro pores where these pores are better able to retain lubricant, thus acting as a micro-sized lubricant bearing.
- Neem oil can be a suitable coolant between SS 316 and carbon slip rings at higher speeds and loads. If it is not possible to use Neem oil, compressed air and water may also be a suitable solution.
- At higher balance ratios the thin layer of lubricating fluid between the friction surfaces can not be permanently formed, which could greatly reduce the friction of coefficient between the mating and primary ring. At lower balance ratios the layer of lubricant formed more easily between the sliding surfaces.
- The amorphous carbon coating on stainless steel and graphite greatly reduces the coefficient of friction in mechanical seals and can be a suitable solution even at extremely low operating temperatures.
- Mixing, compaction, and calcination of raw materials can greatly affect the hardness, microstructure, and other mechanical properties of the materials. These materials could even play an important role in sealing technology.
- Multiple coatings on sliding surfaces have better tribological properties than single coating. This is because multi-coated surfaces have a nanocrystalline structure, while single-coated surfaces have a coarse-grained, pyramid shape.

References

[1] ZHAO, Xingyu, et al. Frictional performance of silicon carbide under different lubrication conditions. Friction, 2014, 2. Jg., Nr. 1, S. 58-63.

[2] YU, X. Q.; HE, S.; CAI, R. L. Frictional characteristics of mechanical seals with a laser-textured seal face. Journal of Materials Processing Technology, 2002, 129.1-3: 463-466.
[3] KAVINPRASAD, S.; SHANKAR, S.; KARTHIC, M. Experimental and CFD investigations of mechanical seals under dry/compressed air/liquid lubricating conditions. Procedia Engineering, 2013, 64. Jg., S. 419-425.
[4] GOILKAR, S. S.; HIRANI, Harish. Parametric study on balance ratio of mechanical face seal in steam environment. Tribology international, 2010, 43.5-6: 1180-1185.
[5] WANG, Jianlei, et al. Experimental study on friction and wear behaviour of amorphous carbon coatings for mechanical seals in cryogenic environment. Applied Surface Science, 2012, 258.24: 9531-9535.
[6] LIU, Zhanjun, et al. Carbon seal materials with superior mechanical properties and fine-grained structure fabricated by a new process. Materials Letters, 2007, 61.8-9: 1816-1819.
[7] SHABANI, M., et al. Multilayered diamond mechanical seal rings under biodiesel lubrication and the full sealing conditions of pressurized water. Wear, 2017, 384: 178-184.
[8] WANG, Tao, et al. Experimental study of two-phase mechanical face seals with laser surface texturing. Tribology International, 2014, 72: 90-97.
[9] ADJEMOUT, Mohand; HUARD, Stéphane. Enhanced mechanical seals performance by surface texturing and diamond coating. Sealing Technology, 2021, 2021.11: 4-9.
[10] ZANINI, Peter. Steam leakage reduction with carbon rings. World Pumps, 2017, 2017.3: 32-33.
[11] ZHANG, Sainan, et al. Properties of super heat-resistant silicon carbide fibers with in situ BN coating. Journal of the European Ceramic Society, 2022, 42.14: 6404-6411.
[12] KISS P. M., KALÁCSKA G.: Trends in material selection for mechanical seals: A review Mechanical Engineering Letters, Volume 21 2022.

Autonomous off-road navigation

Dávid KÖRMÖCZI[1,2], Péter KISS[1]
[1]Department of Vehicle Technology, Institute of Technology, MATE, Gödöllő
[2]Doctoral School of Mechanical Engineering, MATE, Gödöllő

Abstract

Autonomous off-road vehicles are spreading rapidly in multiple application fields, including agricultural and military applications. While supposedly fully autonomous off-road vehicles do exist, there is no generally accepted standardization to determine exactly what requirements have to be met by the vehicle to be considered fully autonomous. In this review paper, a generally applicable definition for "fully autonomous" off-road vehicle is created based on the SAE standard for on-road vehicles. Based on this, 5 state of the art off-road vehicles were selected, of which the manufacturer claims to be fully autonomous. These vehicles autonomous capabilities were reviewed and assessed by the requirement list. It has been determined that by this definition, currently no commercially available vehicles can be considered fully autonomous.

Keywords

autonomous vehicle, off-road, mobility on terrain

1. Introduction

Autonomous off-road vehicles are becoming increasingly more important in every application field. The most important areas of application of autonomous off-road vehicles are agriculture, military technology and planetary rovers, but apart from those vehicles with different autonomy levels are also applied in many other fields, for example in forestry or mining industry. The reason for using autonomous vehicles vary by application field. In the agriculture, the main reasons include the cost of human labor, the increased precision requirements in state of the art agronomic technologies which can be not me by a human operator, and the demand to ensure the continuous work with as few downtime as possible. In military applications, the key factor is the protection of human life and physical safety due the lack of personal presence on site. In space exploration, autonomous vehicles are needed as a remote-control system would be inapplicable due to the physical distance between the vehicle and the control center. [4, 7]

Although autonomous off-road mobility is a constantly evolving field, both from perspective of application and R&D, there still are multiple unsolved problems even in state of the art vehicle navigation systems. With the current

technical level, the navigation of autonomous off-road vehicles is limited by both computational performance, software and sensor capabilities.

In the off-road mobility research project conducted by the MATE Department of Vehicle Technology a complex navigation system will be created for off-road vehicles. The system includes the mapping of the terrain using both sensors mounted on the land vehicle and drone-borne LIDAR scanning, recognition and classification of the obstacles, creation of a vehicle-specific mobility map, and calculation of an optimal route. The navigation system will be field tested on small scale with ClearPath UGV, and on real scale with RM Mission Master vehicles. The navigation algorithm takes into account the both the microscopic and macroscopic topography, the mechanical properties of the soil, and the characteristics of the vehicle.

2. Criteria for mobility on terrain

In scientific research concerning off-road vehicles (both conventional and autonomous) it is a frequently occurring question whether the vehicle can traverse an obstacle or not. To examine this problem, first a well-defined criteria list must be set. In most scientific papers about this topic, these criteria is not defined, and (presumably because it is deemed trivial) obstacle negotiation is used without any explanation. However, there are multiple questions that can be not answered without this well-defined criteria-list. For example, in off-road vehicle dynamics it is a frequently occurring situation that the vehicle can only traverse the obstacle with a given initial speed by (partially) expending its momentum, but it could not do so without an initial speed, i.e. starting the movement from a static position. Another common situation is that the vehicle can controllably descend on a steep slope, but the traction and/or the soils shear strength is not sufficient to slow down or stop the vehicle. In these cases, the vehicle can traverse the obstacle, but only within the given conditions. Without any need for completeness, these and similar situations make it impossible to unambiguously state whether a vehicle can traverse an obstacle, without previously determined criteria. The following criteria is defined for 4 wheeled vehicles. Most of the criterions are also valid for vehicles with tracks or more than 4 wheels, but certain phenomena (for example the stability) may be different in that case. It can be stated that the vehicle can traverse the obstacle only if, in all points of the path, the following are true:

- The traction is large enough that the vehicle, taking into account all resistances (rolling resistance, air resistance, gravity etc.) can maintain a steady speed (either by driving or breaking) and begin moving from a standing position.
- The vehicle is in contact with the terrain only through the wheels, i.e. the other parts (for example the axles or the chassis) do not collide with the ground.
- The lateral grip is large enough that the vehicle can stay on the set route.

- The stability of the vehicle is insured, i.e. the vertical projection of the center of mass is inside the rectangle defined by the wheels.
- All 4 wheels are in contact with the ground.
- The vibrations are not large enough to mechanically damage the vehicle (including the passengers and the cargo).

Whether these criteria are fulfilled depends on the properties of the terrain, the vehicle, and the characteristics of the soil-tire interaction. The most important parameters that influence the obstacle negotiation capability are:

- Mechanical properties of the soil:
  - load bearing capacity,
  - compactibility/sinkage,
  - shear strength.
- Vehicle dynamic parameters:
  - suspension characteristic,
  - engine and transmission/drivetrain,
  - construction and size of the tire.
- Characteristic dimensions of the vehicle:
  - coordinates of the center of mass,
  - external dimensions (length, width, height),
  - wheelbase and track width,
  - ground clearance,
  - approach, departure and break-over angles. [3, 5]

3. Autonomous off-road vehicles

Definition of "autonomous" off-road vehicles

Contrary to on-road vehicles, currently there are no official standards, definitions or requirements to determine whether or not an off-road vehicle can be considered autonomous. There is no system either to define the level of autonomy for partially autonomous off-road vehicles. For this reason, in any scientific work where we use the "autonomous" for off-road vehicles, the term must be explained individually. In the absence of any official standard, in this paper the on-road autonomy level system made by SAE (Society of Automotive Engineering) will be used. Naturally, the definitions used in that standard cannot be directly applied for off-road vehicles, some changes have to be made in regards of normal operational conditions, intended use of the vehicle, and skills of the driver to whom the capabilities of the autonomous vehicle control system are compared. The definition for the highest driving automation level is:

"The automated driving system (ADS) can operate the vehicle on-road anywhere within its region of the world and under all road conditions in which a conventional vehicle can be reasonably operated by a typically skilled human driver. This means, for example, that there are no design-based weather, time-of-

day, or geographical restrictions on where and when the ADS can operate the vehicle. However, there may be conditions not manageable by a driver in which the ADS would also be unable to complete a given trip (e.g., white-out snow storm, flooded roads, glare ice, etc.) until or unless the adverse conditions clear. At the onset of such unmanageable conditions the ADS would perform the DDT fallback to achieve a minimal risk condition (e.g., by pulling over to the side of the road and waiting for the conditions to change)." [8]

While this definition is only applicable to on-road vehicles according to the standard, after some minor changes (e.g. using "off-road" instead "on-road", or "terrain" instead "road" etc.) we can also apply the definition for off-road vehicles. It is important to point out, however, that this definition for autonomy of off-road vehicle is not a generally accepted standard, and thus must be – similarly to any other definition in this topic – individually clarified or referenced in every paper where the term is used. It should also be clarified that while an autonomous vehicle navigation system must have at least the same performance as an experienced human driver, this definition refers only to the movement of the vehicle itself. Additional tasks that are usually performed by the driver (for example attaching an implement to an agricultural tractor or operating a truck's tipper) are not taken into account.

On this basis, the requirements for an off-road vehicle to be autonomous are the following:

The autonomous vehicle must be able to operate without any interaction or supervision by a human driver (including a remote operator), in any expectable weather condition. The vehicle navigation system must be able to perform any task (including choosing an optimal route through or around obstacles) which could be performed by a driver who has extensive experience of driving a similar vehicle under comparable terrain conditions. In case the task cannot be performed (for example due to extreme weather conditions), the vehicle must be able to detect that and safely come to an emergency stop. The navigation system must be able to calculate an optimal route between any two points (the vehicles current position and the destination) within the operational area, without using any pre-set routes or waypoints. For this, the vehicle can use any available navigation equipment (including GNSS) but can only rely on them to the extent that in case of a connection error, the vehicle can safely come to an emergency stop using only its built-in sensory features.

Classification of terrains

From the perspective of navigation, different terrains cab be categorized based on two aspects: whether the properties of the terrain are known, and whether there are macroscopic (macro) obstacles on the terrain. The macro and micro-obstacles are distinguished by their size. The exact size limit above which an obstacle can be considered macroscopic is not a general value, as it must be selected taking into account the dimensions of the vehicle as well. In Table 1, the classification of terrains and some typical application fields are shown.

Table 1. Classification of terrains [4]

Terrain	Known	Partially known	Unknown
Terrain with macro obstacle	Forestry machines	Vehicles in a surface mine	Military vehicels
Terrain without macro obstacle	Tractor on agricultural field	Does not exist	

The terrain is known if the properties (including topography, and in some cases mechanical properties) are available even before the vehicle begins the operation on that specific terrain. The source for this can include a GIS database, drone-based terrain survey, or data collected by the sensors mounted on the same or any other vehicle during an earlier operation on the same location. In this case, it is assumed that the terrain is exactly the same as it was during the initial data collection. For a partially known terrain, data about the terrain properties is available from the same source as above. However, it is expected that the data is not up to date, as some properties have changed since the data collection. The reason for this can be, including but not limited to, an area where earthwork is underway, an intermittent river, or the effect of weather conditions. For an unknown terrain, there is no prior data available. In this case, the navigation can only be fulfilled based on the vehicles own sensors and computational capabilities.

An obstacle can be defined as any feature of the terrain that limits the movement of the vehicle, including artificial structures, steep topography, or water streams. While navigating on a terrain with obstacles, the navigation system must be able to compare the properties of the obstacle to the capabilities of the vehicle and choose the vehicles route after computing whether it is possible to go through the obstacle, or around it. On a terrain without obstacle, the movement of the vehicle is not limited by the terrain properties. A typical example to that is a flat agricultural field. On an unknown terrain, it must always be expected that there are obstacles that the vehicle cannot traverse. Thus, even though physically it could exist, from navigation perspective an unknown terrain should always be considered one with obstacles. [4]

Off-road vehicles with partial autonomous capabilities

Currently, there are no commercially available vehicles that meet the above listed requirements of autonomy. However, there are many vehicles (some of them marketed as fully autonomous by the manufacturer or distributor) which can be considered partially autonomous, as they meet some, but not all requirements of full autonomy.

The John Deere 8R agricultural tractor claims to be “fully autonomous” per the description made available by the manufacturer. The tractor is capable to traverse on an agricultural field and perform various agronomic processes automatically. However, if the vehicle detects any unexpected obstacle in its path, it automatically comes to an emergency stop, without assessing whether it would be

possible to go around the obstacle and continue the desired route. For this reason, by definition this vehicle cannot be considered fully autonomous.

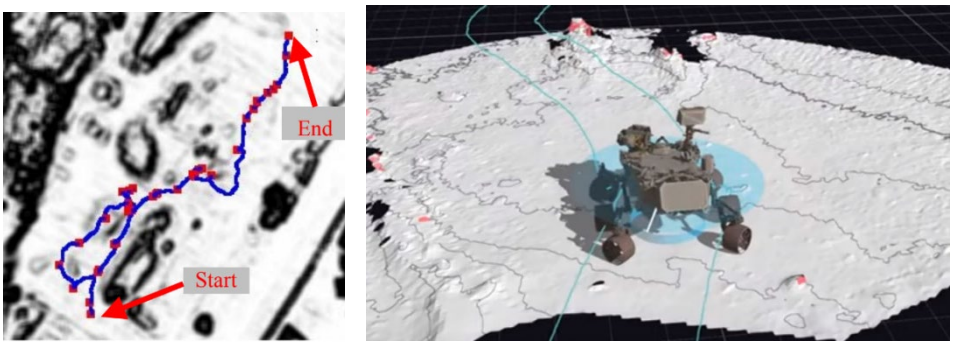

Figure 1. (a) Mobility map (b) 3D scanned terrain around the vehicle [7, 8]

One of the most advanced and well-known application of autonomous off-road navigation are the planetary rovers designed and built by NASA. The Perseverance martian rover utilizes the AutoNav navigation system, which is capable to acquire data about the microscopic environment of the vehicle in a radius of roughly 3-4 meters (Figure 1. b) and based on that, compute an optimal route an optimal route through or around obstacles. However, the navigation of the vehicle requires a set route previously chosen by a control crew. The autonomous capabilities can only be used to navigate around small obstacles in case the vehicle determines it is impossible to traverse through them, before following the original pre-set route. For this reason, this vehicle cannot be considered autonomous, as it requires human interaction to plan the route. It must also be pointed out, that the vehicle – compared to general vehicles used on Earth – has an extremely slow top speed (less than 0.1 km/h) and short sensing range (3-4 m), thus the computational capacity is not as important. By using a similar system under typical conditions of off-road vehicles, the required computational capacity would be 4 to 5 magnitudes larger at the very minimum, which could limit the navigation capabilities of the vehicle. [4, 6]

The vehicle Blitz, created in the PerceptOR mobility program of the US military, meets almost any requirement to be considered fully autonomous. While the vehicle has built in sensors which are used to gather data about the surroundings, but for the navigation it requires the assistance of a drone, which his equipped with sensors to obtain data about the 3-dimensional topography of the terrain, and which can be launched and landed on the vehicle. The system is able to create a mobility map (Figure 1. a) taking into account both the terrain and the properties of the vehicle, based on that compute a route to any given destination point, and traverse along that route. However, it can only be done under optimal circumstances, and the vehicle still requires continuous remote supervision by an operator. For this reason, even the designers refer to it as only

a partially autonomous vehicle. Furthermore, even this partial capability can only be achieved by complete navigation system, and not by a stand-alone vehicle. [4, 9]

Figure 2. (a) Case IH agricultural tractor (b) SMSS Unmanned military vehicle [1, 10]

The Case IH "Magnum" agricultural tractor, introduced in 2016, is not equipped with any cab or control devices required for operation by a human driver (Figure 2. a). The operator can only remotely interact with the autonomous control features. The tractor is equipped with every sensor needed to obtain detailed data about its surroundings, including LIDAR and radar, and is able to perform various tasks supposedly without interaction from the operator. However, similarly to the John Deer tractor assessed earlier, in case of an unexpected obstacle appears in the range of the vehicle, it automatically comes to a stop and waits for the decision of the operator. The tractors navigation system is capable to plan the optimal route both for travel and for some agronomical processes, between the previously set borders of the operational area. However, the vehicle can only travel to that area a route pre-set by the operator, without using its own navigation features. While the first prototype was finished for 2016 and since then many upgrades and enhanced versions were introduced by the manufacturer, the tractor is still not commercially available. [1, 4]

Conclusions

- A criteria list for obstacle negotiation for off-road vehicles have been made, and the most important terrain and vehicle properties that influence the obstacle negotiation capability have been determined.
- Based on the SAE standard for autonomous on-road vehicles, a new definition for autonomy of off-road vehicles has been created. In this definition, the requirements were listed for an off-road vehicle navigation system to be considered fully autonomous, the normal operational tasks

expected from the vehicle and the intended conditions have been specified.

- By applying this definition, from different application areas state of the art off road vehicles that are supposedly fully autonomous according to the manufacturer have been reviewed and assessed to determine if that statement is true. It has been found that by this definition, currently no commercially available off-road vehicle can be considered fully autonomous.

References

[1] Alberto-Rodriguez A. et al. (2020) Review of control on agricultural robot tractors. Int. J. Comb. Optim. Probl. Informatics 11.3: 9-20.

[2] Baladi G.Y. (1987) Terrain evaluation for off-road mobility, Journal of Terramechanics, Volume 24, Issue 2, pp. 127-140.

[3] Kiss P., Kiss B., Böröczky A. (2021) A terepi járműmozgást befolyásoló tényezők I. rész: Kerék–pálya kapcsolat, a terep tulajdonságai, Haditechnika 55 : 6 pp. 42-46.

[4] Körmöczi D., Kiss P. (2022) Autonóm Terepi Járműirányítás. Mezőgazdasági Technika 63 : 5 pp. 2-5. , 4 p.

[5] Laib L. (2002) Terepen mozgó járművek. Szaktudás kiadó, Budapest pp. 273-306

[6] NASA (2021) Self-Driving Perseverance Mars Rover 'Takes the Wheel' (https://www.nasa.gov, 2023.01.05)

[7] Priyanka K., Onkar S. (2022) Autonomous Tractors Market by Component (Sensor, GPS, Vision System, and Others), and Application (Tillage, Harvesting, Seed Sowing, and Others): Global Opportunity Analysis and Industry Forecast, 2021–2030

[8] SAE (2021) Standard J3016_202104: Taxonomy and Definitions for Terms Related to Driving Automation Systems for On-Road Motor Vehicles

[9] Stentz et al. (2018) Integrated Air/Ground Vehicle System for Semi-Autonomous Off-Road Navigation. Carnegie Mellon University.

[10] Xin L. et al. (2013) The latest status and development trends of military unmanned ground vehicles," 2013 Chinese Automation Congress, pp. 533-537

Comparison of control strategies for contact heating systems used in piglet nursery

Viktor ERDÉLYI, László FÖLDI, János BUZÁS
Department of Mechatronics, Institute of Technology, MATE, Gödöllő

Abstract

This paper shows the results of the building an extension of the existing SimSolar framework. This paper focuses on setting up user circuit models. The result of this research is a complete model framework that can be used to simulate contact heating systems with liquid working medium to be able to optimize the control algorithms and strategies used in these types of solutions.

Keywords

block oriented, simulation, thermal, livestock, modeling

1. Introduction

The number of researchers exploring the possibilities of using renewable energy sources has increased significantly in recent decades, due to the growing demand for energy, the finite amount of fossil fuels and the environmentally conscious way of thinking. Environmentally conscious thinking can be observed more and more in agriculture as well, so the use of solar energy is also more and more typical in the case of livestock farms. In the case of pig farms, this is often used to supplement existing fossil fuel-based or electric heating systems with varying efficiencies.
According to literature sources, solar energy is now increasingly used for heating purposes in both industry and agriculture (Xie et al., 2019).

In my experience, solar thermal floor heating systems used in pig farms are often unable to maintain the expected temperatures because they are systems with a large time constant (Kull et al., 2019) and have a lot of parameters (Lu et al., 2020). Therefore, farmers are choosing more expensive to use electric underfloor heating instead of systems that use the sun's energy directly.

Both the Hungarian and international literature discusses the sub-field of control technology, which aims at the optimal utilization of renewable resources and solar systems in detail. Nowadays, this is a cutting edge and evolving research sector. A little researched area, however, is the thermal utilization of solar energy in temperature-sensitive areas such as the contact heating pads in piglet nurseries, where piglet comfort is the highest priority to avoid stress (Johnson et al., 2018), which adversely affects animal development.

During the research, the aim is to examine control algorithms that can provide adequate temperature control of systems with large time constants, further developing the methods for this area and establishing the limits of applicability.
The goal was to build a small-scale model made of a network of contact heating plates with liquid working medium used in pig breeders connected to a heating auxiliary thermal solar energy utilization device, which allows testing different control algorithms (On-Off, PID), different interventional devices. (pump, throttle valve)

2. Materials and methods

In this chapter, the experimental methods and tools used to achieve the goals of this research will be presented, which are the established model library to achieve a framework that can be used to quickly and precisely compare multiple control algorithms and strategies used in heating systems.

Block-oriented modeling
In the course of the work, mathematical modeling and simulation of thermal systems used in animal husbandry were dealt with, for which a simulation program package is essential. Since the university has a MATLAB+Simulink program package license, this method was chosen.
The Simulink program package is the Toolbox of the MATLAB system, i.e. its addition. Simulink is a block-oriented modeling software developed for the simulation of dynamic systems.

The system contains the basic units from which mathematical models describing the solar energy utilization system can be built, which are mostly ordinary differential equations. The Simulink system includes commonly used algorithms for its numerical solution, such as Runge–Kutta or Dormand–Prince (Ashino et al., 2000), i.e. it is a perfect choice for the realization of the goals set in this paper.

The simulations used in the paper to examine the thermal systems were created using version 9.2 of the Simulink environment.

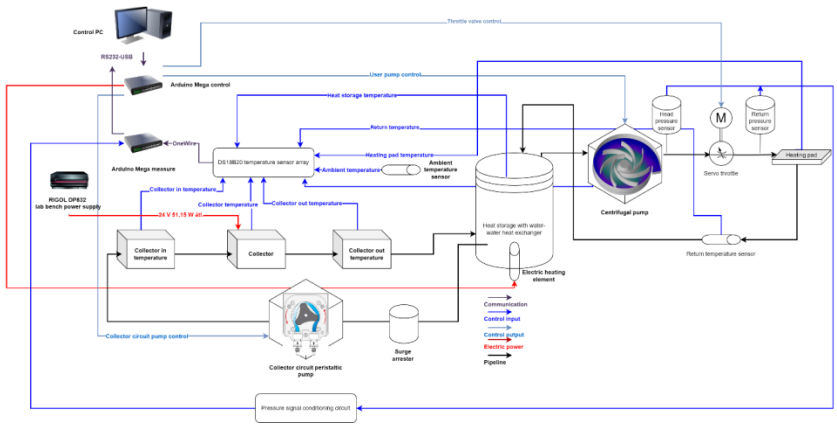

Figure 1. Block diagram of small-scale model

Small-scale model
The mathematical model was identified and validated on a small-scale system, the block diagram of which is shown in Figure 1.

3. Results and discussion

In this chapter the used and newly created models are presented.

The used solar collector model
In solar thermal systems, solar collectors convert the radiant energy of the Sun into heat. Therefore, these devices form the main element of the utilization system, since the goal of the system is optimal energy collection and transmission, which primarily takes place here. The used model of the SimSolar (Tóth, Farkas, 2017) system is presented below.
The Hottel-Whillier (H-W) model for the solar collector is specified as shown in Figure 2. (Tóth, Farkas, 2019).

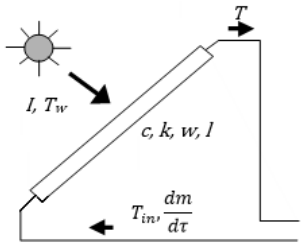

Figure 2. Schematic diagram of solar collector

Based on these, the equation describing the model is as follows:

$$T_{co}(\tau) = T_w(\tau) + \frac{I(\tau)}{\kappa_{aw}} + \left(T_{ci}(\tau) - T_w(\tau) - \frac{I(\tau)}{k_{aw}}\right) \exp\left(-\frac{\kappa_{mw} w l}{c\frac{dm}{d\tau}}\right). \quad (1)$$

The vast majority of the parameters in the model can be measured or are catalog data, but the direct measurement of the global heat transfer factors κ_{aw} and κ_{mw} can be difficult, since they include all forms of heat transfer between the two named units, so they must be identified for the selected solar collector in almost all cases. Hereafter, these global heat transfer factors as ″heat transfer factors″ will be refered.

Figure 3. shows the implementation of the block.

To use the block in simulation, the following parameters must be set:

- specific heat of the heat transfer medium (J kg^{-1} K^{-1}),

- solar collector width (m),
- solar collector length (m),
- heat transfer coefficient between the absorber and the environment (W m^{-2} K^{-1}),
- heat transfer coefficient between the heat transfer medium and the environment (W m^{-2} K^{-1}).

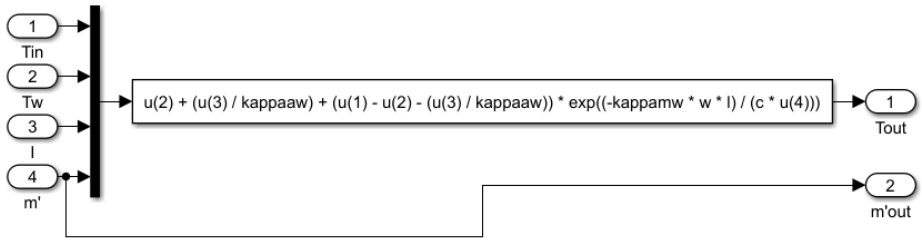

Figure 3. Implementation of H-W block in Simulink

The remaining, partially physics based, partially black box models which are describing the operation of the small-scale model will be identified based on the data of the measurements performed on the small-scale. This will be discussed in detail in the results of the 3.8. Identification of models subchapter.

Model identification and validation

The mathematical models used often need to be identified, as certain parameters cannot be determined by measurement. In this section, the identification procedure of the models used in the work will be presented.

During the identification task, the goal is to determine the unknown parameters of the model based on the measurement results, so that the simulation with the specified parameters comes as close as possible to the measurement results. To complete the task, the deviation as an objective function on the examined interval was defined $[\tau_0; \tau_1]$

$$J(p_1, p_2, \ldots, p_j) = \int_{\tau_0}^{\tau_1} \left(y(t) - \hat{y}(\tau, p_1, p_2, \ldots, p_j)\right)^2 dt. \quad (2)$$

The measurements were made at discrete moments of time, and the simulation uses a numerical solution method, so the discrete form of the objective function was also used, which in the case of n measurement points:

$$J(p_1, p_2, \ldots, p_j) = \sum_{i=1}^{n} \left(y(i) - \hat{y}(i, p_1, p_2, \ldots, p_j)\right)^2. \quad (3)$$

The goal of the identification task is to minimize the target function, that is, to find the parameters $p_1, p_2, \ldots, p_j$ for which the value of the J function is minimal:

$$\min_{p_1, p_2, \ldots, p_j} J(p_1, p_2, \ldots, p_j) \rightarrow p_1, p_2, \ldots, p_j. \tag{4}$$

During the tests, the minimization using a gradient-based local minimum search was used. The results confirm the correctness of this choice, so global minimum search procedures weren't necessary.

The following models based on the measurements made on a small-scale were set and identified in case of physical models.

Based on measurement results, the pump model was created as a black box model, which is a combination of a symmetrical sigmoid and a linear function. While the pump motor was operated at several power levels using PWM, the data was recorded while the pressure side of the pump was gradually throttled. Figure 4. shows the three-dimensional surface describing the behavior of the pump.

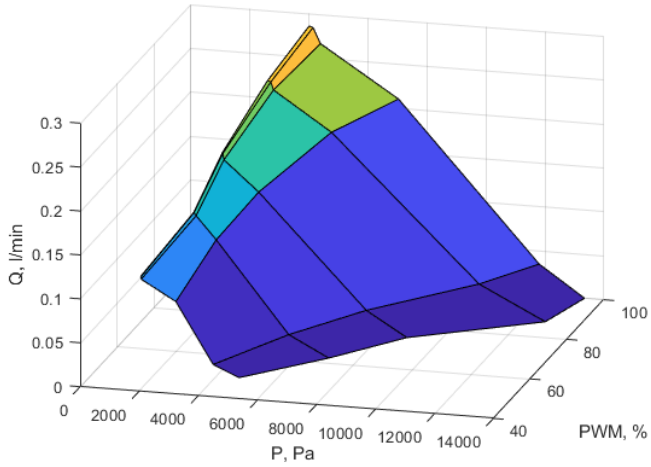

Figure 4. Pressure and flow data for operating the pump at different power levels and throttles

The model describing mass flow:

$$y_1 = d_1 + \frac{a_1 - d_1}{1 + \left(\frac{\xi}{c_1}\right)^{b_1}} \tag{5a}$$

$$\frac{dm}{d\tau} = (a_2\, \zeta + b_2)\, y_1 \tag{5b}$$

Model describing pressure:

$$y_3 = d_3 + \frac{a_3 - d_3}{1+\left(\frac{\xi}{c_3}\right)^{b_3}} \tag{6a}$$

$$\Delta p = (a_4\,\zeta + b_4)\,y_3 \tag{6b}$$

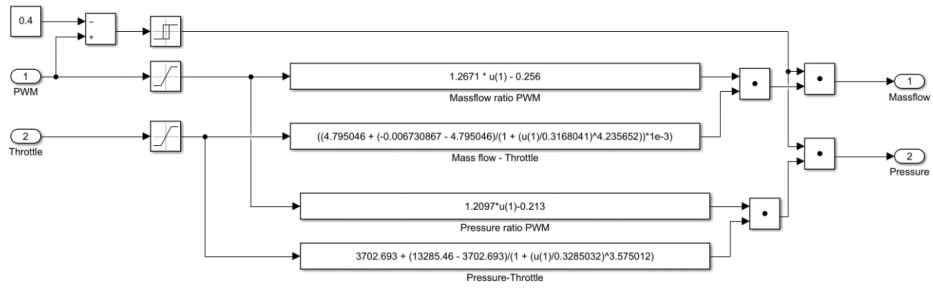

Figure 5. Simulink implementation of the pump model

In the implemented model, there are two saturation blocks to be seen, in conjunction of a relay and a differential block. Their task is to narrow the control signals coming from the controller to the applicable intervention range, since in the case of pulse width modulation (PWM) intervention signals below 50% and above 100% cannot be interpreted. The reason for this is that, due to the technical limitations of the motors, it is not safe to run them at less than 50% power, as the minimum starting torque required to set the rotor in motion is not ensured here. Accordingly, if the control signal is below 50%, the motor will not be started, and thus the output flowrate will be equal to zero.
Parameters sought for model identification: a_i, b_i, c_i, d_i

Throttle model
The throttle model uses the Toricelli equation, which can be derived from the Bernoulli equation (Bärnkopf et al, 1984), which calculates the volume flow through the choke based on the effective flow cross-section obtained from the measurements, as well as the system pressure. The value of the effective flow cross-section as a function of the throttle position is described by a symmetrical sigmoid function, which was based on measured values.

$$\mu\,A_f = d_4 + \frac{a_5 - d_4}{1+\left(\frac{\xi}{c_4}\right)^{b_5}} \tag{7a}$$

$$Q_v = \mu\,A_f\sqrt{\frac{2}{\rho}\,\Delta p} \tag{7b}$$

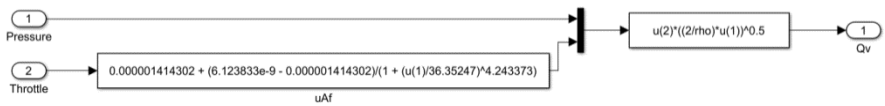

Figure 6. Simulink implementation of the throttle model

Parameters sought for model identification: a_5, b_5, c_4, d_4

Storage model

The heat storage model with a heat exchanger (Farkas, 1999) was extended with an additional electric heater input. The model includes the heat released to the environment on the surface of the tank.

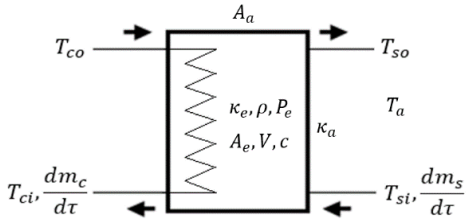

Figure 7. Schematic diagram of the heat storage

The full mathematical model is as follows:

$$T_{ci}(\tau) = \left(T_{co}(\tau) - T_{so}(\tau)\right)\exp\left(-\frac{\kappa_{em}\, A_e}{c\,\frac{dm_c}{d\tau}}\right) + T_{so}(\tau), \tag{8a}$$

$$c\, V\rho\, \frac{dT_{so}}{d\tau} = c\, \frac{dm}{d\tau}\, \left(T_{si}(\tau) - T_{so}(\tau)\right) + c\, \frac{dm_c}{d\tau}$$
$$\left(T_{co}(\tau) - -T_{ci}(\tau)\right) + P_e - \kappa_{aw}\, A_a\, \left(T_{so}(\tau) - T_w(\tau)\right). \tag{8b}$$

The global heat transfer factor κ_{aw} includes all forms of heat transfer between the heat storage medium and the environment. The global heat transfer factor κ_{em} includes all forms of heat transfer between the heat storage medium and the medium flowing in the heat exchanger coil.

According the above equations, the Simulink implementation is also made up of two parts (Figure 8).

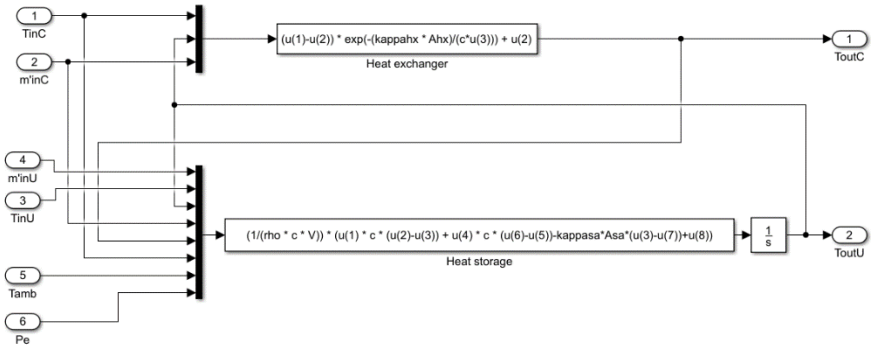

Figure 8. Simulink implementation of heat storage block

- specific heat of the heat transfer medium (J kg^{-1} K^{-1}),
- density of heat transfer medium (kg m^{-3}),
- heat exchanger surface (m^2),
- heat storage surface (m^2),
- heat storage volume (m^3)
- heat exchanger heat transfer coefficient (W m^{-2} K^{-1}),
- heat storage heat transfer coefficient (W m^{-2} K^{-1}),
- initial temperature (°C).

Parameters sought for model identification: κ_{em}, κ_{aw}.

Heating pad model

The simplification used in the heating plate model is that the temperature inside the heating plate is homogenous, and that the temperature of the heating plate's surface is the same as the temperature of the exiting water.

$$c\ m\ \frac{dT_p}{d\tau} = c\ \frac{dm_{in}}{d\tau}\ \left(T_{in}(\tau) - T_p(\tau)\right) -\ \kappa_{pw} A_p\ \left(T_p(\tau) - T_w(\tau)\right) \qquad (9)$$

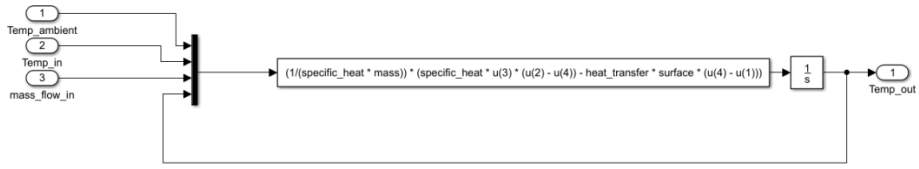

Figure 9. Implementation of the heating plate model in a Simulink environment

- specific heat of the heat transfer medium (J kg^{-1} K^{-1}),

- mass of water in the heating plate (kg),
- heating plate surface (m^2),
- heat transfer coefficient (W m^{-2} K^{-1}),
- initial temperature (°C).

Parameter sought for model identification: κ_{pw}.

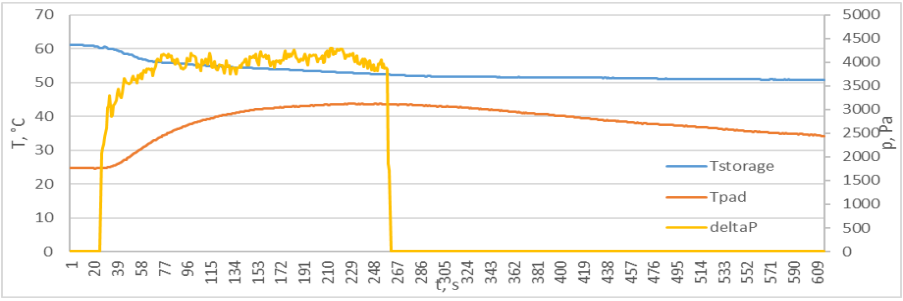

Figure 10. Measurement data set used to identify the model

Identification of models

Figure 10. shows the measured data on small-scale system used to identify the user circuit models

Figure 11. shows the of cooling of the heating pad used to identify the surface heat transfer coefficient.

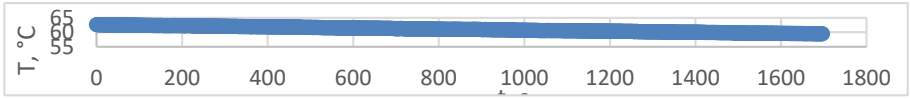

Figure 11. Measurement data series used to validate the surface heat transfer coefficient

Identification of heat storage model

The equation below shows the objective function used to identify the parameters of the heat storage.

$$J_1(\kappa_{em}, \kappa_{aw}) = \int_0^{600} \left(y(\tau) - \hat{y}(\tau, \kappa_{em}, \kappa_{aw})\right)^2 d\tau. \quad (10)$$

Identification of heating pad model

The equation below shows the objective function used to identify the parameters of the heating pad.

$$J_2(\kappa_{pw}) = \int_0^{600} \left(y(\tau) - \hat{y}(\tau, \kappa_{pw})\right)^2 d\tau. \quad (11)$$

Conclusions

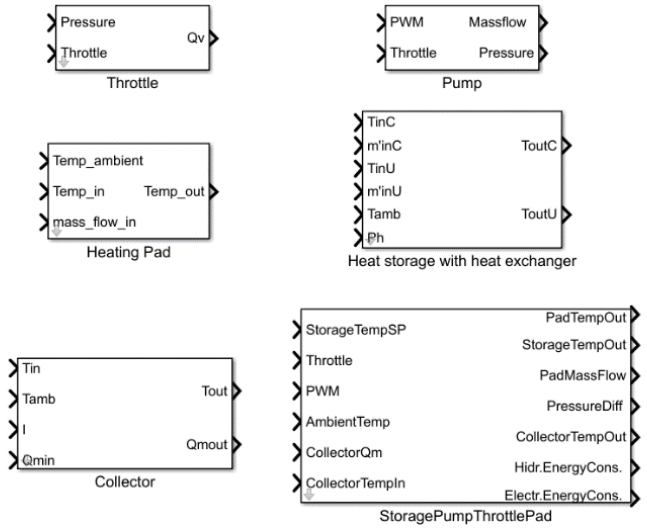

Figure 12. Model library for the block-oriented simulation framework

For further research a new block-oriented model framework was established. The framework is built from the following blocks:

- Throttle model
- Pump model
- Heating plate model
- Heat storage model, with heat exchanger, built-in additional electric heating, with surface heat transfer
- Hottel-Whillier solar collector model
- Combined storage, heating plate, pump, throttle model, which also includes the step-by-step electric heating power regulator that regulates the temperature of the heat storage and the blocks that calculate the electrical and hydraulic energy used

List of symbols

A	surface	[m^2]
A_a	surface in contact with the environment	[m^2]
A_e	heat exchanger surface	[m^2]
A_f	orifice cross section	[m^2]
A_p	pad surface	[m^2]
P_e	electric heating capacity	[W]

Q_v	volumetric flowrate	[m^3/s]
T_{ci}	temperature of the heat transfer medium entering the solar collector	[°C]
T_{co}	temperature of the heat transfer medium leaving the solar collector	[°C]
T_{in}	inlet temperature	[°C]
T_p	heating pad temperature	[°C]
T_{si}	temperature of the heat transfer medium entering the heat storage	[°C]
T_{so}	temperature of the heat transfer medium leaving the heat storage	[°C]
T_w	ambient temperature	[°C]
$a_{1,2,3,4,5}$	parameter to be identified	[-]
$b_{1,2,3,4,5}$	parameter to be identified	[-]
$c_{1,3}$	parameter to be identified	[-]
$d_{1,3,4}$	parameter to be identified	[-]
m_c	the mass of the heat transfer medium of the solar collector	[kg]
m_{in}	entering mass	[kg]
p_j	general parameter	[-]
$\hat{y}$	output of a simulated system	[-]
y_1, y_3	parameters of black-box model	[-]
κ_{aw}	heat transfer coefficient between the absorber and the environment	[W/m^{2}K]
κ_{em}	heat transfer coefficient between the heat exchanger and the heat transfer medium	[W/m^{2}K]
κ_{mw}	heat transfer factor between the heat transfer medium and the environment	[W/m^{2}K]
κ_{pw}	heat transfer coefficient between pad and the environment	[W/m^{2}K]
I	solar radiation intensity	[W/m^2]
J	objective function	[-]
V	volume	[m^3]
c	specific heat	[J/kgK]
l	solar collector length	[m]
m	mass	[kg]
p	pressure	[Pa]
w	solar collector width	[m]
y	system output	[-]
ζ	motor performance	[%]
μ	flow coefficient	[-]
ξ	throttle position	[%]
ρ	density	[kg/m^3]
τ	time	[s]

References

[1] Ashino R., Nagase M., Vaillancourt R. (2000): Behind and beyond the MATLAB ODE Suite, Computers & Mathematics with Applications, Vol. 40, No. 4-5, pp. 491-512, doi: 10.1016/S0898-1221(00)00175-9
[2] Bärnkopf R., Ezer R., Kiss P., Máté S. (1984) Hidraulikus rendszerek tervezése, Műszaki Könyvkiadó, Budapest, p. 377, ISBN: 963-10-5744-7
[3] Farkas I. (1999): Számítógépes szimuláció, Egyetemi jegyzet
[4] Johnson, J.S., Aardsma, M.A., Duttlinger, A.W., & Kpodo, K. R. (2018). Early life thermal stress: impact on future thermotolerance, stress response, behavior, and intestinal morphology in piglets exposed to a heat stress challenge during simulated transport. Journal of Animal Science, 96(5), pp. 1640-1653.
[5] Kull, T. M., Thalfeldt, M., & Kurnitski, J. (2019). Estimating time constants for underfloor heating control. In Journal of Physics: Conference Series, Vol. 1343, No. 1, p. 012121. IOP Publishing.
[6] Lu, S., Gao, J., Tong, H., Yin, S., Tang, X., & Jiang, X. (2020). Model establishment and operation optimization of the casing PCM radiant floor heating system. Energy, 193, p. 116814.
[7] Tóth J., Farkas I. (2017) A simulink library for solar energy applications Mechanical Engineering Letters: R And D: Research And Development pp 89-95 HU ISSN 2060-3789
[8] Tóth J., Farkas I. (2019): Mathematical modelling of solar thermal collectors and storages, Acta Technologica Agriculturae, Vol. 23, No. 4, pp. 128-133., ISSN 1338-5267
[9] Xie, Q., Ni, J.Q., Bao, J., & Su, Z. (2019). A thermal environmental model for indoor air temperature prediction and energy consumption in pig building. Building and Environment, 161, p. 106238.

Examination of the safety functions of a pneumatic balancing system

László FÖLDI, Eszter MAYERNÉ SÁRKÖZI,
Department of Mechatronics, Institute of Technology, MATE, Gödöllő,

Abstract

In present article a pneumatic balancing system is examined, which is widespreadly used in the automotive industry. The subject of the examination is the methods to reduce the stopping time of the dangerous movements of the equipment. Reducing the stopping time is important because it is used to determine the minimum safety distance that must be between the operator and the actuator performing a dangerous movement. In the research a Safe stopping and closing safety function (SSC) was investigated, that is commonly applied in pneumatic systems. Besides that we examined other safety functions that are used in electric drives, but not in the case of pneumatic drives: SOS and SS2 safe stop. By applying the new safety functions, a shorter downtime was achieved and, as a result, a smaller minimum safety distance.

Keywords

servopneumatics, pneumatic balancer, safety functions, proportional pneumatics, functional safety

1. Introduction

Safety functions are critical points of any machines. The goal of the safety functions are to prevent any type of physical damage. Beyond the EC Machinery Directive there are several related standards (eg. EN ISO 12100, 2005; EN ISO 13849- 1, 2016), which describe the risk assessment process. In the following a risk analysis and evaluation of a servopneumatic system is performed with three different safety functions according to the related standards.

Figure 1 shows the pneumatic balancing system that is the subject of the present study. The basic task of the equipment is to assist the operator in lifting and moving heavy loads. With the manual setpoint generator, the operator commands the servo-pneumatic system to raise or lower the load, while in lateral direction the operator moves the mass by hand. Considering machine safety functions it is important that if the movement speed of the mass exceeds the value specified in the standard, the fall of the mass must be stopped as quickly as possible. ISO 14120 (ISO 14120, 2015) standard defines the kinetic energy of the moved mass as E = 4 J. Exceeding the specified speed is checked by a monitoring safety

function (SLS). When the speed limit is exceeded, the Safe Stopping and Closeing (SSC) safety function is activated (BGIA Report, 2008; IFA Report, 2019).

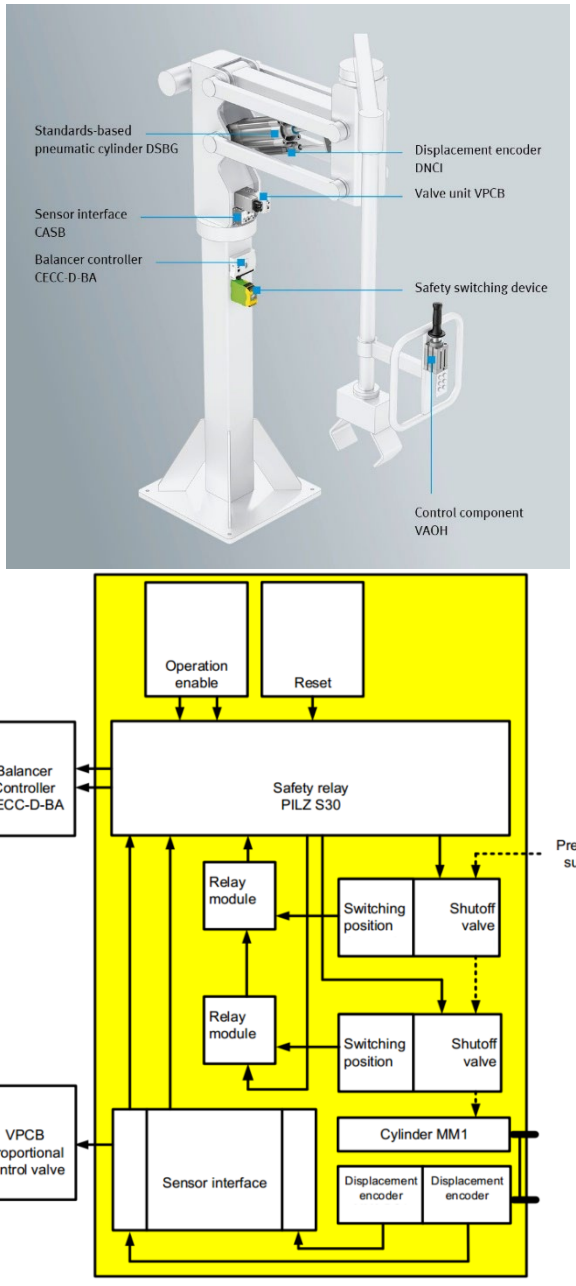

Figure 1. The pneumatic balancer system (Balancer kits YHBP, 2020, Application Note: YHBP, 2020)

Safety function used in fluid mechanical and electrical systems

One of the most frequently used safety functions for pneumatic drives is SSC (Safe stopping and closing). In this function the energy supply or energy outlet is closed in at least one chamber of the pneumatic actuator, and the stored energy is used to achieve stopping the motion. For all solutions, the safe condition is realized in the initial position of the monostable valves. This happens when the valve is not operated, so without control signal the valve is switched to inital position by spring (VDMA 24584, 2019).

The safety function used in electric drives is SOS (Safe Operating Stop). Stopping an electric motor with SOS function results that the stopped motor is moved to a given position, and the drive controller monitors the status. The SS2 (Safe Stop 2) function stops the motor quickly and safely, then activates the SOS function after stopping. Definition according to EN 61800-5-2 (IEC 61800-5-2, 2017): the SS2 function brakes the motor, monitors the amount of motor deceleration, and then after a delay time starts the SOS function.

Safely-limited speed (SLS) function ensures that the drive does not exceed the specified speed limit. Definition according to EN 61800-5-2 (IEC 61800-5-2, 2017): The SLS function prevents the drive from exceeding the specified speed limit. Its effect is that the drive reliably monitors the speed and activates the error reaction defined by the configuration in case of exceeding the set speed limit (Guideline for functional safety, 2019).

Application of safety devices taking into account the approach speed of human body parts (ISO 13855, 2010)

The measures that keep the operator in place, such as two-handed starters or, as in this application, the placement of the manual setpoint generator are provided for in the ISO 13855, 2010 standard. The safety distance (S) must be calculated based on the eq.1:

$$S = K * T + C \quad (1)$$

where K is the speed of approach, in this case it is 1600 mm/s, T is the downtime of the system [s], and C is an additional distance with value of 250 mm.

2. Experimental

Tested pneumatic balancer system

The balancer system moves loads of up to 999 kg effortlessly at the touch of a finger. The controller automatically detects the weight of the load and sets the balancing force itself. It also takes into account any weight changes in the suspended state. This is helpful in keeping production processes really flexible. The components of the balancer kit are suitable for installation in all common kinematic systems such as lifting columns or parallel kinematic systems. (see Fig. 1).

Features:

- Dual-channel speed monitoring

- Safety: Performance Level d achievable
- Safely limited speed (SLS)
- Safe stopping and closing (SSC)

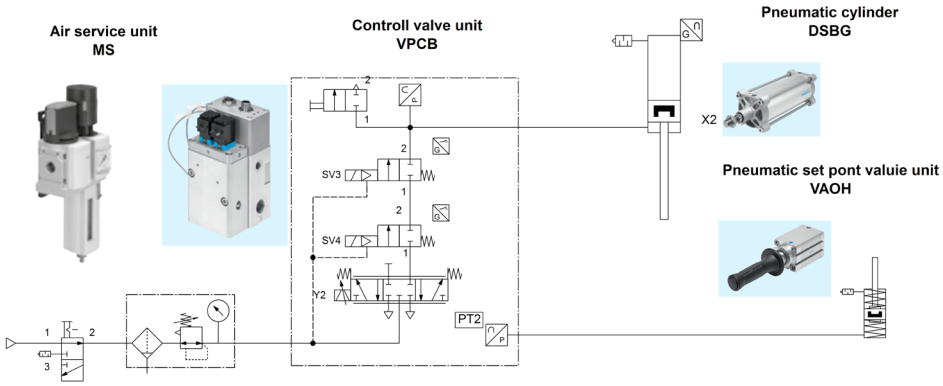

Figure 2. The pneumatic circuit diagram of the pneumatic balancer (Balancer kits YHBP, 2020)

The system components used:

Standards-based cylinder	DSBG-80-500-PPVA-N3
Displacement encoder	DNCI-32-500-P-A
Valve unit	VPCB-6-L-8-G38-10-F-D3-T22-M
Control element	VAOH-P15-H13
Plug socket with cable	KME-1-24DC-5-LED
Connecting cable	NEBC-M12G5-ES-5-LE5-CO
Balancer controller	CECC-D-BA
Plug	NECC-S1G9-C2-M
Proximity switch	SMT-8M-A-PS-24V-E-0.3-M8D
Sensor interface	CASB-MT-D3-R7
Connecting cable	NEBU-M12G5-K-5-LE4
Plug socket with cable	NEBU-M12W8-K-5-N-LE8
Safety relay unit	PNOZS30C24-240VACDC

The simulation of pneumatic balancer system

The main unit of the balancing system is a pneumatic cylinder. The working cylinder is equipped with a redundant displacement sensor due to the requirements of the standard. Redundancy is necessary to achieve of d level of PL (Performance Level). The SSC safety function implemented in case of overspeeding is performed by a shut-off valve combination consisting of 2/2 valves with redundant valve switching state feedback. The operator initiates the intervention with a setpoint generator equipped with a pressure sensor made of a pneumatic

cylinder. The intervention is implemented by a proportional way valve. The control process is managed by a controller programmed for this purpose based on the measured position of the cylinder and the pressure measured in the chamber of the cylinder. The examination of the system was implemented in the FluidSim 5 simulation environment.

3. Results and discussion

Implementation and results of the SSC security function

The SSC safety function results in an immediate stop of the pneumatic drive by locking the compressed air in the chambers of the working cylinder when the descent speed of the balancer cylinder exceeds the kinetic energy of 4 J defined in ISO 14120, 2015. The sensor subsystem is a redundant subsystem consisting of two DNCI displacement sensors. Diagnostics of the sensor subsystem, cross monitoring of input signals and intermediate results within the logic (L), temporal and logical software monitor of the program flow and detection of static faults and short circuits (for multiple I/O) are solved (DC = 99 %). The sensor subsystem is category 3 and PL e performance level. The power control subsystem for stopping the cylinder is implemented with the diagnosed valves SV3 and SV4. SV3 and SV4 valves are diagnosed by direct switching position status feedback, so the diagnostic coverage for both valves is DC = 99%. The performance control subsystem is category 3 PL e performance level. The control logic is a category 4 PL e performance level Safety controller. The resulting performance level of the entire safety function is PL d.

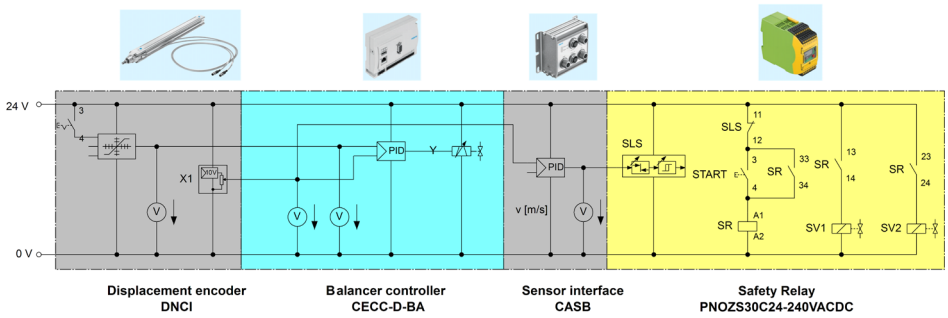

Figure 3. The SSC control logic

In the simulation, the first block of the electrical system is the sensor subsystem, which consists of a setpoint generator and a displacement meter. The second block contains the PID control block that implements the control of the working cylinder. The third part is the sensor interface, which in the present simulation consists of a derivative term with P=0, I=0 and a time constant D=50 ms, the output of which is thus the displacement speed in m/s. The last block is the part

that implements the SSC safety function, which consists of a comparator marked SLS, whose setting is the speed corresponding to the current energy E = 4 J. If the speed exceeds the set value, then the relay marked SR cuts off the power supply to the valve magnets SV1 and SV2, so they block the path of the exhausting air from the cylinder.

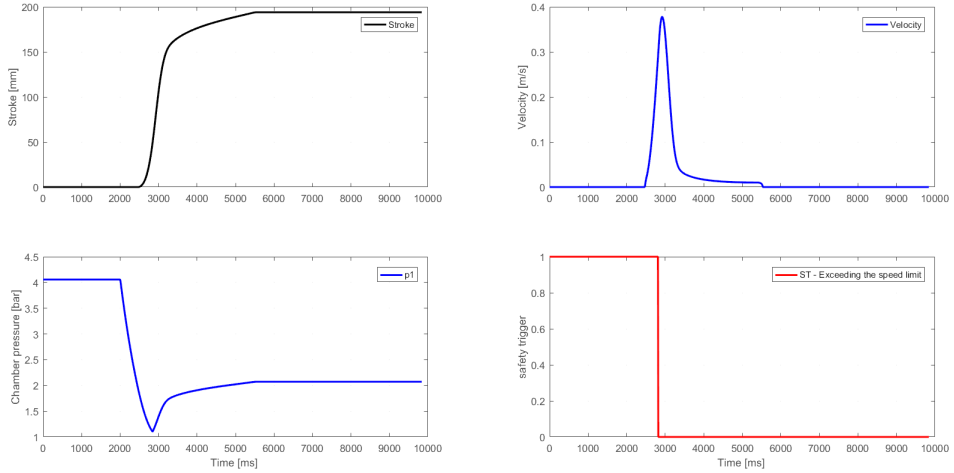

Figure 4. The results of the SSC simulation

Figure 4 shows the results of the simulation. The top left figure shows the displacement of the cylinder as a function of time. The top right figure shows the speed of the cylinder and the moved mass. The lower left figure shows the pressure developing in the chamber of the cylinder, while the lower right figure shows the crossing of the speed limit as a function of time. The simulation settings are the following: the moving mass is 100 kg, the static friction is 0.15, the sliding friction is 0.1, the speed limit is 0.283 m/s. The diagrams clearly show that when crossing the speed limit, the movement slows down rapidly, but nevertheless a considerable amount of overrun is visible after 2.61 s. The minimum safety distance (S) calculated from this is 4426 m, which cannot be applied in practice.

Implementation and results of the SS2 security function

The SS2 safety function starts by braking the pneumatic drive with the highest available torque, and after stopping, closes the compressed air in the chambers of the pneumatic cylinder when the descent speed of the balancer cylinder exceeds the kinetic energy of 4 J defined in the standard (ISO 14120, 2015). The sensor subsystem is a redundant subsystem consisting of two DNCI displacement sensors. Diagnostics of the sensor subsystem, cross monitoring of input signals and intermediate results within the logic (L), temporal and logical software monitor of the program flow and detection of static faults and short circuits (for

multiple I/O) are solved (DC = 99 %). The sensor subsystem is category 3 and PL e performance level. The power control subsystem for stopping the cylinder is implemented with the diagnosed valves SV3 and SV4. SV3 and SV4 valves are diagnosed by direct switching position status feedback, so the diagnostic coverage for both valves is DC = 99%. The performance control subsystem is category 3 PL e performance level. In addition to this, the braking is provided by a proportional valve with spool position feedback. The braking subsystem is category 2, PL d performance level. The control logic is a category 4 PL e performance level Safety controller. The braking control logic is a non-safety CECC-D-BA controller, category 1, with performance level PL c. The resulting performance level of the entire safety function is PL c.

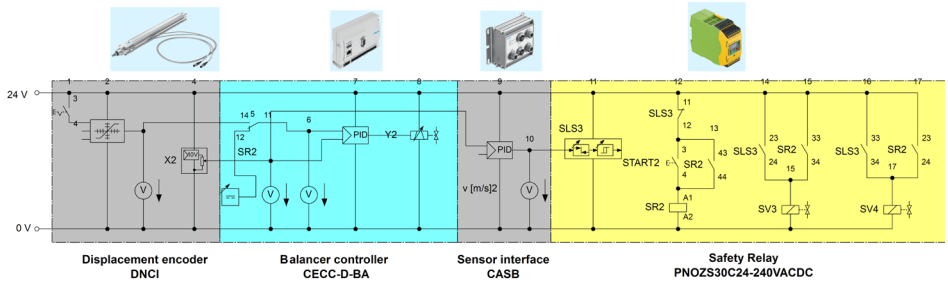

Figure 5. The control logic of SS2

In the simulation, the first block of the electrical system is the sensor subsystem, which consists of a setpoint generator and a displacement meter. The second block consists the PID control block that implements the control of the cylinder, and is supplemented with a setpoint changeover switch depending on the state of the SR2 relay, which increases the setpoint change at maximum speed when the speed limit is exceeded. The third part is the sensor interface, which in the present simulation consists of a derivative term with P=0, I=0 and a D=50 ms time constant, the output of which is thus the displacement speed in m/s. The last block is the part that implements the safety function SS2, which consists of a comparator marked SLS, which has a speed corresponding to the current energy E = 4 J. If the speed exceeds the set value, the relay marked SR2 does not disconnect the power supply to the SV3 and SV4 valve magnets immediately. Closing only occurs when the speed drops to 0.

Figure 6 shows the results of the simulation. The top left figure shows the displacement of the cylinder as a function of time. The top right figure shows the speed of the cylinder and the moved mass. The lower left figure shows the pressure developing in the chamber of the pneumatic cylinder, while the lower right figure shows the crossing of the speed limit as a function of time. The simulation settings are the flooowing: mass is 100 kg, static friction is 0.15, sliding friction is 0.1, speed limit is 0.283 m/s. The diagrams clearly show that when

crossing the speed limit, the movement slows down rapidly, and a slight overrun of T = 0.26 s is visible. The minimum safety distance calculated from this is S = 666 m, which is acceptable from a practical point of view. This significantly faster stopping results from the maximum braking force applied in the first phase of the safety function.

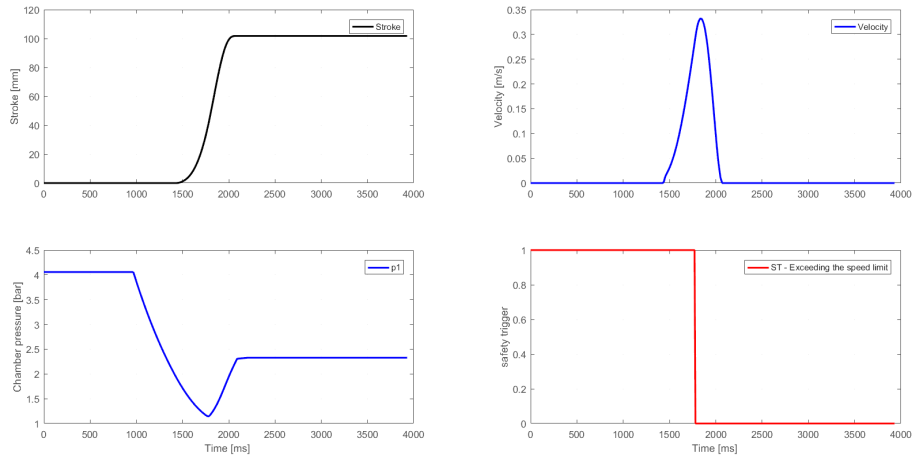

Figure 6. The results of SS2 simulation

The stopping speed limit (SLS- safely limited speed) depends on the kinetic energy defined in the standard as movements below 4 J kinetic energy is not dangerous according to the ISO 14120, 2015 standard. The speed values corresponding to 4 J kinetic energy depends on the mass are as follows:

Table 1. Simulation results SSC Safety function

Safety speed limit [m/s]	0,400	0,327	0,283	0,253	0,231	0,214	0,200
Mass [kg]	50	75	100	125	150	175	200
Runnig on time [s]	1,74	2,26	2,61	2,85	3,04	3,22	3,34
Safety distance [mm]	3034	3866	4426	4810	5114	5402	5594

Table 2. Simulation results SS2 Safety function:

Safety speed limit [m/s]	0,400	0,327	0,283	0,253	0,231	0,214	0,200
Mass [kg]	50	75	100	125	150	175	200
Runnig on time [s]	0,17	0,22	0,26	0,33	0,38	0,47	0,56
Safety distance [mm]	522	602	666	778	858	1002	1146

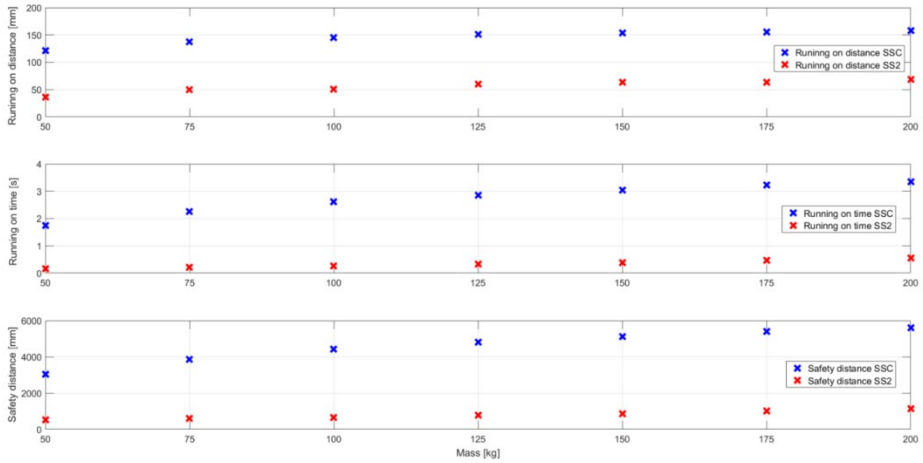

Figure 7. Overrun time of the SSC and the modified SS1 safety function depending on the moved mass

Figure 7 shows the difference in stopping performance between the SSC and SS2 safety functions as a function of the moved mass. The upper figure shows the continuation, the middle figure the overrun time, while the lower figure shows the minimum safety distance calculated from the overrun time according to ISO 13855, 2010.

Conclusions

- With SSC safety function applied the minimum safety distance (S) is 3034 mm, which is unacceptably large even for the smallest tested load, while it is 5594 mm for the largest tested load.
- With the SSC safety function, based on the results of the simulation, the overruning distances are not that much longer than the stop times, due to the stop speed characteristic.
- The SSC safety function can be applied up to performance level PL d.
- For the SS2 safety function, the minimum safety distances defined on the basis of the standard are acceptable in terms of the technologies used.
- The SS2 safety function corresponds to PL c performance level, without hardware modification.

References

[1] EN ISO 13849-1: Safety of machinery - Safety-related parts of control systems - Part 1: General principles for design (2016)

[2] EN ISO 12100: Safety of machinery. General principles for design. Risk assessment and risk reduction (2015)
[3] ISO 13855: Safety of machinery — Positioning of safeguards with respect to the approach speeds of parts of the human body (2010)
[4] BGIA Report 2/2008e (2009) Functoinal safety of machine controls-Application of EN ISO 13849. ISBN: 978-3-88383-793-2. ISSN: 1869-3491
[5] IFA Report 2/2017e (2019) Functional safety of machine controls – Application of EN ISO 13849. ISBN: 978-3-86423-232-9. ISSN: 2190-7994
[6] VDMA 24584: 2019, Safety functions of regulated and unregulated (fluid) mechanical systems
[7] IEC 61800-5-2: 2017 Adjustable speed electrical power drive systems – Part 5-2: Safety requirements – Functional
[8] Balancer kits YHBP [https://www.festo.com/hu/hu/a/8087218/?q=balancer~:festoSortOrderScored], 2020
[9] Application Note: YHBP - Servopneumatic Balancer Kit Design diagram, Example design diagram for a PLd Servopneumatic Balancerkit. PLd, Festo SE & CO. KG, D-73726 Esslingen, 2020
[10] Festo AG, Guideline for functional safety, 135242 (EN), 2019/05 [https://www.festo.com/net/SupportPortal/Files/13541/Guideline_Functional-safety_EN_2019_135242_L.pdf]
[11] MSZ EN ISO 14120 Safety of machinery. Guards. General requirements for the design and construction of fixed and movable guards (ISO 14120:2015)

Application of drone technology for facility management mainly for hazardous plants

István SZALKAI[1], Attila LÁGYMÁNYOSI[2], Péter Emőd KORZENSZKY[2], Aurél LUKÁCS[2], Zoltán BÁRTFAI[2]
[1]Doctoral School of Mechanical Engineering, MATE, Gödöllő
[2]Institute of Technology, MATE, Gödöllő

Abstract

One of the directions of our applied research is the development of non-commercially available drone devices, such as a sensor or sensor group that can be installed on a transport platform, that can be made suitable for continuous hazard control and prevention control of different kind of facilities (e.g warehouses. power plants). The drone devices can be optimized for performing measurements. Info communication system can contain closed-circuit data transmission and are suitable for transmitting experienced or measured data. Measuring equipment installed on drone devices is capable for autonomous operation that ensures their own mobility. The operation can be human-controlled or autonomous inspection of the detected object, so the measurement process can prevent continuous danger and support the surveillance.

Keywords

drone, inspection of hazardous plants, autonomous measuring instruments

1. Introduction

One of the directions of our research is to determine how drones can be used to measure technical data related to the operation of hazardous plants, and how measuring devices built on the developed drone platform can be suitable for integration into the measuring devices that monitor the operation of these plants (Gabryelewicz, 2021).

In most cases, during the examinations necessary for the assessment of official operating permits for the operation of hazardous plants, as well as during technical supervision work of industrial equipment, highly experienced specialists in difficult-to-reach and hazardous working conditions must work in industrial areas or on operating equipment (Kátai 2021).

The data of the manually controlled measurements and visual inspections will be processed during further office work after an on-site inspection, and the results will be documented and then analyzed. These inspection and supervision works are often preceded by significant scaffolding and crane preparation work. This is

all time-consuming, and involves significant costs. Recognizing this real market demand, we plan a research project focusing the development of a drone sensor system that would be uniquely new both for the enterprises operate hazardous plants or produce measuring equipment.

A measuring instrument or a group of them installed on a drone device would significantly improve the duration of the operational test process, increase the accuracy of the evaluation, simplify the performance of repetitive tests, and as a very important aspect, increase the enforceability of increasingly stringent occupational safety and health regulations (Rácz, 2017).

If the technical development objectives set are achieved, more cost-effective means would be available to operators of hazardous plants (e.g. heat and electric energy power plant), and at the time of their establishment, to their investors and contractors as well.

The main direction of our research is the development of an adequate test technology based on drone utilization, including the knowledge and the equipment as well in order to apply for different kind of plant detections mainly for elaborating the hazard deriving from the operation.

In the case of a successful development the technical supervisory burden could be reduced, and a more effective way of inspections cold be reached. The preparation and archiving of post-examination documentation can also be made much easier. As a result of these processes, the activities of the authorities supervising hazardous plants would also become more transparent and the administrative process to would also become significantly easier.

2. Experimental

Relevance of the drone applications

Drones, also known as Unmanned Aerial Vehicles (UAVs or Remotely Piloted Vehicles -RPVs), first appeared in the US military in the 1960s. The primary purpose of using drones was to minimize human casualties during military reconnaissance and to destroy enemy forces when used as weapons. After the war, it was used as a target device to train the air force, and now its primary function is to gather and transmit information using various sensors. In addition to military use, these developments have seen a steady expansion of public, commercial, research and private use.

One of the main considerations for industrial use today is still the protection of human life (for example, when working at high altitudes), but also, of course, cost-effectiveness and time-saving. For this reason, drones are increasingly being used in various facility maintenance investigations, as a remotely operated drone can reach places where human manpower would find it difficult or impossible to reach.

Drones can provide the operator or client with a visual image of the problem at hand in a variety of ways. A camera for visualization is an essential accessory of the drone, but in addition, thermal imaging, laser-based remote sensing,

ultrasonic, ultraviolet, hyperspectral, gamma and magnetometric measurements in hard-to-reach places are also possible. Thanks to the remote control of the cameras, we can obtain a realistic image of the roof of a tall building or even of critical equipment on the roof, without risking the safety of people. In addition to all this, the information obtained more quickly and the instant comparability speeds up the decision-making process and the ability to react.

Market potential

The magnitude of the market potential has already been outlined by the definition of the user target group. The number of investments in Hungary is constantly increasing, and at the same time, technical supervision, control, and planning are inevitable. Since this is often a time-consuming, costly and sometimes dangerous activity, in order to do this, it is necessary to develop a drone sensor system, which can be unique in the market. Overall, it is also known from the press that in the period we have been told, the preliminary number of Paks investments for on-site work is estimated at 10.3 billion dollars, while MOL Poliol's plant is 1.8 billion dollars, and the market volume of the related technical supervision activity can account for 1.5-3% of the 12 billion investments. If we look only at these two items, we can still see that there is significant market potential.

It is essential to identify all the **potential users** needed to make proper use of future developments. Before the technical development, we can determine exactly to whom and through what channels we can deliver the news and message of our product. Technology can generally be sold to companies that make a major investment, so they need a technical review and inspection process. There will always be such investments – this is evidenced by the fact that, based on the data of the HCSO, the value of investments shows a continuous increase from year to year. In the years 2019 and 2020, - before the COVID 19 pandemic period - the value of investments was HUF 11,000 billion per year at current prices (Restás 2022).

Manufacturing enterprises account for the largest share of these investments. With my development idea, it targets two groups: On the one hand, micro, small and medium-sized enterprises throughout the country that make investments where technical supervision activities are necessary, but whose company, due to the size of their company, do not have their own technical supervision capacity, their own metrology department, or a permanent full-time technical inspector. When planning this future measurement capacity-providing activity, we must consider the statistics containing official economic indicators, according to which manufacturing enterprises mainly account for most industrial investments, then according to the data of the Central Statistical Office (HCSO), there are more than 75,000 such companies in Hungary.

The technological solutions planned to be developed can make their operation faster and more economical and, above all, safe for them. Secondly, the use of the developed drone sensors can be understood primarily as a partial replacement of traditional inspection activities necessary for the technical supervision of oil, gas

and energy industrial facilities based on physical dimensions, extent, mass, and accessibility characteristics.

Green and brownfield investments, in-service inspections, large shutdowns (planned maintenance), reconstruction works affecting part or the entire operating environment. In such areas, the application of a drone sensor results in time and significant additional costs savings, and the development has a more accurate and reconstructed technical content. I would like to point out that in such a dangerous environment, the occupational health and safety aspects of workers come to the fore, which may be less substantiated by economic calculations, but can contribute to the operational safety of the given operating environment by improving the overall level of safety and protecting the health of workers.

In addition, the on-site evaluation of measurement and detection results can be solved by the work of fewer experienced senior experts, thus alleviating the persistent market shortage of labor. Potential development partners or users may be highlighted by the technical supervision of the petrochemical industry and the energy sector, including installation works outside the power plant circle, as well as the planned large shutdowns and maintenance works of conventional power plants, which induce large investments in the Hungarian economy. The main direction of the targeted applied research is the development and development of a non-commercially available sensor group that can be connected to a drone as a transport platform and are suitable for transmitting experienced, measured data, connected to an appropriate data transmission system. Regarding to the huge amount of data can be gathered in digital measuring processes preparation of useful information needs adequate analyzing technology (Bártfai et al., 2019).

In our research, the target is formulated in a development of a complex drone operating measuring system for special usage in detection of facilities mainly of hazardous energy plants (e.g waste incinerator).

Areas of the essential technical development:

1. technical facilities, drone devices for use in hazardous operating environments,
2. gas detection sensors,
3. temperature and vapor's saturation meters,
4. vibration meters,
5. surface and material wall thickness meters,
6. surface protection layer thickness meters

Main modules of the drones

Drones are complex mechatronic systems containing mechanical, electronical and info-communication units (**Figure 1**).

The **drone frame** is usually a very lightweight support structure made of solid carbon fiber, fiberglass or injection molded plastic, to which the other elements are attached.

The common feature of **control electronics** is that they all contain at least one microcontroller and one gyroscope sensor. The microcontroller runs the program

written in the flash ROM, which can be updated independently of the manufacturer to add new functions. The gyroscope is the basic unit that transmits data to the microcontroller about the drone's instantaneous pitch angle and pitch direction. These special gyroscopes sense along three axes that promote forward-backward, right-left and vertical axis rotation.

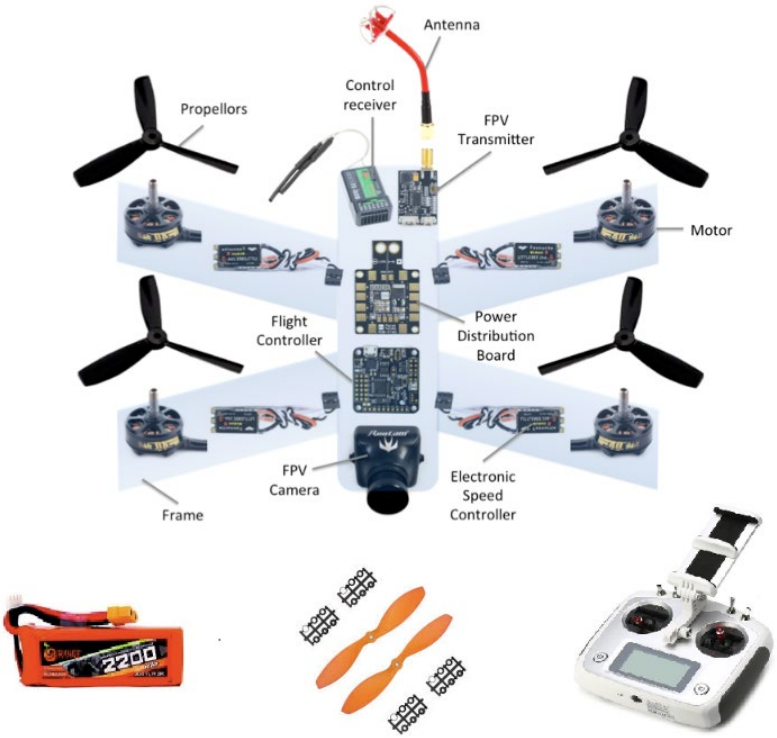

Figure 1. Main components of a drone (https://robu.in/product-category/drone-parts/)

Other components connected to the controller allow additional functions: **acceleration sensor** (ACC), **barometer sensor** (BARO), **magnetometer sensor** (MAG), GPS receiver. These components are essential for the use of a professional drone

The **drone motor** is usually a carbon brushless electric motor, on which the propeller is mounted. Each motor is connected to a control circuit, called ESC (Electronic Speed Controller), which controls the speed of the motors, adjusts their direction and, if necessary, controls the braking of the motors.

Most drones are designed with 4 arms, so they have 4 double-sided **propellers**. The more arms and propellers, the more stable the device can hold itself in the air and the more precisely the controller can distribute the speed of a given motor to compensate for weather conditions. The choice of materials for propellers is

typically divided into three main groups: wood, carbon fiber plastic, glass fiber reinforced plastic.

Lithium-Polymer batteries are almost invariably used for drones, as they are relatively lightweight yet can deliver a high current in a short time and do not take long to recharge. Their best feature is that they have no so-called memory effect and can store their capacity for a long time with little loss. However, they have the disadvantage that they can catch fire if hit and require a special charger to charge them.

Drones can be equipped with a wide range of sensors for different measuring tasks that can be performed during flying. **Figure 2.** shows one of our experimental drones having self-developed data logging and sampling system.

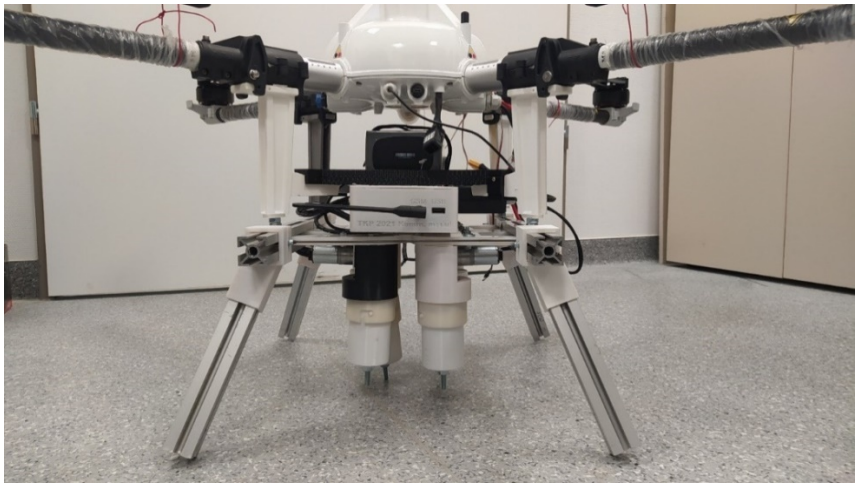

Figure 2. Experimental drone equipped with data logging and sampling system (self-made photo)

The continuous and smooth operation of a plant/industry/building requires continuous maintenance and monitoring of equipment whose breakdown or failure could cause serious material damage. For these inspections, it would be sufficient in many cases today to use a drone that can be programmed and self-controlled to scan a permanently inspected area at certain intervals and then send the data to a specified location or save it to its own storage. However, even if a programmable drone is not required, a single person who is familiar with drone control and the associated software is sufficient. Thanks to the high quality of the images, and the complementary laser scanning or thermal imaging, you can get a more comprehensive picture of the object than direct visual inspection, as the videos and images can be viewed back by a professional to analyze and make the right decision.

Thanks to developments, drone support systems are expanding. The drone, when connected to a sophisticated enterprise asset management system (EAM),

can upload images and collected data, generating historical data to help set standards for facility management. All this can successfully support economic savings through more efficient resource management and more predictable processes.

There is a growing demand in the market for drone inspection methods for the exterior maintenance of buildings for design, construction, as-built assessment, operation, maintenance, purchase, rental, etc. The specific characteristics of a given drone make it suitable to perform a variety of jobs. The first and most important task, if we want to carry out a drone survey, is to define the specific survey, and the survey environment.

Drones in the facility management

The continuous and smooth operation of a plant/industry/building requires continuous maintenance and monitoring of equipment whose breakdown or failure could cause serious material damage. For these inspections, it would be sufficient in many cases today to use a drone that can be programmed and self-controlled to scan a permanently inspected area at certain intervals and then send the data to a specified location or save it to its own storage. However, even if a programmable drone is not required, a single person who is familiar with drone control and the associated software is sufficient. Thanks to the high quality of the images, and the complementary laser scanning or thermal imaging, you can get a more comprehensive picture of the object than direct visual inspection, as the videos and images can be viewed back by a professional to analyse and make the right decision.

Thanks to developments, drone support systems are expanding. The drone, when connected to a sophisticated enterprise asset management system (EAM), can upload images and collected data, generating historical data to help set standards for facility management. All this can successfully support economic savings through more efficient resource management and more predictable processes.

Figure 3. Drone application for facility detection
(https://www.engineering.com/story/automating-facility-inspection-with-drones)

There is a growing demand in the market for drone inspection methods for the exterior maintenance of buildings for design, construction, as-built assessment, operation, maintenance, purchase, rental, etc. The specific characteristics of a given drone make it suitable to perform a variety of jobs. The first and most important task, if we want to carry out a drone survey, is to define the specific survey, the survey environment.

Condition assessment, operation, maintenance

The simplest and most widespread use of drones clearly falls under this heading. These are the operations that require a lot of inspection, which drones are most effective at. Furthermore, if you only need simple visual inspection, you don't even need to buy a drone for that purpose for an astronomical amount of money, as the core will be a camera with good resolution.

Obviously, when it comes to condition surveys, we are talking about both exterior and interior areas, so the drone must meet some of the expectations that the owner or even the operator of the facility has of the device:

- one of the most important is the stable recording of both images and videos
- the drone should not be too large, as there are confined spaces within the facility where it should be able to fit and access
- maintain reliable communication with the aircraft communicating with it
- sensors to detect and correct the direction of travel if the drone hits something
- be equipped with sensors, cameras and devices that allow the maximum number of possible uses to be made of it
- be easy to operate, maintain and reliable

It is always worth choosing the drone that gives you the most options at the best value for money.

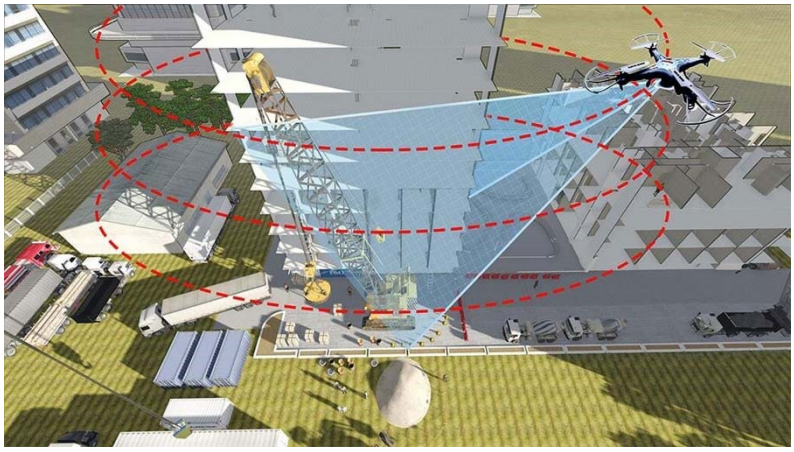

Figure 4. Drone application for building and surrounding inspection
https://www.bimcommunity.com/news/load/447/drones-the-perfect-tool-for-facility-inspections

Thermal detection

Thermal imaging cameras mounted on drones can be used effectively in a number of areas during facility management:

- Fire protection and control
- Fire protection and fire protection
- Solar and wind power plant inspection
- Inspection of thermal bridges
- Roof structure inspection, finding leaking points

Infrared roof inspection is a proven method for detecting trapped moisture problems in flat roofs. Infrared roof Thermography can prevent equipment down time, production losses and help building owners and property management companies find roof problems. Due to the high cost of replacing a damaged roof, Thermographic roof inspections should be performed whenever a building is purchased, sold or leased. Infrared roof surveys provide the diagnostic information necessary for developing an effective roof maintenance program, planning capital budgets and for making informed decisions when considering roof repairs, replacement or resurfacing with one of the popular new roof coatings.

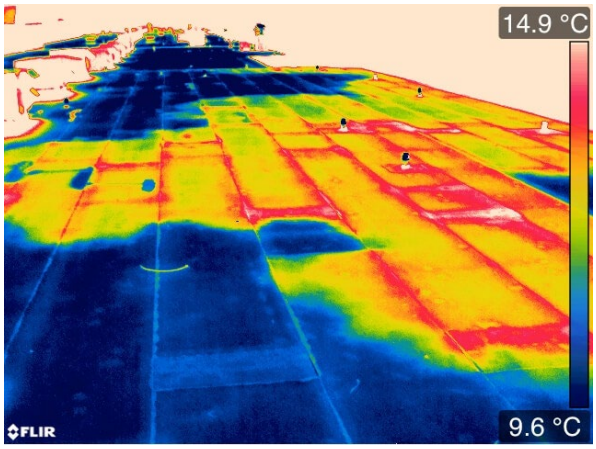

Figure 5. Infrared roof moisture survey
https://www.infraredimagingservices.com/roof-scan-ir/

Ultrasound examination

In unmanned aircraft inspections, we can mainly use techniques that are non-destructive material tests and do not require physical contact. The integration of ultrasonic sensors in drone facility maintenance, however, requires that the sensor mounted on the drone be capable of some form of physical contact with the object under test. The physical principle of ultrasonic testing is that ultrasound entering the observed object propagates through the material until it reaches a defect or contamination, i.e. an acoustic interface from which some of the ultrasound is

reflected. The reflected acoustic energy is determined by the ratio of the acoustic hardness of the materials on either side of the interface, the angle of incidence, the geometry of the interface, the longitudinal/transverse type of ultrasound and the frequency. To perform this test, a special instrument is required that is capable of both generating ultrasound and detecting its reflected sound waves.

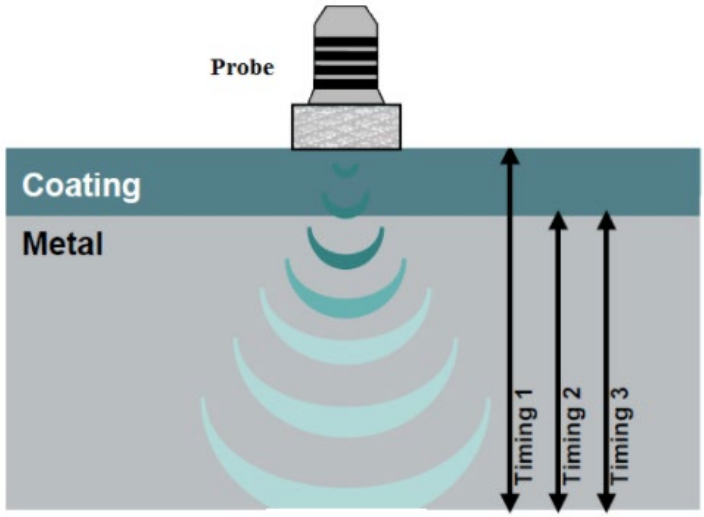

Figure 6. The deployed ultrasonic probe and testing method (https://inspectioneering.com/journal/2018-04-25/7567/development-of-a-wall-sticking-drone-for-non-destructive-ultraso)

The test can be used to determine not only the location of the reflection but also the extent of the reflection, which can be used to draw conclusions about the size of the reflecting surface. An important factor during the test is that the surface with which the probe is in contact should not be rusty or have poor surface quality, as these prevent the ultrasound from penetrating the part.

Ultrasonic testing is used for wall thickness measurement, quality control of welds, castings, forged and machined parts.

Wall thickness measurement requires a digital instrument specially developed for this purpose. The accuracy of the measurement can be affected by the surface smoothness, the test head and the instrument, and the thickness of the wall to be measured. If the test is carried out in a suitable measuring environment, a measurement accuracy of +-0.1mm can be achieved. For ultrasonic flaw detection using perpendicular heads, a digital/analogue pulse/response instrument is used. The technology is suitable for the detection of surface and internal defects, which can be significantly affected by material quality (e.g. excessive grain size), material thickness (>8 mm), or highly structured surfaces, surface irregularities.

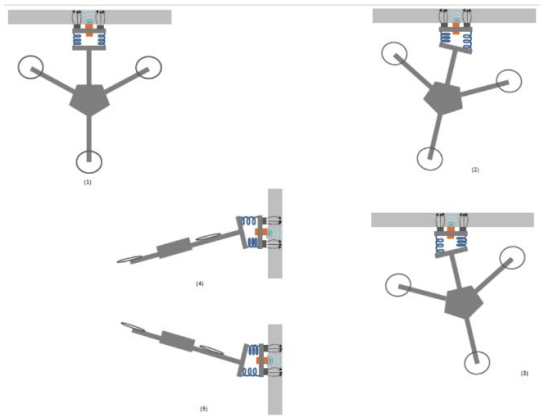

Figure 7. Different scenarios the drone experiences during wall-sticking (https://inspectioneering.com/journal/2018-04-25/7567/development-of-a-wall-sticking-drone-for-non-destructive-ultraso)

Figure 8. clearly shows that the propellers have been fitted with extra protection to avoid a possible collision and thus damage to the drone. An extension arm was mounted on the frame of the body in the middle, with a support plate fixed to the end. This plate is connected by dampers to the plate on which the electromagnet and the ultrasonic unit are mounted. This damping is necessary due to the motion of the drone. While the drone is in the air, it allows the drone body to move to a certain level relative to the probe, while the probe is held against the test piece by the electromagnet. This relatively simple method successfully eliminates both x and y deflections, preventing the probe from moving away from the surface to be measured.

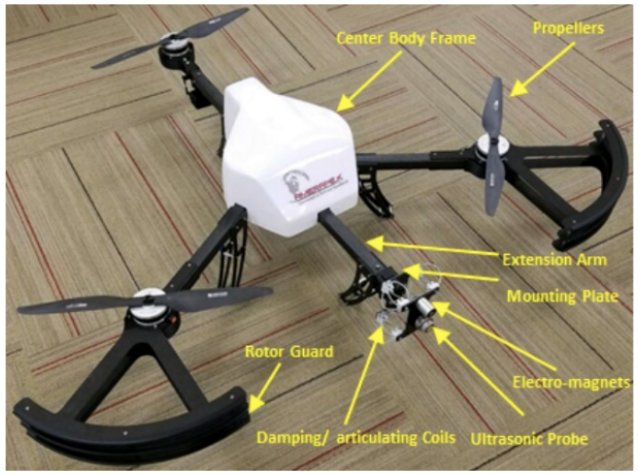

Figure 8. Drone for ultrasound examination (https://inspectioneering.com/journal/2018-04-25/7567/development-of-a-wall-sticking-drone-for-non-destructive-ultraso)

Drones are not only capable of visual inspections, but also of non-destructive inspections that require physical contact, such as ultrasonic material testing. Condition assessment and operation may also involve inspecting the floor structure, load-bearing walls and eaves of the facility. This requires more specialised inspection methods and therefore less material is available for such inspections, so this is also an untapped area for drone-based inspections. Condition surveys can therefore be profitable with a drone, since it is possible to determine the expected time for maintenance and repair, prevent certain material damage and at the same time reduce maintenance costs and the risk of accidents at work

3. Results and discussion

System design of a test drone

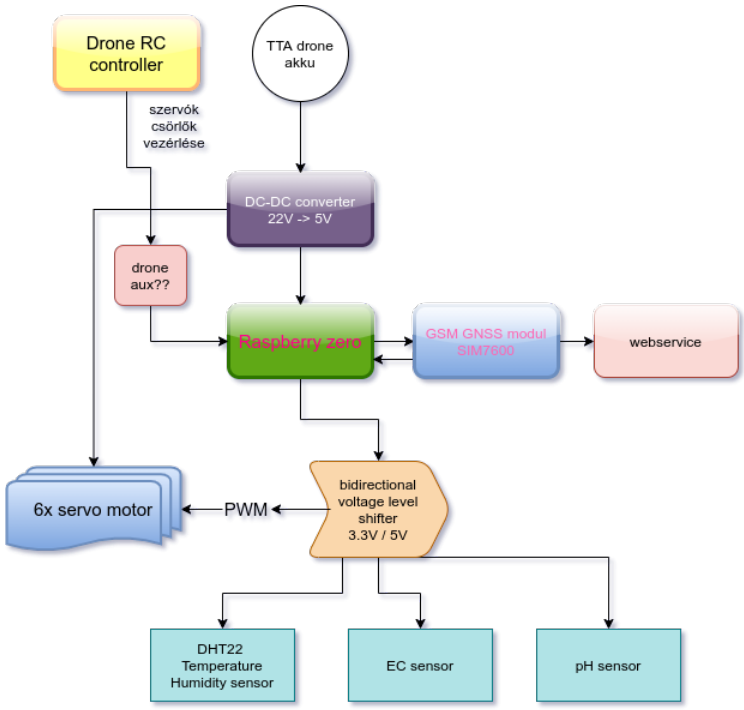

Figure 9. System design of a test drone

In our research, we are investigating the potential application of drones to determine various operational and environmental characteristics related to the operation of installations. Among these, particular attention may be given to the characteristics determining the risk factors associated with the operation (e.g.

emissions of pollutants from power plants). To carry out the research tasks, it is necessary to design and equip test drones with special measuring instruments, which perform the given measurement task during the flight operation as a secondary function.

A possible concept of a drone-mounted measurement data acquisition system is shown in **Figure 9**. The system design shows the microcontroller and microprocessor units that can be connected to the drone with possible sensors, as well as the modules for wireless communication to transmit the measurement data. The unit will be powered by the drone's own battery.

The main professional tasks of the planned R&D project:

1.) Acquisition of tools, software development

Defining the development program of the developed sensor group, selecting basic units suitable for further development, designing the measured data and their transmission system: data depth, quantity, time transfer determination, development of data receiving software, management of software development, and feedback of the results of monitoring drone sensors tests into the development process. It is a basic requirement that the measuring devices installed on the drone should be able to operate in a hazardous operating environment, have the necessary capabilities and have safety certifications confirming them.

2.) Documentation

The development, continuous management and maintenance of the documentation system of the research, if necessary, the rethinking and transformation of the documentation system, and the establishment of the basis for possible future metrology and standardization documentation requirements.

3.) Drone Testing

Testing of drone sensors in airplane mode, air navigation safety, (in some cases, development of airspace licensing procedures) date gathering of different parameters of a plant operation (e.g. waste incineration hazardous energy plant).

4.) Documenting the results achieved, creating a strategy for the utilization of innovation, preparing national and international publications

The main direction of applied research is the development or development of a non-commercially available sensor group that can be connected to a human-controlled or autonomously controlled drone and are suitable for transmitting data measured with various sensors, connected to an appropriate data transmission system and to collect measured data. Due to the novelty of the topic, it is necessary to develop a utilization strategy for delivering it to potential users in the areas set out in the initial objectives, and to support this and present scientific results, to prepare domestic and international scientific publications.

Conclusions

From the above detailed investigations, the following conclusions can be drawn:

- the safe operation of the facilities is determined by a number of operational and environmental parameters, the continuous detection of which, and the processing and evaluation of the information obtained from measurements are expected at operational and even societal level,
- for certain measurement tasks, specially designed drones can provide effective assistance,
- the fitting of a drone with suitable sensors and measuring instruments, and the development of measurement, data collection and data processing technology requires in-depth research,
- a large number of operational measurements are needed to assess the suitability of drones for specific missions.

References

[1] Izabela Gabryelewicz - Maciej Wedrychowicz – Pántya Péter - Patryk Krupa: Raw material and environmental safety of industrial processes. In: Gabryelewicz, Izabela; Wędrychowicz, Maciej (szerk.) Environmental safety - non-energy and raw materials. Zielona Góra, Poland: University of Zielona Góra Press (2021), 166 p. pp. 11-38.

[2] Kátai-Urbán Lajos - Cimer Zsolt - Cséplő Zoltán - Vass Gyula: Examination of the technical competencies required to fulfill the industrial safety responsibilities. In: Bodnár, László; Heizler, György (edit.) Proceedings of the Fire Engineering & Disaster Management Prerecorded International Scientific Conference. Budapest, Hungary: Védelem online (2021) 503 p. pp. 404-413.

[3] Lágymányosi Anikó (2019): Létesítmény üzemeltetésének fejlesztése intelligens technológiákkal Szent István Egyetem, Gödöllő

[4] Lobo Fereira - Bruna Carolina – Restás Ágoston - Bodnár László: Real Examples Focusing the Mental Health Service Provided in the Framework of Crisis Management. Košická Bezpečnostná Revue 8.1. (2018), pp. 11-21.

[5] Rami Mattar (2018): Development of a Wall Sticking Drone for Non-Destructive Ultrasonic and Corrosion Testing Inspectioneering Journal.

[6] Restás Ágoston: Drone Applications Fighting COVID-19 Pandemic—Towards Good Practices. Drones 6. 1. (2022), pp. 1-20. Paper: 15, 20 p.

[7] Rácz Sándor: A tűzoltói beavatkozások súlyponti erőmegosztásának vizsgálata. Hadmérnök, 12. KÖFOP (2017), pp. 92-107.

[8] Z. Bártfai-A Lágymányosi-I. Szabó-T. Tímár (2019): Development of a Digital Database for Supporting Precision Technologies Mechanical Engineering Letters, pp 195-201

[10] https://www.engineering.com/story/automating-facility-inspection-with-drones

[11] https://www.bimcommunity.com/news/load/447/drones-the-perfect-tool-for-facility-inspections
[12] https://inspectioneering.com/journal/2018-04-25/7567/development-of-a-wall-sticking-drone-for-non-destructive-ultraso

The application of plastic plain bearings of different material grades on the shafts of fortschritt k454b baler

Róbert KOVÁCS[1], Péter KORZENSZKY[2], Róbert KERESZTES[3]
[1]Doctoral School of Mechanical Engineering, MATE, Gödöllő
[2]Department of Farm and Food Machinery, Institute of Technology, MATE, Gödöllő
[3]Institute of Technology, MATE, Gödöllő

Abstract

Basically, the baler used in the study was made in the early 1990s, but there are still a large number of them working in Hungarian fields, so the topic is still relevant today.

During the preparations, the plain bearings were machined from PA6, POM C and UHMWPE HD1000 materials, and the pivoting pins were manufactured. The study investigated the correlation of wear intensities as a function of the material qualities of the plain bearings.

In the case of plain bearings, the wear rates have not shown well-measurable and significantly detectable values during operation to date.

For steel bearings, however, more significant wear was already measurable. This is the case for the steel and commercially available sliding pins. The worn surface is eccentric to the original surface, as the mandrels are only loaded in one direction.

In contrast, the steel pin with a UHMW PE HD1000 polymer sliding pin showed the least wear. The wear pattern is naturally eccentric due to the same load. The wear rate of the plain bearing itself also showed no significant results.

Based on the experience and measurements so far, the service life of the bearings can be significantly increased and even more than doubled. In this way, we can reduce the time required for maintenance and repair and increase the machine's uptime.

In the future, the currently measured plain bearings and pins will be re-installed in the machine and subjected to further operational tests.

Keywords

polymer; baler; polymer bearing; PA6; POM C; PE HD1000

1. Introduction

Plastics' role in daily life has increased tremendously, and they are of great importance in the industry, including agriculture. Virtually everywhere we look, we see plastics. Many machine components are made of plastic. In agricultural machinery, it is also common to find applications such as load-carrying or

transmission elements, such as plain plastic bearings, gears, and pulleys. In many cases, sliding and guiding elements in contact with crop parts are also made of plastic. In such cases, making high-precision joints in plastic materials may also be necessary, in which case the machining technology is used.

For the tests, I chose a Fortschritt K454B baler (Figure 1), a heavy-duty trailed baler with a sliding piston suitable for baling and tying hay and straw. A sorting drum carries out the sorting with spring fingers, and the crop is then conveyed to the baling chute by a transversely moving fork conveyor. (Betriebsanleitung Hochdruckpresse K454B, 1988; Ersatzteil-katalog Hochdruckpresse K454B, 1988)

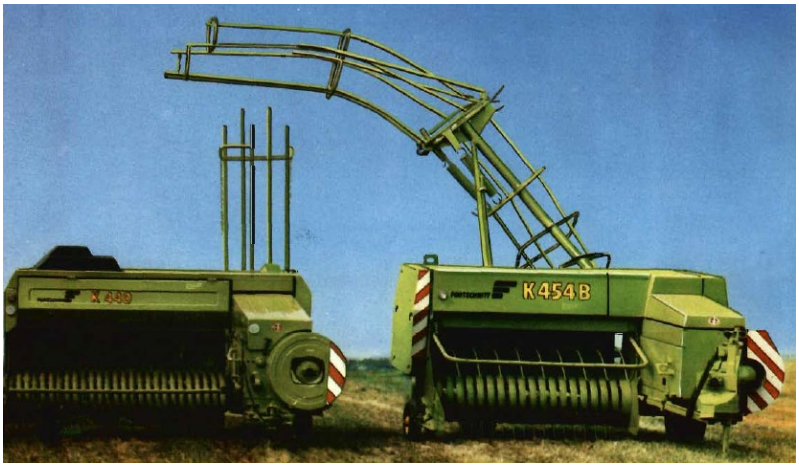

Figure 1 Fortschritt K454B baler (www.mezogeparchivum.hu)

For the test, I chose the shafts of the baler's rewinder, which have steel shaft ends and rotate in a plastic plain bearing during operation. (Figure 2)

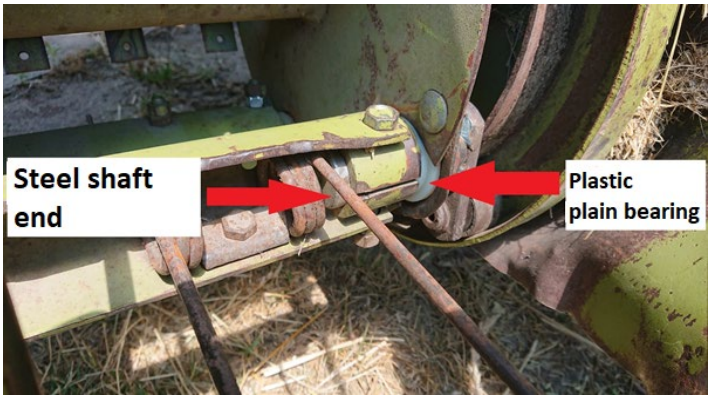

Figure 2 Bale pick-up mechanism with plastic sliding trap

2. Material and methods

Figure 2 shows (Nr.12) a commercially available plain bearing made of injection moulded polyethylene. That Figure shows Nr.03, Nr.07 and Nr.06 are machined plain bearings made from Polyoxymethylene copolymer, Polyamide 6 and Ultra High Molecular Weight Polyethylene (UHMW PE HD 1000), respectively.

Nr.12) Nr.03) Nr.07) Nr.06)

Figure 3 Plain bearings made of different materials before installation;
Nr.12) Commercially available plain bearings made of injection-moulded polyethylene;
Nr.03) plain bearing made of polyoxymethylene plastic (POM C);
Nr.07) Polyamide 6 type plain bearing (PA6);
Nr.06) Ultra High Molecular Weight Polyethylene plain bearing (UHMWPE HD1000);

Ultra high molecular weight polyethylene (PE HD1000)
Applications are generally in plain bearings, sliding guides, cutting tables, food processing, chute and hopper liners for granular handling, insulators, rollers, low-load gears, and shields in the nuclear industry.

Relatively low yield strength 20-24MPa, high toughness, good machinability, weather resistant, damping capability, good chemical resistance, good resistance to abrasion wear. It does not swell when exposed to humidity.

Machining with metal or woodworking tools. It can be used in carbon steel, high-speed steel, carbide, diamond, and sharp finish. Cooling is recommended for high cutting speeds. (www.quattroplast.hu, Fenyvessy et al, 2010, Sarankó et al, 2021)

Polyamide 6 (PA6)
Applications in general: bearing bushings, gears, racks, conveyor belt rollers, sealing elements, sealing rings, cutting plates, sprockets and many other diverse applications in the industry.

Average tensile strength 70-110MPa. Application temperatures can range from -40 to +140°C. Good sliding properties and good wear resistance characterise it. However, it has the disadvantage of being able to absorb water in a humid environment, which changes its mechanical properties and dimensions due to swelling caused by water absorption.

It can be machined by various cutting processes such as drilling, milling, turning, sawing, reaming, etc. It can be used for carbon steel, high-speed steel, carbide, and diamond. Cooling is allowed and recommended at high speeds. (Sarankó et al, 2021)

Polyoxymethylene copolymer (POM C)

Applications include small modular gears, precision dimensional machine parts, springs, valve seats, electrical insulators, water contact parts, rollers, etc.

Relatively high yield strength 70-80MPa, good sliding properties. Application temperatures from -50 to +120ºC, good fatigue and damping properties, high hardness, and good machinability on automatic machines. It does not swell when exposed to water. This grade is copolymer with improved sliding and abrasion properties compared to its homopolymer counterpart and can be used underwater up to 80ºC.

It can be machined in various cutting processes, including carbon steel, high-speed steel, carbide and diamond, with a sharp finish. It is one of the most machinable plastics. For high cutting speeds, cooling is recommended. (www.quattroplast.hu)

The pins (Fig. 3), which rotate in the plain bearings, i.e. the ends of the baler's pick-up shafts, are made of S355 drawn round steel. Their surfaces have not been subjected to any machining process. All four shafts were made of the same grade of material and diameter. S355 is a general-purpose non-alloy structural steel with a low carbon content and a tensile strength generally between 500 and 600 N/mm^2. It is highly suitable for welding. It is readily available commercially. (Kovács 2016)

Figure 4. Rotating pin in plain bearings before use

The field test was carried out in Bács-Kiskun county on sandy soil. This is important for the study because, during operation, the bearings are subjected to

intensive dust loads, part of which comes from the soil, which in our case is sand. During operation, the external temperature was between 25 and 35°C.

All four sliding bearings and pins were installed at the same time so that each one operated under the same conditions and for the same duration. The current operational test lasted for 40 operating hours.

Test preparations

The finished plain bearings were measured in the measuring room of MAG Hungary Kft. in Kecskemét, Hungary, using a calibrated CNC coordinate measuring machine with a Gidding&Lewis Cordax RS150 DCC type Renishaw probe (Figure 4).

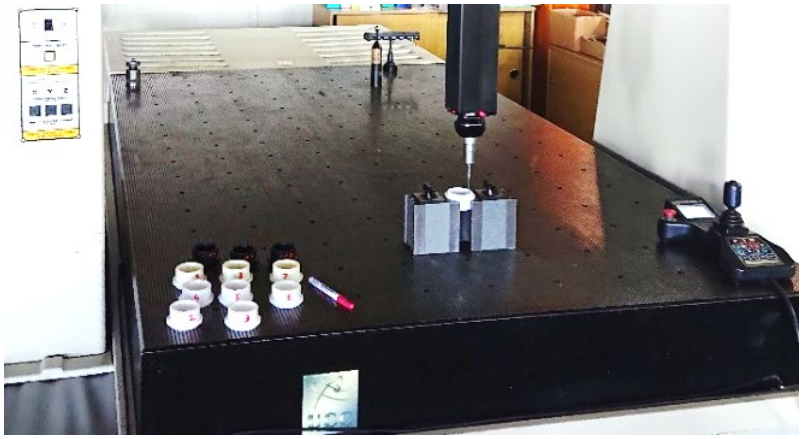

Figure 5. The Gidding&Lewis Cordax RS150 DCC calibrated CNC coordinate measuring machine with Renishaw probe

The nominal inner diameter of the plain bearings is d=40mm. The measurement was made on the inner, i.e. the functional diameter, in two planes of different heights (Z=-5mm, Z=-25mm) at 20-20 points.

The steel pins were measured using a calibrated micrometre with a 0.01mm pitch. The circular tolerance of the pins was within 0.05mm.

3. Results and discussion

Measurements of the inner diameter of the plain bearings and the outer diameter of the pins preceded the operational tests. This was repeated after 40 hours of operation under load.

Figure 7 shows the results of the internal diameter measurements of plain bearing "Nr.03" in the initial, original and after 40 hours of operation in the Z-5 plane.

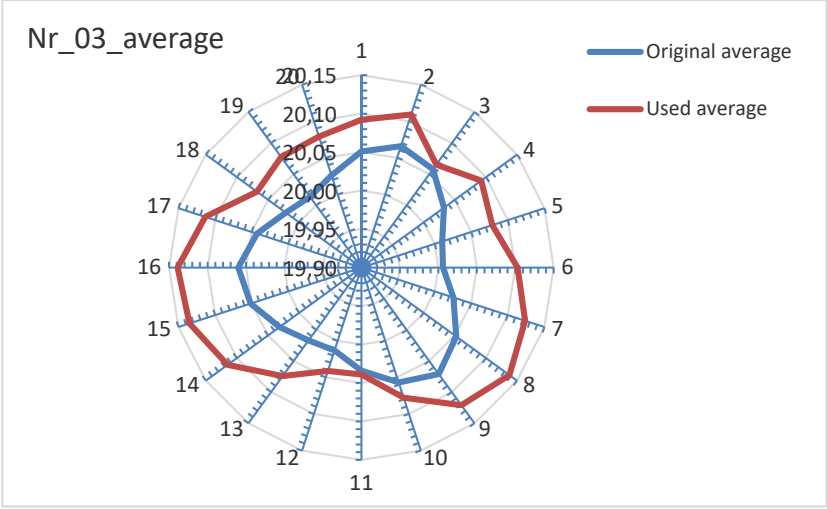

Figure 6. Nr.03 plain bearing inner diameter measurement results before and after use

The measurement results of the "Nr.03" plain bearings show that the Z-5 plane showed wear between 0 and 0.05mm measured in radius.

Figure 6 also shows the measurement results of the inner diameter of plain bearing "Nr.03" in the initial, original and after 40 hours of operation, but now in the Z-25 plane.

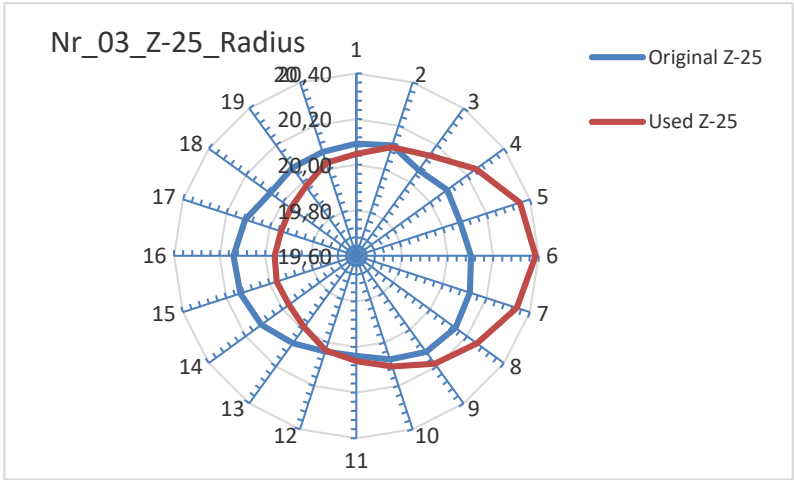

Figure 7. Internal diameter measurement results of plain bearing Nr.03 before and after use in Z-25 plane

The plain bearings in the Z -25 plane showed more interesting results, with all four plain bearings increasing in diameter at some measuring points. This is because the plain bearings are mounted in a steel plate housing with a tight fit.

The plain bearing is thus deformed and, as it was installed for several months, has taken up the shape of the steel housing, and during this time, the stresses have presumably relaxed.

Measurement results of taps

The measurement results for the taps showed more significant wear visible to the eye. The high level of wear can be reported for all four taps, but the results of the tap coupled with the commercially available sliding trap were evaluated first. Figure 7 shows the measurement results of the "Nr.12" pin in the Z-52 plane.

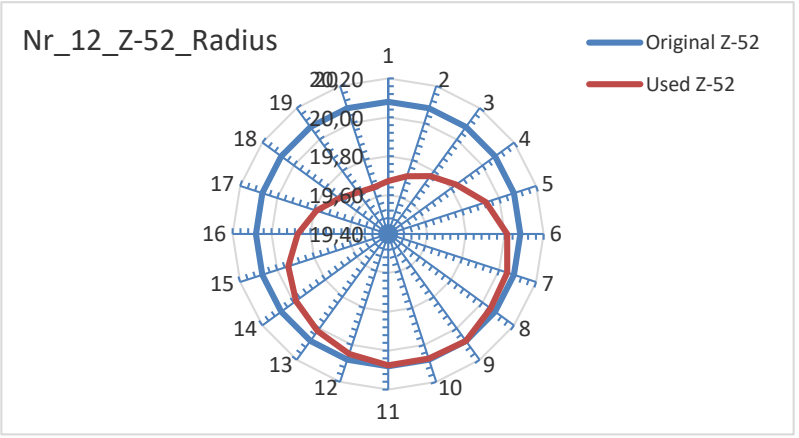

Figure 8. Measurement results of tap Nr.12 in Z-52 plane

Figure 7 shows the wear intensity, with the maximum wear being 0.41mm for the "Nr.12" pin in the Z-52 plane. In this pin's Z-65 and Z-77 planes, the maximum wear rate was 0.4-0.5mm. Figure 8 illustrates the average wear rate per measuring point in the three measuring planes of the "Nr.12" pin.

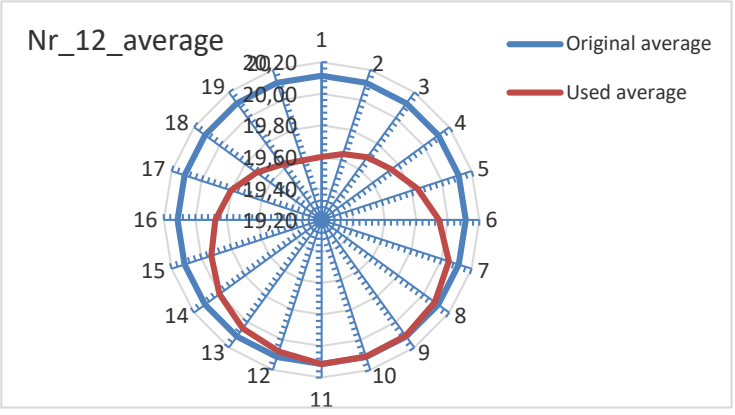

Figure 9. Average wear of pin Nr.12

Figure 8 also shows that the highest average wear is measured at a radius of 0.5mm.

The smallest wear was shown by the "Nr.06" pin, illustrated in Figure 9. The wear pattern here also shows a similar character, i.e. eccentric. However, in this case, the maximum wear rate is 0.165mm, significantly less than the maximum wear rate for a commercially available sliding pin.

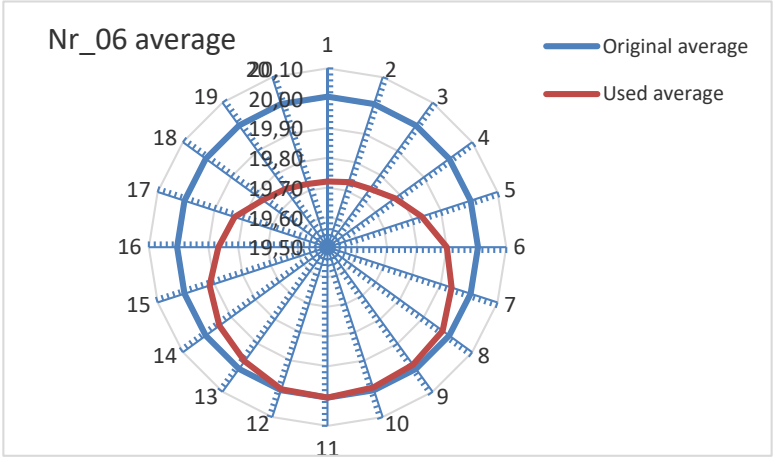

Figure 10. Average wear on pin Nr.06

Figure 10 illustrates the extent of wear on steel pins. It is noticeable that the commercially available plain bearings showed a significantly higher degree of shaft wears than any of the custom-made plain bearings.

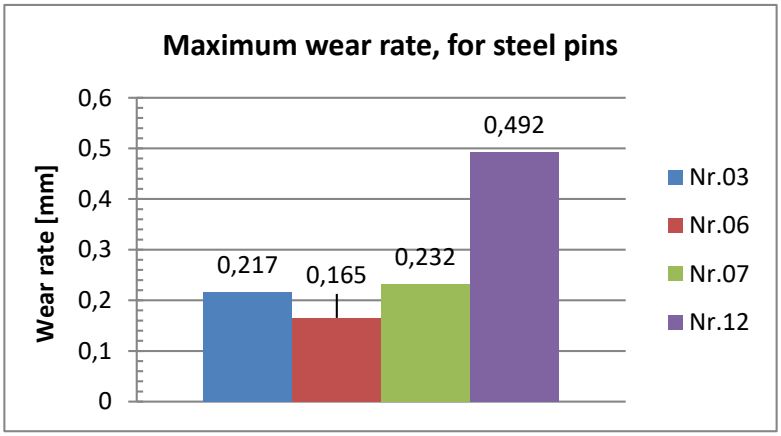

Figure 11. Maximum wear rates for steel pins

Summary

In the case of plain bearings, the wear rate has not shown well-measurable and significantly detectable values during operation so far.

For steel bearings, however, more significant wear was already measurable. This value was highest for the steel pin coupled with the commercially available sliding pin (Nr.12), with a maximum value of 0.49mm in the tested planes. The worn surface is eccentric to the original surface, as the spikes are only loaded in one direction on the shaft.

In contrast, the steel pin coupled with a polymer sliding pin (Nr.06) made of UHMW PE HD1000 showed the least wear. The wear pattern is naturally eccentric due to the same load. However, the maximum wear rate is only 0.165mm, which is only 33% of the wear of a steel pin coupled with a commercially available sliding pin. The wear rate of the plain bearing itself also showed no significant results.

Overall, UHMW PE HD1000 grade plain bearings have shown significantly less wear on the steel pins and no significant wear on the plain bearing. Based on experience and measurements to date, the service life of the bearings can be significantly increased or even more than doubled. This way, the time required for maintenance and repair of the machine can be reduced, and the uptime of the machine can be increased.

In the future, the currently measured plain bearings and pins will be re-installed in the machine and subjected to further operational tests.

References

[1] Betriebsanleitung Hochdruckpresse K454B: VEB Kombinat Fortschritt Landmaschinen, Neustadt in Sachen, (1988), p.43.
[2] Ersatzteil-katalog, Hochdruckpresse K454B: VEB Kombinat Fortschritt Landmaschinen, Neustadt (1988)
[3] Kalácska G., Kozma M., Zsidai L., Keresztes R., (2007): Műszaki Polimerek és Kompozitok a gépészmérnöki gyakorlatban, 3C-Grafika Kft., Gödöllő, p. 315
[4] Kalácska G., (2005): Műszaki műanyag féltermékek forgácsolása, Quattroplast Kft. Gödöllő
[5] Fenyvessy T., Fuchs R., Plósz A., (2010): Műszaki Táblázatok, NSZFI, Budapest
[6] Kovács R. (2016), Műszaki műanyagok forgácsolásának kutatása, Tudományos Diákköri dolgozat, Szent István Egyetem
[7] Kovács R. Korzenszky P., Keresztes R, (2021) Research on the Turning of Technical Polymers, Scientific Bulletin Series C: Fascicle Mechanics, Tribology, Machine Manufacturing Technology, 2021, Vol. 2021 Issue 35, p49-53. 5p.

[8] Sarankó Á., Kalácska G. Keresztes R. (2021) Analysis of Formed Chips in the Case of Turning Different Polymer Materials, HUNGARIAN JOURNAL OF INDUSTRY AND CHEMISTRY Vol. 49 pp. 71–75
[9] www.mezogeparchivum.hu (2022.04.30)
[10] www.quattroplast.hu (2022.04.30)
[11] www.loksacel.hu (2022.04.30)

Heat and power production in high-efficiency heat treatment pyrolysis systems

Viktor MADÁR[1], András BETOVICS[2], Norbert SCHREMPF[2], László TÓTH[2]

[1]Pyrowatt Kft., 6120 Kiskunmajsa, Vágóhíd utca 91. Hungary;
[2]Department of Building Service Engineering and Energetics., Institute of Technology, MATE, Gödöllő

Abstract

In our article, we present a pyrolysis generator installed in a transferable container that produces electricity and thermal energy, which was prepared and set up based on the authors' plans. Their goal was to produce electricity for their own use or for sale in smaller settlements, where biomass with high cellulose content is available in large quantities, though thermal energy generated by the system serves local needs. The specificity of the system is that it is highly efficient, since waste heat energy generated from the operation is recuperated and used to operate the system, and the excess is transferred to public utility purposes. It was established that the CHP system is economical with the current and expectedly high energy prices, and the investment returns in a short period of time.

Keywords

pyrolysis generator, pyrolysis CHP system, system control, heat and electricity from biomass

1. Introduction

Nowadays, we hear a lot about the energy system of the European Union and the individual countries of the union, and about energy dependence. The dependency percentage of our country did not decrease during the years 2000-2018 (Figure 1), moreover a smaller increase was observed. In the EU, in average of all countries, the growth was even higher than ours. Energy improvements are necessary for independent, safer supply. "Hungary's energy production must be strengthened," emphasized Dr. László Palkovics, Minister of Technology and Industry. He noted1: energy sovereignty must be strengthened, energy supply must be diversified, the level of domestic resources and the proportion of renewable energy sources must be increased. The problem is that until now, due attention has not been paid to the development of the electricity network according to the new needs, and the country does not have considerable storage capacity either.

2. Experimental

Data characterizing the energy situation
Figure 1 illustrates the country's energy dependence in % over a period of almost 20 years.

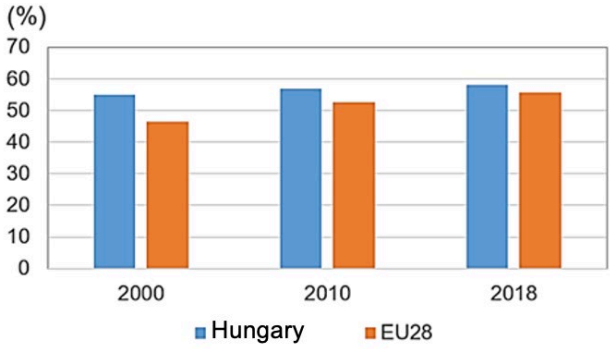

Figure 1. Hungary's dependence on energy imports, compared to the EU average
Source: https://www.ksh.hu/sdg/3-35-sdg-7.html

Examining the domestic final energy consumption, it can be concluded that the largest consumer is the population and agriculture is far below (Table 1).

Table 1. Final energy consumption in Hungary in the year 2020

Sector	PJ	%
Agriculture	29,5	4,0
Industry	185,6	25,2
Transport	185,9	25,3
Trade, services	83,5	11,4
Defence	1,6	0,2
Residental	249	**33,9**
Total	**735,1**	**100**

*Source: https://www.ksh.hu/stadat_files/ene/hu/ene0006.html

Examining the years 2015 and 2020, it can be concluded that residential consumption has not changed significantly, but also according tot he goals. The energy used for heating from natural gas is the highest (more than 50%). Out of the total 250 PJ of thermal energy for thermal energy use, 175 PJ was used for heating. In this area we can acheive considerable savings by insulating the buildings, but the other source, which is firewood, cannot be neglected altough

using it is inefficient and pollutes the environment. In our article we will further address the high cellulite biomass, so we deal with a more efficient and environment-friendly solution for using wood, namely the development of a pyrolysis generator capable of producing low power heat and electricity (CHP).
CHP fuels built on wood can only be found in major municipalities where transport (due to large distances) is costly, the storage of materials is also a problem, but their efficiency is not satisfactory.

Objective of the development
With the pyrolysis energy production equipment developed we wanted to make smaller settlements suitable to use efficient and environmental-friendly electricity and heat systems from locally grown biomass. Pyrolysis is not recent tehcnology, but the efficiency of the method is rising significantly and therefore the equipments can be operated without supervision or with remote monitoring by using modern automation devices. It is a further advantage that I can refer to the so-called circular economy. The gas generated while the process will be used immediately, but the residual high level of mineral ash and residual good biosphere in agricultural areas of municipalities can be used to benefit from soil management.

Resaarch has developed ~50kW electricity and ~100kWkW thermal energy. This can be perfect solution for modifying the electrical energy consumption of smaller settlements, supplying the heat demands of central buildings, educational institutions, kindergartens, social homes and houses in the surroundings of the settlement. Generally there is a considerable amount of hard-stemmed biomass available in the surroundings of the settlements, and the only challenge is collecting and making it suitable for use. This could save considerable amount of natural gas, and improves the surroundings of the settlements while the emissions decrease (gases, dust, soot etc.)

Design of the system
Container-mounted (complete) combined pyrolysis and CHP unit

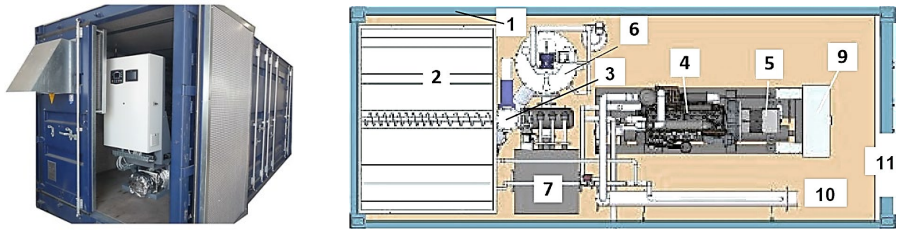

Figure 2. Main constituents placed in the container, view from above
Signs of the Figure:
1-the frame of the container, 2-the top-opening dryer and the feeding auger, 3-material dispenser, 4-gas generator, 5-electrical generator, 6-pyrolysis generator, 7-dust filter, 8-control cabinet, 9-heat exchanger, 10-air inlet.

The equipment developed was mounted in a standard steel container (Figure 2). The biomass enters the equipment in chopped form. As the moisture content of the substance may be greater then necessary, the material entering the storage space is dried by the (recuperated) waste heat energy to an appropriate moisture content before the thermal decomposition process (at 100-150°C), which takes place in the first element of the equipment (Basu, 2010), then passes through the auger feeder towards the pyrolysis generator (Wright et al., 2010).

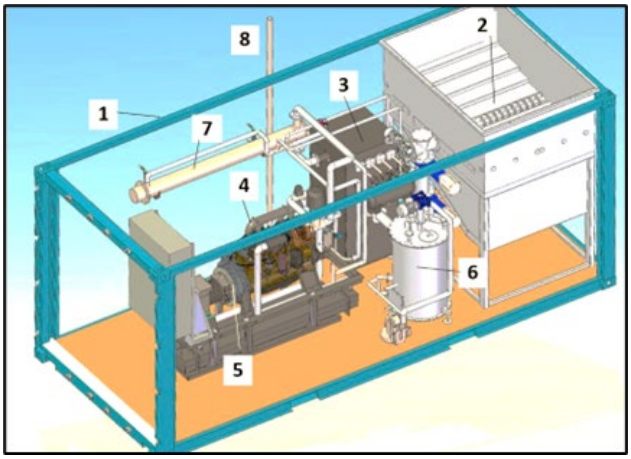

Figure 3. Main constituents placed in the container, x-ray
Signs of the Figure:
1-container housing, 2-drying room and the feeding auger, 3-filter, 4-gas generator, 5-electrical generator, 6-pyrolysis generator, 7-gas cooler, 8-flame.

Description of the operation

The gasification of the material entering the pyrolysis generator takes place gradually, at increasingly higher temperatures. External thermal energy is only required for ignition, the rest of the heat is generated during the reactions of the material (Figure 4).

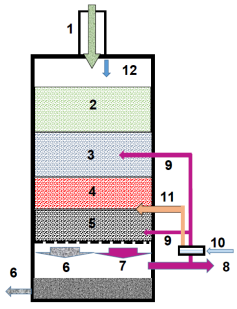

The Signs of the Figure:

1. fuel injection (20–25 °C), 2. Drying zone (60–180 °C), 3. pyrolysis (charring) zone (200–500 °C), 4. combustion zone (800–1000 °C), 5. reduction zone (600–700 °C), 6. ash and its removal, 7. gas, 8. gas discharge to the gas engine, 9. recirculation of part of the gas, 10. air-gas heat exchanger, 11. introduction of warm air, 12. the air coming with the fuel (in gaps)

Figure 4. The principal structure of the gas generator

In the first stage lignin, hemicellulose and cellulose are decomposed of the biomass in the generator. The temperature is around 250-500°C here. The amount of lignin doesn't decrease significantly in hard woods, hemicellulose degrades almost completely (from the initial ~15%), but ~10% of the cellulose (from the initial 30-35%) ain't. Other materials (from the initial ~25%) decompose almost completely into gas (from which oil can be obtained by condensation). In the pyrolysis stage materails split into gas and carbon. Then comes the combustion stage, where the material is already in the form of smoldering reactive carbon, but the gas among particles contains undesirable amount of tar. Reducing the amount of tar, a part of the generated gas is returned here, mixed with air. The materials move forward tot he so-called reduction zone, where the temperature is around 700-800°C. A part of coal degrades into hydrogen and carbon-monoxide, but the combustion product, CO_2 is reduced to carbon-monoxide as well in this smouldering carbon-rich environment. This produces a multi-component combustible gas with considerable energy content, without tar, thus it can be fed into the internal combustion engine after additional filtering (Di Blasi, 2004).

In order to remove the dust content of the producted gas, an aluminium silicate filter is used, which is suitable at high tempraturers (~1100°C) and has great regeneration.

During the process the residue is about 3-6% by weight, namely a mixture of ash and carbon. The stable operation of the gas generator requires a fuel with a moisture content of maximum 18-20%, if this level is higher, the fuel must be dried. Drying the fuel takes place in the drying chamber under the loading inlet of the container with a moving bed system. The supply auger towards the feeder takes place in the lower, central part of the drying chamber (Figure 5).

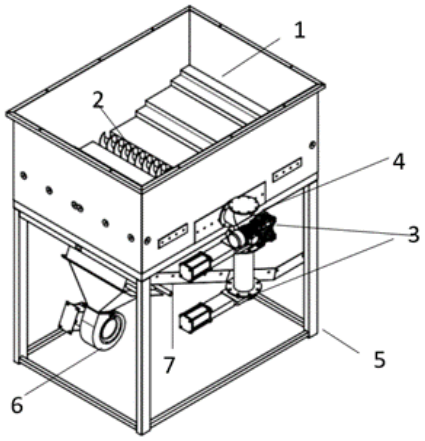

Figure 5. Transport and feeder equipment under the fuel storage
Signs of the Figure:
1-drying chambre, 2-supply auger, 3-dosing sluices, 4-motor and engine of the auger, 5-storage unit frame structure, 6-drying heat gun, 7-tube heat exchanger (air-air).

The drying performance can be controlled by the temperature and flow rate of the drying air. The heat energy of the drying air comes from the cooling of the gas leaving the generator, the high temperature exhaust gas from the engine in addition to the generator and engine heat losses inside the container.

By using heat recovery recuperators – gas cooler and exhaust gas heat exchanger – we can acheive that this equipment is able to operate with ~80% efficiency (have a look at Figure 8). The produced electrical energy will be supplied to the electricity grid. Waste heat may be used for own purposes, or it can be sold under appropriate environmental conditions (domestic hot water or heating). If the starting material is too wet, most of the waste heat must be used for drying. If absolutely dry wood arrives, then the amount of heat corresponding to ~100kW output generated from waste heat can be purchased by external users. The arrengement of the system's thermal engineering is illustrated in Figure 6.

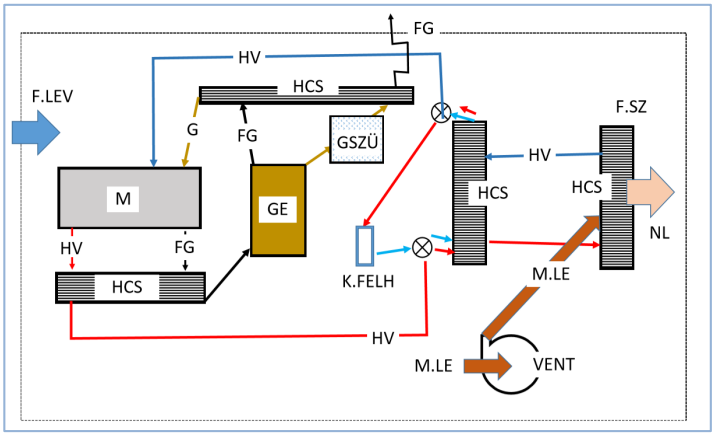

Figure 6. The theoretic flowchart of the system and the relations with heat energy recuperation [9]
Signs of the Figure:
F.LEV-fresh air into the container, M-engine, HV-cooling water, HCS-heat exchanger, FG-flue gas, GE-gas generator, G-gas, K.FELH-external users, M.LE-hot air of the container, VENT-ventillator, F.SZ-Drying wood, NL-moist air (heat loss ~14-16%).

Control of the system

The operation of the gas generator have to be optimized due to acheive the lowest emission values when exhausting (at full load as well).

Satisfactory emission at the exhaust side can only be achieved for engines operating with lean mixtures, with an appropriate excess pressure ratio (air-gas ratio). The control uses (detects and analyzes) the direct correlation between NOx emissions and excess air ratio. The developed so-called Lean-mix control is based on the linear relation between the excess pressure ratio and the temperature, the pressure step and the air-gas temperature. At this control system, all the mentioned quantities can be measures simply and reliably, and the air ratio (X) can be calculated accurately. So the emission requirements are met reliably.

The control unit turns on automatically as soon as the instantaneous output power exceeds the threshold value (this is about 30% of the total operating power). The control unit is always active during the grid connection operation, buti t can also be switched on in isolated mode (depending on the execution). In fact, the PID controller performs the actual control. The electric control valve is the operated unit, which enables the adjustment of the volume of the heating gas at the inlet of the air-gas mixer, and this results in a change in the air ratio.

The operation of the controller is absolutely automated. In case of a deviation, the engine control immediately receives a signal and ensures the synchronous rotation for the generator (Figure 7).

Depending on the gas intake of the gas generator, the gas production of the compartment can be changed. This is controlled by the inlet air at the pressure measuring point at the gas generator's upper point. The desired pressure base is -200Pa. The heat gun shall determine the amount of ambient air required using a hot-wire air volume meter behind the air filter. After all, the entire system is controlled by the Unitronics PLC devices built in.

The communication PLC unit

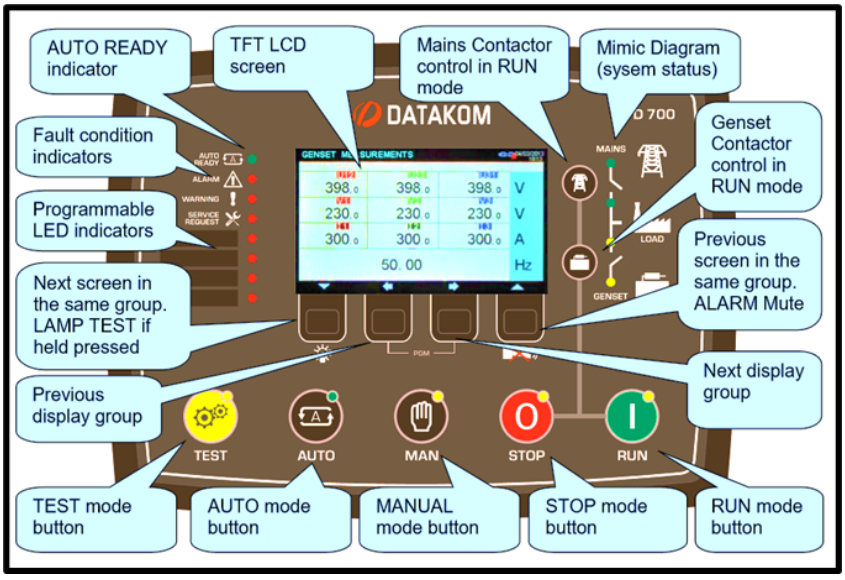

Figure 7. Signs and function points on the control panel

The monitoring data collector records gas consumption, electrical energy production, heat release etc. (current, monthly and annual database can be queried). The efficiencies can be calculated based on these data.

The unit (AMF) between the system and the electrical grid monitors net voltages, ensures the grid and the generator control, runs the engine and provides instrumentation and monitoring of the engine and the generator (Figure 8).
The motorized generator works according to the characteristics of the electrical system, the connection can only be established if the electrical parameters of the system's output energy are absolutely identical.

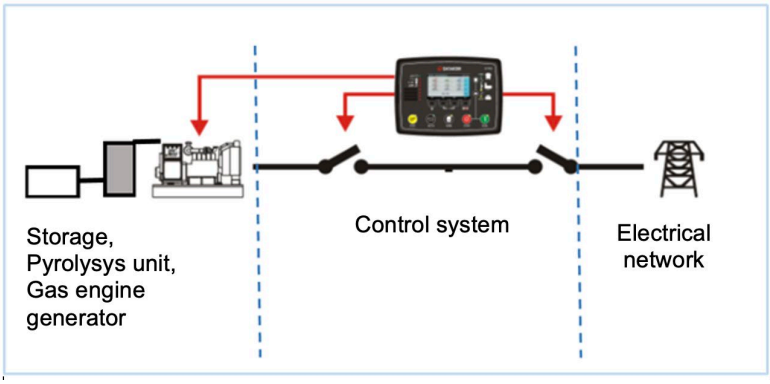

Figure 8. The control between the electrical system and the equipment (MPU with CANBUS inputs)

3. Results

The electricity produced from wood as raw material is supplied tot he electrical grid. Waste heat can be used for own purposes, but it may be sold under appropriate environmental conditions (domestic hot water or heating). If the starting material is too wet, it may need to use the significant part of waste heat. If completely dry wood is received, the heat generated from the waste heat corresponding to ~75kW output can be purchased by external users.

Based on operating test of the presented ~50kWe system, the following performance levels were obtained.

Out of ~41kg wood, with a moisture content of 20%:

- P_e=50-52 kWhe electricity can be obtained, which means that the efficiency is ~27-28% (η_e=0,27-0,28)
- the consumable heat energy is Q_h=75-100 kWh
- 1,0 kWh electricity can be obtained from ~0,8-0,88 kg of wood chops (at a moisture content of 20%)

Conclusions

On domestic market (according tot he current national and international energy situation), the price of commercial wood chips has raised substantially and greatly dependent on the trade. The not precisely defined material quality in the selections makes the purchase speculative. Moisture content, calorific value and often the degree of shredding are missing from the descriptions, nor what was the raw material from which the wood chips were made. Comparing the advertisements found on the Internet: it can be assumed that the price of wet (with a moisture contetnt of 20-28%) mixed wood chips.

- Basicly they have an energy content of 14-15MJ/kg (less, if they are contaminated by soil),
- from which electricity and ~95-100Ft/kWh heat energy is obtained.
- If we consider the equipment's planting and production expenses we find that the system is economical (in case of 7000h/year and 10 years operation, at the price of 6,0-7,0 Ft/kWh).
- It is particularly beneficial, if the biomass is made of waste or own by-product is used.
- At the settlements where the use of heat energy can be provided continuously, the application of the system can be suggested without any risk.

Acknowledgements

The equipment developed is today a product, it was made by the support of the tender titled VÁLLALATI KFI_16. The contract number is: KFI 16-1-2017-0560.

Developer and manufacturer: Cső-Montage Technológiai és Épületgépészeti Kft., http://csomontage.hu

References

[1] Bácskai I.: (2020) Pirolízisgenerátor hatékonyságának növelése Doktori (PhD) értekezés, Gödöllő, Műszaki Tudományi Doktori Iskola, pp. 9-10.

[2] Basu, P. (2010). Pyrolysis and torrefaction. In: Biomass Gasification and Pyrolysis, Practical Design and Theory (pp. 65-96). Elsevier Inc., New York

[3] Dhaundiyal, A., Bercesi, G., Atsu, D., and Toth, L.: (2021) Development of a small-scale reactor for upgraded biofuel pellet, Renewable Energy, 170, pp.1197–1214. DOI: 10.1016/j.renene. 2021.02.057 (IF:7.387)

[4] Di Blasi: (2004) Modelling wood gasification in a countercurrent fixed-bed reactor, AIChE J, 50, pp. 2306-2319.

[5] F. Lettner, P. Haselbacher, H. Timmerer, P. Leitner: 2007 Latest results of "CleanStGas" - Staged biomass gasification CHP, Proceedings of the 15th European Biomass Conference & Exhibition, Berlin
[6] M. Wright, D. Daugaard, J. Satrio, R. Brown: (2010) Techno-economic analysis of biomass fast pyrolysis to transportation fuels, Fuel 89 2e10. https://doi:10.1016/j.fuel.2010.07.029.
[7] Madár V., Tóth L., Schrempf N., Madár Gy., Gubó J., Szegvári P.: (2016) Kísérleti pirolízis kiserőmű tüzeléstechnikai vizsgálata, Mezőgazdasági Technika, ISSN 0026 1890. 58. évf. Nr.02, pp. 2-6.
[8] N. S. Barman, S. Ghosh: (2012) Gasification of biomass in a fixed bed downdraft gasifier – A realistic model including tar, Elsevier, Bioresource Technology 107. sz., pp. 505-511.
[9] Tóth L., Madár V., Bácskai I.: (2019) Pirolízis berendezés fejlesztését megelőző vizsgálatok, Energiagazdálkodás, 60. évf. 1-2. pp. 27-33.
[10] Tóth L.: 2012 Alternatív energiaellátási rendszerek az agrárgazdaságban, Szaktudás Kiadó, Budapest, ISBN 978-615-5224-22-5. 320 p.

Penetration and environmental impact of heat pump systems in europe

Hasna SAADI[1], Péter HERMANUCZ[2]
[1] Doctoral School of Mechanical Engineering, MATE, Gödöllő
[2]Institute of Technology, MATE, Gödöllő

Abstract

The research presented aims to evaluate the ability of a heat pump to be an appropriate alternative in heating and cooling in residential buildings during the gas crisis by comparing primary energy usage over the previous ten years and the volume of use on the European market, CO_2 emission and net present cost. This is accomplished by using in-depth data from statistics provided by the European Heat Pump Association (EHPA). It used standard questionnaires from national heat pump associations, statistical offices and research institutes, and research organizations to calculate the quantity of heat pumps sold. In order to mention the net present cost, the researches made on Cost optimal analysis of heat pump technology adoption in residential reference buildings has been touched upon as well. The results of this analysis emphasizes that there is a large market ahead for industrial heat pump manufacturers. The result motivates the hypothesis of heat pumps an effective example of a significant technology that could assist Domestic Hot Water (DHW) preparation, cooling, and heating. The research suggests a heat pump as future by concentrating research effort on heat pumps industry, design and control optimization.

Keywords

Heat Pumps, Heat Pump Market, Cost Analysis, CO_2 emission

1. Introduction

Residential and commercial buildings make up over 40% of the total primary energy usage in European countries (BPIE 2011). Heating and cooling services currently account for the majority of the end-use energy demand within buildings, making it necessary to reduce energy consumption and CO_2 emissions. Building envelope efficiency criteria are becoming increasingly stricter, and the need of having efficient technical heating and cooling systems is rising. The most current revision to the Energy Performance of Buildings Directive (EPBD 2010), which updates and broadens the key points of the EPBD from 2002 (EPBD 2002), states that all new construction should be "virtually zero energy buildings" by the end of 2020 (Kolokotsa et al., 2011) and (Sartori et al., 2012). In order to limit global

warming to less than 2°C, over preindustrial temperatures, carbon emissions need be cut to 9.5 Gt by 2050, according to the International Renewable Energy Agency (IRENA).

Refrigerants are essential for the operation of heat pumps and cause both direct and indirect environmental impact. On the one hand, they can contribute significantly to the warming of the atmosphere, and on the other hand, they are responsible for the efficiency of the cycle and therefore have a direct impact on the electricity consumption of the equipment (Hermanucz et al., 2018). Reducing final energy consumption through new processes and process efficiency improvements, reusing waste heat, and switching from fossil to renewable sources of energy are the decarbonization strategies leading the industrial transformation. Expanding the use of renewable energy sources and increasing energy efficiency are both important to accomplish this goal (MRF 2021).

Heat pumps can be an illustration of the essential technology that might deliver heating, cooling, and domestic hot water preparation in an environmentally and energy-efficient manner. These devices work by extracting heat that is renewable and naturally existing in the environment, upgrading it to a useful temperature, and then using that temperature to meet heating or cooling demands. Studies by (Ghabour and Korzenszky, 2022) have shown that a solar collector system can meet 69% of domestic hot water demand in Hungary. In contrast, the heat pump systems investigated in this paper are able to meet the full domestic hot water and heating demand. It has been shown that heat pumps are very suitable for applications where heat input is required at low temperatures (Géczi et al., 2013, Géczi et al., 2014). At the same time, other research (Korzenszky and Géczi, 2012) has investigated the applicability of heat pumps in the food industry and shown that favourable conditions for heat pump installation are available in many areas. The above research results substantiate the expectations that heat pumps are likely to become more widespread in the future.

Compared to traditional heating methods, heat pumps have many benefits. They have a fairly effective energy to heat conversion rate. Heat pumps could be a viable substitute for the boiler, furnace, air conditioner, or central ventilation because they are also inexpensive to operate and don't need specialized maintenance (Calcea, 2020). Additionally, according to data from the IEA (International Energy Agency), heat pumps could reduce CO_2 emissions by 5% in the industrial sector and 50% in the construction sector, saving 1.8 billion tons of CO_2 annually (EHPA 2021).

2. Literature review

This article characterizes the heat pump market in different European countries and the cost analysis made all to make sure of the importance of heat pumps. The first phase of the literature review will display the European heat pump market and the second part will display some reductions that heat pumps could do in terms of money and CO_2 emission. The size of the world market for heat pumps in 2018

was expected to be USD 58.6 billion. The cumulative annual growth rate (CAGR) is anticipated to reach a value of 8.5% during 2019–2025 as a result of considerable government assistance in the form of subsidies and other financial incentives, as well as the rising demand for renewable energy sources. The household market is the greatest user of heat pumps, and reversible heat pumps up to 10 kW are the most popular (GVR 2019). Since 2009, more heat pumps are built in Europe each year, according to information on the European Heat Pump Association (EHPA) website. For instance, approximately 3.7 million heat pumps were made in 19 European nations in 2009, while 68% more were created in 2018. (11.6 million units) (Pezzutto et al., 2017).

The examination of the renewable energy industry, including heat pumps, has recently become a crucial problem globally due to the public's keen interest in ecology in the energy sector (Vallances et al., 2019). gave an overview of several heat pump (HP) systems used in Lithuania as an example of a case study for a cold climate. In the context of Europe, they also provide an overview of the HP market trends in Lithuania. (Moià-Pol. et al., 2018) conducted a comparison of the Russian and European heat pump markets. They also discussed the potential uses of combined heat pump systems for small buildings. Maurizio P. and Trinchieri R. (2019) presented the Italian HP market, taking the last ten years into account. Zimny et al. (2015) discussed the growth of the European heat pump market from 2000 to 2013, with an emphasis on Poland. An evaluation of the heat pump support schemes for a few nations was also presented. offered a 10-year analysis of the Italian HP market. Marina et al. (2021) offered an estimate of number of units, and size of the European industrial heat pump market. (Wood, 2019)

European heat pump market

According to EHPA's analysis (EHPA 2021). of 19 European nations, France (1.9 million units), Italy (1.4 million units), Sweden (1.1 million units), Norway (764 000 units), Germany (746 000 units), and Spain were the nation with the highest number of heat pumps sold between 2009 and 2018. (701 000 units). With 167 000 heat pumps sold, Poland came in at number 12 and Lithuania came in at number 18. (Only 29 000 units sold). The highest heat pump sales were registered in France during the second half of the examined decade, followed by Italy, Spain, Sweden, Norway, and Germany. It is clear that Spain has had tremendous sales growth in recent years. The heat pump market in this country saw a rise of up to 130 000 units throughout the studied period (2014–2018). Next came Denmark (41 000 units), Germany (4000 units), Italy (60 000 units), and France (89 000 units) (40 000 units). With a growth of 31 000 units, Poland rose to a very impressive sixth place, while Lithuania was positioned thirteenth. Figure 1 (Witkowska et al., 2021) displays a summary of market growth for heat pumps in several nations.

The quantity of heat pumps sold per 1,000 homes is another crucial sign of how the European heat pump market is developing. In this instance, from 2009 to 2018,

Norway was undoubtedly the top (347 units), followed by Estonia (251 units) Finland (248 units), Sweden (229 units), and Denmark (129 units). Poland came up at a pitiful 18th place, while Lithuania was ranked 12th. In Figure 2, these outcomes are contrasted.

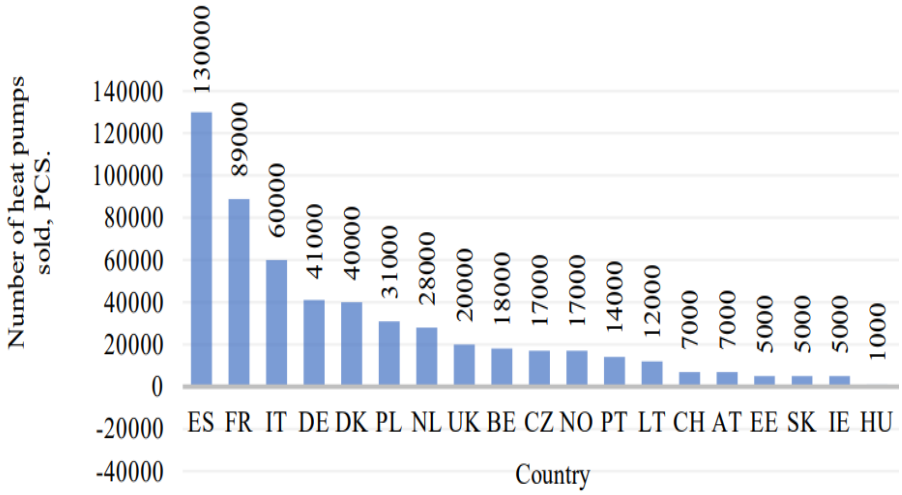

Figure 1. Heat pump market growth in 2014–2018 (Witkowska et al. 2021)

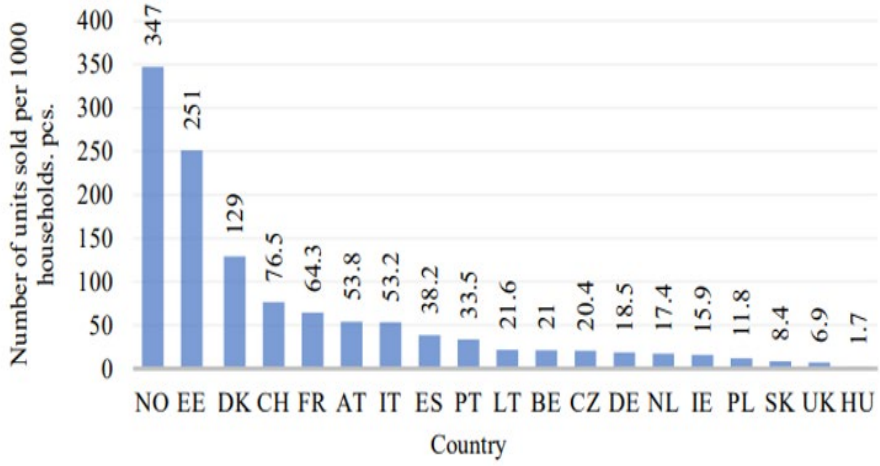

Figure 2. The number of heat pumps sold per 1000 households (Witkowska et al., 2021)

Figure 3 depicts the growth projection for the heat pump market until 2025, taking the gross domestic product of the 19 European nations into account.

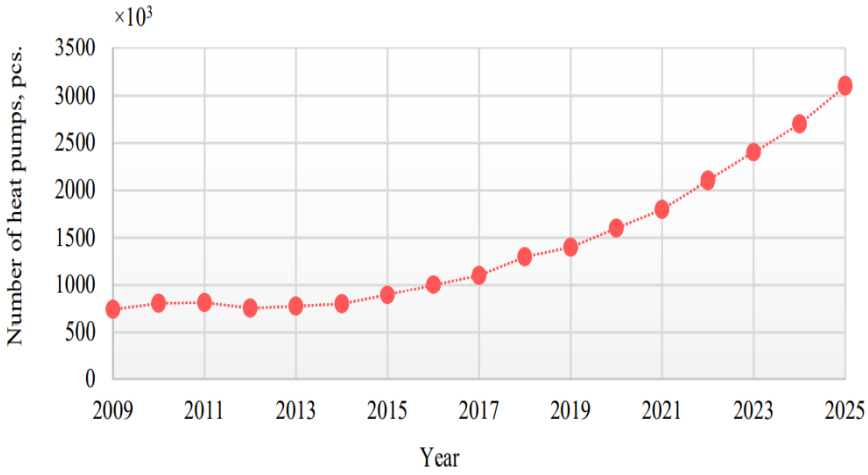

Figure 3. Forecast of the heat pump market development until 2025. (Witkowska et al., 2021)

3. Research metodology

Our research is based on the review of some several publications related to heat pump market, CO_2 emission. In addition, the majority of the statistics used in the analysis were given by the European heat pump association (EHPA 2021), and the authority for electricity and gas (AAEG) especially on results obtained from the study case of (Niccolò A. and Adhikari S 2013). In order to clarify the influence of the production of electricity on the CO_2 intensity, and how does heat pumps also contribute in increasing this intensity because of their consumption of electricity, although they are better than fuel means of heating, I used data records of CO_2 to produce electricity in four European countries (Italy, Austria, Hungary, Poland) during five years (2018-2022) from electricity maps.

4. Results

The following costs are taken into account in the analysis:

1. investment for technical systems (production, distribution, emission, and control)
2. cost of energy (electricity and natural gas tariffs (AAEG))
3. ongoing cost for technical systems' operation and maintenance (Niccolò A and Adhikari S 2013).

The chosen location is Milan, Italy. (Niccoló A. and Adhikari S 2013) presented a simulation and data analytic of Milan as a chosen location to evaluate the reduction in energy demand as well as the reduction of CO_2 emission.

Table 1. Primary energy demand for heating and cooling according to different system configurations and technologies (Niccolò A. and Adhikari S. 2013)

Configuration	Milan Heating [kWh/m^2]	Milan Cooling [kWh/m^2]
Type 1	62.4	22.0
Type 2	53.4	19.2
Type 3	42.6	22.6
Type 4	23.8	10.5
Type 5	22.3	9.6

Type 1. natural gas boiler and split system (baseline)
Type 2. air-to-air heat pump (AAHP)
Type 3. air-to-water heat pump (AWHP)
Type 4. ground-source water-to-water heat pump (GSHP)
Type 5. groundwater-source water-to-water heat pump (GWHP)

Table 2. CO_2 emissions and reduction with respect to baseline type 1 (Niccolò A. and Adhikari S 2013)

Configuration	Milan Emission [$kgCO_2/m^2$]	Reduction [%]
Type 1	19.2	0.0
Type 2	16.2	15.9
Type 3	14.5	24.5
Type 4	7.6	60.3
Type 5	7.1	63.1

Table 3. CO_2 intensity in Italy, Austria, Hungary, Poland to produce the electricity during 5 years 2018-2022 and reduction with respect to baseline Italy (Electricity maps)

Country	CO_2 Intensity [g/kWh]	Reduction [%]
Italy	378 g/kWh	0.0
Austria	249 g/kWh	34.13
Hungary	300 g/kWh	20.64
Poland	820 g/kWh	-116.93

Table 3 shows the intensity of CO_2 over 5 years data registration by the electricity maps of four European countries, considering the Intensity in Italy is the reference, the reduction calculation for each country was performed based on it, therefore we can clearly see that the CO_2 intensity in Austria is the lowest (249g /kWh), and it exceeded twice the reference in case of Poland (820g/kWh). (http1, 2023)

Table 4. CO_2 intensity $kg_{/m^2}$ in Italy, Austria, Hungary, Poland for each given solution types (Electricity maps) (Niccolò A. and Adhikari S, 2013)

Type	**Milan Emission [$kgCO_2/m^2$]**	**Countries**	**Emission [$kgCO_2/m^2$] for each country**
Type 1	19.2	Austria	12.6
		Hungary	15.1
		Poland	41.4
Type 2	16.2	Austria	10.6
		Hungary	12.7
		Poland	34.9
Type 3	14.5	Austria	9.5
		Hungary	11.4
		Poland	31.3
Type 4	7.6	Austria	5.0
		Hungary	6.0
		Poland	16.4
Type 5	7.4	Austria	4.8
		Hungary	5.8
		Poland	15.9

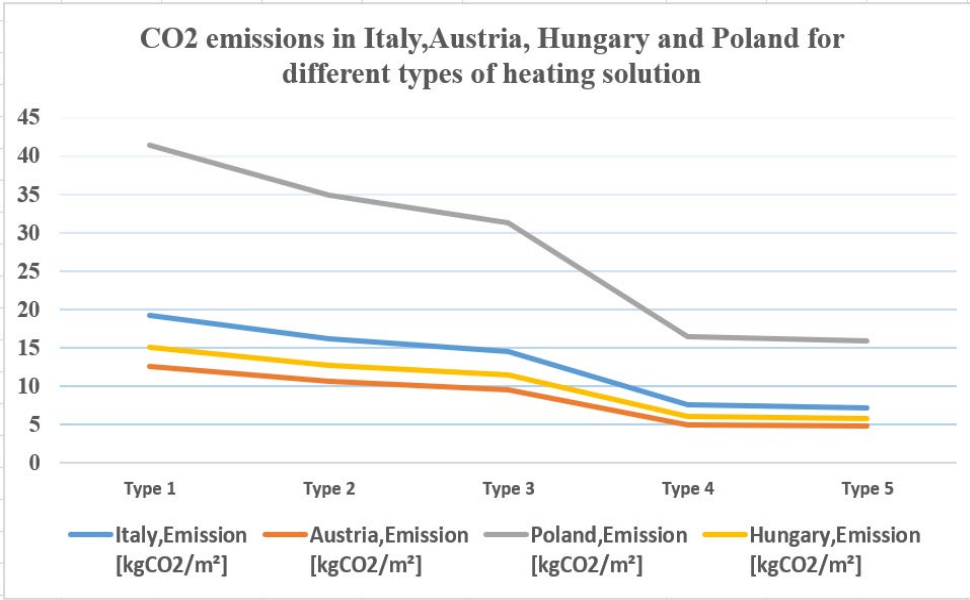

Figure 4. CO_2 emissions in Italy, Austria, Hungary and Poland for different types of heating (own work)

The values of CO_2 emissions in Table 4 have been calculated by multiplying the emissions [kg CO_2 /m^2] values obtained in Milan by the percentage of reduction in each of the three countries with taking in confederation the five different type of heating. The Table 4 also shows that the utilization of heat pumps can minimize the CO_2 emission up to more than 38% compared to natural gas boiler and split system, with the groundwater-source water-to-water heat pump we can reach 4.88 $kgCO_2/m^2$ in Austria as a lowest value and more than 15 $kgCO_2/m^2$ as a good result but not the best because the emission of CO_2 still exist, though because the heat pumps itself consume a significant amount of electricity depends on each country, the following graph Figure 4 clarify that for the same investment, the environmental benefits of heat pumps vary significantly from country to country.

From the graph above we can see that whatever is the type of heating is used the CO_2 emissions in Poland are still higher, but in the opposite side if we consider emission in Austria with the groundwater-source water-to-water heat pump system we can say that the CO_2 savings are also higher.

5. Discussion

In this article, the European heat pump market and estimates of energy consumption, energy savings, and carbon emission reduction are reviewed we obtained that the energy savings attainable with the heat pump system in terms of primary energy consumption is 62.2% for the site location Milan. That is a significant financial benefit, in our opinion. In addition, there are also some environmental benefits according to EHPA (EHPA 2021) estimates, heat pumps installed in the 19 European nations under analysis produced a total of 1000 TWh of renewable energy from 2011 to 2020.France produced the most energy (301 TWh), followed by Sweden (145 TWh), Germany (118 TWh), and Italy (117 TWh). It was only generated in Lithuania in 2.1 TWh, placing the country in 20th place. Additionally, from 2011 to 2020, carbon dioxide (CO_2) emissions in the aforementioned 19 nations were decreased by 266 Mt thanks to the utilization of heat pumps. Between 2011 and 2020, the usage of heat pumps in the nations under study resulted in additional final energy savings of 1000 TWh and useable energy production of 2000 TWh.

Conclusion

According to a review of the European heat pump market, sales of heat pumps have been rising in France, Lithuania, and Poland since 2010 and will start increasing in Spain after two years. But since 2017, the popularity of these heat pumps has increased. Heat pumps were by far the most common option. It has been determined that the CO_2 emissions and net present costs are a significant factor in determining how well large-scale policies for the heating and cooling of buildings may be implemented. The primary objective of the research was to

determine whether heat pumps may replace regular household heating system in the future. The findings of the study unequivocally demonstrate that heat pumps are economically viable, and an environmentally sound choice and it's enough popular to take a chance of an industrial development revolution.
Future demand for heat pumps in the commercial sector is anticipated to be driven by increased consumption, residential construction industry growth, and revenue growth in the service and trading sectors. (Pezzutto et al., 2017). The following are the primary variables affecting the market for heat pumps in Europe: Increasingly wider range of temperatures within which heat pumps can operate with high efficiency, financial incentives for renewable energy, stringent building codes and regulations for heat demand, as well as the use of self-produced electricity, all contribute to low heat pump installation operating costs. (SHPM. 2019)

Refernces

[1] Buildings Performance Institute Europe (BPIE, 2011), Europe's buildings under the microscope. Belgium, ISBN: 9789491143014, 132p.
[2] Autorità per l'energia elettrica ed il gas (AEEG, 2012), Annual Report To The Agency For The Cooperation Of Energy Regulators And To The European Commission On Regulatory Activities And The Fulfillment Of Duties Of The Italian Regulatory Authority For Electricity And Gas, 31 July 2012, 106p.
[3] Calcea N. (2020), Heat pumps are on the rise in Europe. Energy Monitor [Online]. Available: https://www.energymonitor.ai/sectors/heating-cooling/heat-pumps-are-on-the-rise-in-europe/ [Accessed: 09.01.2023]
[4] EHPA (2021): Key Facts on Heat Pumps [Online]. Available: https://www.ehpa.org/technology [Accessed 10.03.2021]
[5] Follow the Directive of 2002/91/EC (16 December 2002) of the European Parliament and of the Council on the energy performance of buildings (EPBD 2002 recast)
[6] Follow the Directive of 2010/31/EU (19 May 2010) of the European Parliament and of the Council of on the energy performance of buildings (EPBD 2010 recast)
[7] Géczi G., Bense L., Korzenszky P. (2014), Water Tempering of Pools Using Air to Water Heat Pump Environmental Friendly Solution. Rocznik Ochrona Srodowiska, 16, 115-128.
[8] Géczi G., Korzenszky P., Bense L. (2013), Ideális körülmények a levegő-víz hőszivattyú uszodatechnikai alkalmazása során. Magyar Épületgépészet, 62:7-8, 7-10.
[9] Ghabour R., Korzenszky P. (2022), Linear Model of DHW System Using Response Surface Method Approach. Tehnicki Vjesnik-Technical Gazette, 29:1, 66-72.

[10] Hermanucz P., Géczi G., Barótfi I. (2018), Environmental and Healthcare Risks of Refrigerants, Mechanical Engineering Letters, 17, 28-34.
[11] Industry Report, (2019) Residential Heat Pump Market Size, Share & Trends Analysis Report By Technology (Air to Air, Water Source), By Power Source (Electric Powered, Gas Powered), By Region, And Segment Forecasts, 2019 – 2025 San Francisco, (GVR 2019), 80p.
[12] Kolokotsa D., Rovas D. Kosmatopoulos E. Kalaitzakis K (2011), A roadmap towards intelligent net zero- and positive-energy buildings, Solar Energy, 85, 3067-84.
[13] Korzenszky P., Géczi G. (2012), Heat Pump Application In Food Technology. Journal of Microbiology Biotechnology and Food Sciences, 2:2, 493-500.
[14] Marina A., (2021), An estimation of the European industrial heat pump market potential. Renewable and Sustainable Energy Reviews, 139, 1105-45. DOI: https://doi.org/10.1016/j.rser.2020.110545
[15] Market Research Future (MRF 2021), Heat Pump Market Research Report, Maharashtra, 111p. https://www.marketresearchfuture.com/reports/heat-pump-market-7012 [Accessed 09.01.2023]
[16] Maurizio P., Trinchieri R. (2019), The heat-pump market in Italy: an in-depth economic study about the reasons for a still unexpressed potential. Clean Energy, 3, 126–143. DOI: https://doi.org/10.1093/ce/zkz002
[17] Moià-Pol A., Morzhukhin A., Nazmitdinov R. (2018), Analysis of heat pump market in Russia. Prospects of application of combined system for small buildings. Presented at 13th IIR Gustav Lorentzen Conference, Valencia, Spain, 2018. DOI: http://doi.org/10.18462/iir.gl.2018.1368
[18] Niccolò Aste, R., Adhikari, S. (2013), Cost optimal analysis of heat pump technology adoption in residential reference buildings. Renewable Energy, 60, 615-624.
[19] Pezzutto S., Grilli G., Zambotti S. (2017), European Heat Pump Market Analysis: Assessment of Barriers and Drivers. International Journal of Contemporary Energy, 3, 62–70.
[20] Sartori I, Napolitano A, Voss K. (2012), Net zero energy buildings: a consistent definition framework. Energy and Buildings, 48, 220-232.
[21] Wood L, (2019), Study of the Heat Pump Market in Europe, Dublin, Research and Markets (11 December 2019) [Online] Available: https://www.prnewswire.com/news-releases/2019-study-of-the-heat-pump-market-in-europe---france-italy--spain-areresponsible-for-more-than-half-of-annual-heat-pump-sales-300973350.html [Accessed 10.03.2021].
[22] Vallancius, R. (2019), A Review of Heat Pump Systems and Applications in Cold Climates: Evidence from Lithuania. Energies, 12(22), 4331. DOI: https://doi.org/10.3390/en12224331
[23] Wikowska, A., Dorota, A., Rodero, A. (2021), Analysis of the Heat Pump Market in Europe with a Special Regard to France, Spain, Poland and Lithuania. Envireonmental and Climate Technologies, 25, 840–852. DOI: https://doi.org/10.2478/rtuect-2021-0063

[24] Zimny J., Michalak P., Szczotka K. (2015), Polish heat pump market between 2000 and 2013: European background, current state and development prospects. Renewable and Sustainable Energy Reviews, 48, 791–812. DOI: Https://Doi.Org/10.1016/J.Rser.2015.04.005
[25] http1, Electricity maps (2023) [Online]. Available: https://app.electricitymaps.com/zone/PL [Accessed 09.01.2023].